

Università degli studi di Bologna

FACOLTÀ DI SCIENZE MATEMATICHE FISICHE E NATURALI

DOTTORATO DI RICERCA IN FISICA

XIX CICLO

Experimental study of neutrino interactions in the OPERA-like Emulsion Cloud Chambers

Author: Donato Di Ferdinando

Advisors:

Prof. Giorgio Giacomelli

Dott. Gianni Mandrioli

Dott. Maximiliano Sioli

PhD Coordinator:

Prof. Fabio Ortolani

Bologna, Marzo 2007

Contents

Introduction	1
1 Neutrino oscillations	3
1.1 Introduction.	3
1.2 Neutrino oscillations phenomenology	4
1.2.1 Pontecorvo's hypothesis	5
1.3 Formalism of neutrino oscillations	6
1.4 Solar Neutrinos	10
1.5 Reactor experiments	13
1.6 Atmospheric Neutrinos	15
1.7 Long Base Line Experiments	25
1.7.1 Direct Neutrino Mass Search	27
1.7.2 Neutrinoless double- β decay	28
2 The OPERA experiment	29
2.1 The OPERA experiment	29
2.1.1 The CNGS neutrino beam	29
2.1.2 The detector	31
2.1.3 Data-acquisition, brick extraction, microscope scanning	37

CONTENTS

2.2	Physics performances: $\nu_\mu \rightarrow \nu_\tau$ search	38
2.2.1	τ detection	38
2.2.2	Background	39
2.3	First test run with the CNGS neutrino Beam	40
3	OPERA emulsion properties	45
3.1	Introduction	45
3.2	Basic properties of emulsions	46
3.2.1	The latent image	47
3.2.2	Development and fixation	48
3.2.3	distortions and shrinkage factor	51
3.3	OPERA emulsion films	52
3.3.1	Refreshing at Tono mine.	55
3.4	LNGS development facility	58
4	The European Scanning System	63
4.1	Introduction	63
4.2	The design of the European Scanning System (ESS)	64
4.2.1	Mechanical stages	67
4.2.2	Optical system	68
4.3	The on-line acquisition software	71
4.3.1	Image acquisition and processing	71
4.4	The off-line track processing	74
4.4.1	Base-track reconstruction	74
4.4.2	Emulsion film alignment	75
4.4.3	Performances of the EES	76

CONTENTS

5	The experimental test PEANUT	79
5.1	Introduction	79
5.1.1	The NuMI neutrino beam	79
5.1.2	The PEANUT detector	83
5.1.3	PEANUT test data flow	88
6	Search for neutrino interactions	91
6.1	Introduction	91
6.2	Brick scanning	91
6.3	Electronic detector predictions	98
6.4	Brick / SFT Alignment	99
6.5	Vertex Analysis	100
6.5.1	Prediction scanning	101
6.5.2	Scanning around <i>stopping points</i>	103
6.6	Conclusions	108
	Conclusions	109
	Bibliography	111

CONTENTS

Introduction

Since their birth, the neutrinos, have been the most interesting particles of the Standard Model (SM). The first neutrino was experimentally observed 28 years after its introduction in the world of particle physics. In the SM there are three types of neutrinos, one for each charged lepton; the neutrinos are considered massless, left-handed particles

In the last decades, several experiments studied solar and atmospheric neutrinos. Early experiments indicated some problems and later experiments evidenced neutrino oscillations as the source of those problems.

Neutrino oscillations were first introduced by Pontecorvo in 1958, in the form of neutrino-antineutrino oscillations. This basic idea was later extended to oscillations among different neutrino flavours. As a consequence neutrinos must have masses different from zero.

The so called "solar neutrino problem", that is the deficit in the neutrino flux coming from the sun, has found a good explanation assuming neutrino flavor oscillations in matter with a mass square difference parameter of the order of 10^{-5} eV² and a relatively large mixing angle between mass and flavour eigenstates.

In the same manner the atmospheric anomaly is interpreted as due to $\nu_\mu \rightarrow \nu_\tau$ oscillations although a direct observation of the ν_τ appearance is still missing.

The OPERA neutrino detector, at the underground Gran Sasso Laboratory, is an experiment mainly designed to perform the first detection of neutrino oscillations in appearance mode. The apparatus is placed in the high energy, long-baseline CERN to LNGS beam (CNGS) at a distance of 730 km from the neutrino source.

The detector is a hybrid detector made of electronic subdetectors and lead/nuclear emulsion target. The electronic modules are trackers and muon spectrometers that accomplish the task of identifying in real time the position of the neutrino interaction inside the target and measure the muon momentum. The target is composed of Emulsion Cloud Chambers (ECC), whose unit is a (*brick*). Each brick is formed of 57 double sided nuclear emulsion films interleaved with 56 lead plate of 1 mm thickness. When a neutrino event hits the detector, the electronics selects the brick, that is then removed, developed and sent to the scanning laboratories for interaction vertex analysis.

The main purpose of this thesis is the analysis of OPERA-like bricks exposed to a neutrino beam. A test exposure was performed at Fermilab (Chicago). A small OPERA-like detector made of electronics trackers and ECC bricks was realized. The detector was exposed, in the MINOS near hall, to the NuMI neutrino beam. For this thesis we have mainly used the tools developed for OPERA to search neutrino vertices inside the bricks.

This thesis is organized as follows:

The first chapter summarizes the theory of neutrino oscillations and discusses a number of experimental results.

The second chapter describes the OPERA experiment and reports its first test run with the CNGS neutrino beam.

The third chapter describes in more detail the emulsions and their handling.

The fourth chapter describes the European Scanning System, including its design details and their performances.

The fifth chapter discusses the PEANUT test exposure performed at Fermilab.

The sixth chapter presents the results obtained in PEANUT and their implications for OPERA.

Chapter 1

Neutrino oscillations

1.1 Introduction.

In 1931 W. Pauli [1] tried to explain the apparent energy non-conservation in nuclear weak decays by an invisible particle that is emitted together with electrons in nuclear beta decays; in fact it was seen that in certain radioactive decays, energy and momentum did not appear to be conserved. Pauli suggested that this missing energy might be carried off, unseen, by a neutral particle which was very difficult to detect. This particle played an important role in the theory of radioactive decays developed by Fermi who called the new particle *neutrino*.

Fermi theory explains accurately many experimentally observed results. The neutrinos "became visible" only 28 years after the prediction, thanks to a reactor experiment performed by F. Reines and C. Cowan [2].

Goldhaber [3], in 1957, showed that the neutrino is left-handed.

Later (1962) a pionering accelerator neutrino experiment at BNL [4] showed a second neutrino, $\nu_\mu \neq \nu_e$.

In 1975 at the SLAC $e^+ e^-$ collider was discovered the τ lepton [5] and 20 years later at Fermilab the lepton family was completed with the ν_τ [6].

The following years saw a remarkable progress in neutrino experiments, especially those utilizing accelerators. Accelerators at increasing energies and at higher inten-

sities, the advances in neutrino beam technology and in massive detectors were used to provide more precise neutrino informations. The neutrino experiments played a key role in testing the validity of the Standard Model of particle physics (SM), and with a variety of other efforts (especially $e^+ e^-$ annihilations and deep inelastic electron scattering) discovered neutral currents, measurements of the neutrino-lepton scattering, etc.. The LEP experiments at CERN demonstrated that there are 3 and only 3 families of neutrinos.

The main goals in the future will probably be on one side a better understanding of the nature of the neutrino and on the other side the use of the neutrino in astrophysics and cosmology as an alternative window on the universe, complementing the information obtained from studies of the electromagnetic spectrum.

In the first experiment [7] performed to detect electron neutrinos produced by the Sun's burning (using a liquid Chlorine target deep underground) was found that less than half of the expected neutrinos was observed (1968). This was the origin of the long-standing *solar neutrino problem*.

1.2 Neutrino oscillations phenomenology

For a long time, it was believed that neutrinos are massless, spin 1/2 particles, making them different from other Standard Model spin 1/2 relatives, such as the charged leptons (e, μ, τ) and the quarks (u, d, s, c, t, b).

The masslessness of neutrinos was so important since its first formulation in the four fermions weak interaction involving only V-A currents proposed by Fermi. This concept was reinforced in the 1950s and 1960s in the V-A theory of weak interaction for charged current weak processes proposed by Soudarshan, Marshak, Gell-Mann and Feynman.

In this theory a massless fermion field equation is invariant under the γ_5 transformation; as a neutrino is one of such particles and it participates exclusively in weak interactions, the weak interaction must reflect invariance under γ_5 -transformation of all fermionic matter participating in weak interaction.

This theory remained valid for a long time as no evidence for neutrino masses was found for almost 50 years.

In the 90's some observations suggested that neutrinos could have mass: the deficits between predicted neutrino fluxes originated by the Sun and by cosmic ray.

The possibility of nonzero neutrino mass at phenomenological level goes back almost 50 years. In the contest of gauge theories, they were discussed extensively in 70's and 80's long before there was any firm evidence for it. The existence of a nonzero neutrino mass makes neutrinos more like the quarks, and allows for mixing between the different neutrino species leading to the phenomenon of neutrino oscillations, an idea first discussed by Pontecorvo in the 60's.

1.2.1 Pontecorvo's hypothesis

Neutrino oscillations were first considered by Pontecorvo [8] in 1957; he assumed that there exists an analogy between lepton charge and strangeness and that not only the strangeness but also the lepton charge is not conserved by the weak interactions.

Following this hypothesis it was natural to assume (in analogy with the K^0 - \bar{K}^0 system) that the neutrinos, eigenstates of weak flavour, are a superposition of mass eigenstates. In this case the oscillations should take place in the neutrino beams and can be established by the shortage of initial type neutrinos. The usual weak interaction Hamiltonian is:

$$H_W = H_W^c + H_W^0, \quad H_W^c = \frac{G}{\sqrt{2}} j_\alpha \bar{j}_\alpha \quad (1.1)$$

Here

$$j_\alpha = (\nu_{eL} \gamma_\alpha e_L) + (\bar{\nu}_{\mu L} \gamma_\alpha \mu_L) + j_\alpha^h \quad (1.2)$$

is the weak charged current, $\Psi_L = \frac{1}{2}(1 + \gamma_5) \Psi$ is the left-handed component of Ψ , $G = 10^{-5}/M^2$ is the weak interaction constant. The second term of the Hamiltonian is the neutral current contribution. In the case of 2 neutrinos and of

leptonic/charge non conservation one may write the following Hamiltonian:

$$H = m_{\bar{e}e}\bar{\nu}_{eR}^c\nu_{eL} + m_{\bar{\mu}\mu}\bar{\nu}_{\mu R}^c\nu_{\mu L} + m_{\bar{\mu}e}(\bar{\nu}_{\mu R}^c\nu_{eL} + \bar{\nu}_{eR}^c\nu_{\mu L}) + h.c. \quad (1.3)$$

where the parameters m_{xy} have the dimensions of a mass. The Hamiltonian can be written more compactly as:

$$H = \bar{\nu}_R^c M \nu_L + \bar{\nu}_L M^+ \nu_R^c \quad (1.4)$$

where

$$\nu_L = \begin{bmatrix} \nu_{eL} \\ \nu_{\mu L} \end{bmatrix} \quad \nu_R^c = \begin{bmatrix} \nu_{eR}^c \\ \nu_{\mu R}^c \end{bmatrix} \quad M = \begin{bmatrix} m_{\bar{e}e} & m_{\bar{\mu}e} \\ m_{\bar{\mu}e} & m_{\bar{\mu}\mu} \end{bmatrix} \quad (1.5)$$

The M values are real and the M matrix can be diagonalized as:

$$M_0 = \begin{bmatrix} m_1 & 0 \\ 0 & m_2 \end{bmatrix} \quad (1.6)$$

and the Hamiltonian becomes:

$$H = \sum_{i=1,2} m_i \bar{\phi}_i \phi_i \quad \phi = M^T \chi \quad (1.7)$$

Thus in the usual weak interaction appears some orthogonal superimpositions of fields of neutrinos, whose masses m_1 and m_2 are not equal to zero.

1.3 Formalism of neutrino oscillations

For three neutrino flavour the neutrinos have three mass eigenstates $|\nu_i\rangle = \nu_1, \nu_2, \nu_3$ and three weak flavour eigenstates $|\nu_\alpha\rangle = \nu_e, \nu_\mu, \nu_\tau$.

The neutrinos created in weak interaction processes, coupling to the W boson and to a charged lepton, are weak flavour eigenstates, which can be written in terms of mass eigenstates as:

$$|\nu_\alpha\rangle_{Flavour} = \sum_{i=1}^3 U_{\alpha i}^* |\nu_i\rangle_{Mass} \quad (1.8)$$

U is a unitary leptonic mixing matrix, the so called PMNS matrix to honor the pioneering contributions of Pontecorvo, Maki, Nakagawa, Sakata [9]. This matrix can be parametrized as:

$$U = \begin{bmatrix} c_{12}c_{13}e^{i\alpha_1/2} & s_{12}c_{13}e^{i\alpha_2/2} & s_{13}e^{-i\delta} \\ (s_{12}c_{23} - c_{12}s_{23}s_{13}e^{i\delta})e^{i\alpha_1/2} & (c_{12}c_{23} - s_{12}s_{23}s_{13}e^{i\delta})e^{i\alpha_2/2} & s_{23}c_{13} \\ (s_{12}s_{23} - c_{12}c_{23}s_{13}e^{i\delta})e^{i\alpha_1/2} & (-c_{12}s_{23} - s_{12}c_{23}s_{13}e^{i\delta})e^{i\alpha_2/2} & c_{23}c_{13} \end{bmatrix} \quad (1.9)$$

where $c_{ij} = \cos \theta_{ij}$, $s_{ij} = \sin \theta_{ij}$, θ_{12} , θ_{13} and θ_{23} are three mixing angles, δ , α_1 and α_2 are three phases.

The phases α_1 and α_2 , known as Majorana phases, are the extra physically significant phases that U may contain if the neutrinos are Majorana particles. These phases influence neutrinoless double beta decay.

The phase δ appears only if CP is violated in weak interactions.

Let us have a look to neutrino flavour change and we consider how neutrinos with flavour α (eq 1.9) will evolve in time. First, we apply Schrödinger equation to the ν_i component of ν_α in the rest frame of that component; we have:

$$|\nu_i(\bar{t}_i)\rangle = e^{-im_i\bar{t}_i} |\nu_i(0)\rangle \quad (1.10)$$

where m_i is the mass of ν_i , and \bar{t}_i is the proper time in the neutrino rest frame. In terms of the time t and position L in the laboratory frame, the phase factor in Eq. 1.11 may be written

$$e^{-im_i\bar{t}_i} = e^{-i(E_it - p_iL)} \quad (1.11)$$

were E_i and p_i are, respectively, the energy and momentum of ν_i in the laboratory frame. The neutrino will be relativistic and will propagate at almost the velocity of light. So, the phase factor of Eq. 1.12 can be evaluated with $t \simeq L$ ($c=1$) and it becomes $e^{-i(E_it - p_iL)}$.

In the case of two neutrinos ν_α , ν_β and ν_1 , ν_2 , there is only one squared-mass difference $\Delta m = \Delta m_{21}^2 = m_2^2 - m_1^2$ and the mixing matrix can be parameterized in terms of one mixing angle θ :

$$U = \begin{bmatrix} \cos \theta & \sin \theta \\ -\sin \theta & \cos \theta \end{bmatrix} \quad (1.12)$$

The transition probability of a neutrino of flavor α into a neutrino of flavour β becomes

$$P(\nu_\alpha \rightarrow \nu_\beta) = \sin^2 2\theta \sin^2 \left[1.27 \frac{\Delta m^2 (eV^2) L (km)}{E_\nu (GeV)} \right] \quad (1.13)$$

where are introduced the correct c and h factors inside the \sin^2 argument.

Data from solar and atmospheric neutrino experiments have been analyzed in terms of two flavours. In (1.16), L is the distance between the neutrino production and detection points. The oscillation behaviour of (1.17) has a frequency $\Delta m^2 L / E_\nu$ and the oscillation length λ may be written as:

$$\lambda = \frac{E\pi}{1.267\Delta m^2} \quad (1.14)$$

The oscillation probability has maxima for:

$$L = \frac{\lambda + n\pi}{2} \quad (1.15)$$

The first maximum corresponds to $E / L \approx \Delta m^2$.

If $\Delta m^2 \gg E/L$, the term $\sin^2 (1.267\Delta m^2 L/E)$ oscillates very fast, and, owing to the experimental resolution and neutrino energy bandwidth, it is not possible to observe the oscillation probability but only a mean value:

$$P(\nu_e \rightarrow \nu_\mu) \rightarrow \frac{1}{2} \sin^2 2\vartheta \quad (1.16)$$

In the same way, when $\Delta m^2 \ll E/L$ the argument of \sin^2 becomes too small, ($\sin \vartheta \approx \vartheta$) and we obtain for the oscillation probability:

$$P(\nu_e \rightarrow \nu_\mu) \approx \sin^2 2\vartheta \left(1.267 \frac{\Delta m^2 L}{E} \right)^2 \quad (1.17)$$

Also in this case it is not possible to observe oscillations, even if there is a clear sign of the phenomenon.

In the case $\Delta m^2 \sim E/L$ we reach full sensitivity.

The sensitivity of an oscillation detector experiment is determined by the source-detector distance and by the neutrino energy. Table 1.1 shows the sensitivity in Δm^2 for an oscillation experiment depending on the used source.

Source	L (km)	E (GeV)	$m^2(eV^2)$
Sun	10^8	10^{-3}	10^{-11}
Atmosphere (zenith)	10	1	10^{-1}
Atmosphere (nadir)	10^3	1	10^{-4}
Reactors	10^{-2}	5×10^{-3}	0.5
Accelerator (SBL)	1	20	20
Accelerator (LBL)	10^3	20	10^{-2}

Tab. 1.1: Sensitivities for Δm^2 for different kind of neutrino sources.

In an oscillation experiment, if we fix L and E, the expression (1.16) depends only on Δm^2 and $\sin^2 2\vartheta$, so it is possible to obtain a region in $[\Delta m^2; \sin^2 2\vartheta]$ in which it is possible to measure the oscillation probability $P(\nu_e \rightarrow \nu_\mu)$.

If the experiment probes a region of small $\sin^2 \vartheta$, it needs good statistics as the effect is small. Since the neutrino flux, and the event rate, fall off with increasing source-detector distance L as $\Phi_\nu \propto 1/L^2$ the detector must be relatively near to the source to have large event rates. For the condition of maximum sensitivity ($\Delta m^2 \sim E/L$) the experiment will probe large values of Δm^2 .

In disappearance experiments one measures the neutrinos flux at a distance L from the source and one looks for a reduction in the expected flux. The sensitivity of this kind of experiment is limited to the knowledge of the flux at the origin. In these experiments it is not possible to know the mode of oscillation since one observes only one flavour. The solar and atmospheric neutrinos have been studied by disappearance experiments.

In appearance experiments a neutrino beam of a specific flavour is created and

one searches, at a distance L from the source, for reactions induced by neutrinos of different flavours. An example of appearance experiment is the search for ν_τ identified by τ production and decay in emulsion in a predominantly ν_μ beam.

1.4 Solar Neutrinos

The Sun is a "nuclear fusion reactor", and produces electron neutrinos only. These neutrinos are obtained from many processes; the main one, that produces almost 98.5% of the energy of the sun and almost all the neutrinos, is the p - p cycle:



The so called Standard Solar Model (SSM) predicts the fluxes of the solar neutrinos and their energy.

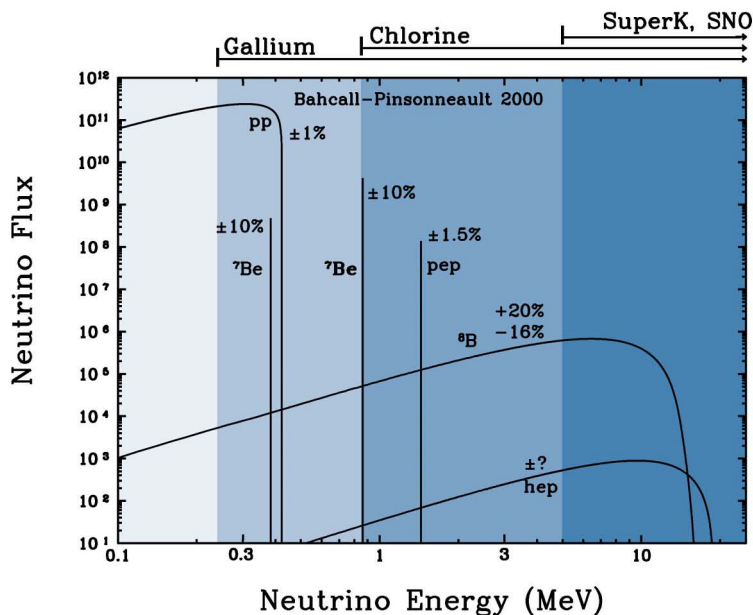


Fig. 1.1: Energy distribution of solar neutrino fluxes predicted by the SSM [10]. At the top of figure are indicated the thresholds for various experiments.

The first experiment that led to take into account seriously the oscillation hypothesis was **Homestake** [11](South Carolina, USA, a mine under 1480 m of rock, corresponding to about 4200 m of water equivalent); Davis and coworkers, used a target composed of 615 ton of C_2Cl_4 in which an inverse β decay reaction: $\nu_e + {}^{37}Cl \rightarrow e^- + {}^{37}Ar$ was detected by radiochemical techniques. The reaction happens only if neutrinos have a minimum energy of 0.813 MeV; so, as can be seen in Fig. 1.1 the main component of the measured flux is due to neutrinos coming from the 7Be and 8B reactions. The result of this experiment was $R(data/theory) = 0.33 \pm 0.06$.

Also Gallium based experiments, **SAGE** (in Baksan) and **Gallex-GNO** [12] (in Gran Sasso), had a lower threshold (0.233 MeV). The results from the Gallex-GNO experiments are showed in figure 1.2. The measured value is 70 Solar Neutrino Unit (SNU) while the prediction is 130 SNU, thus the ratio measured/predicted $\simeq 0.52$

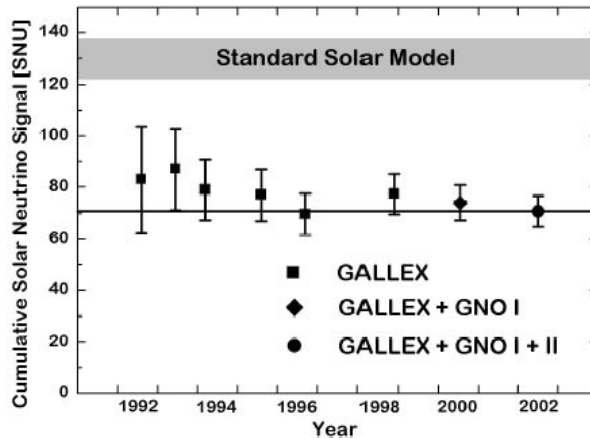


Fig. 1.2: Cumulative results of Gallex and GNO experiments

The radiochemical experiments are not able to measure the direction of the ν_e detected. The **Kamiokande** [13] experiment, built at the depth of 1000 m, was a 3 kton water Cerenkov detector, where the elastic scattering of solar neutrinos on electrons ($\nu_e + e^- \rightarrow \nu_e + e^-$) was observed by 1000 20-inch photo multiplier tubes (PMTs) placed uniformly in the inner surface water-tank walls. It was observed that the ν_e came from the sun and there was a deficit:

$$R(\text{data/theory}) = 0.49 \pm 0.06$$

An upgraded detector with 50 kton mass and more than 10000 PMTs, called SuperKamiokande [14] obtained the result

$$R(\text{data/theory}) = 0.451 \pm 0.005$$

All experiments reported a deficit in the solar neutrino flux relative to the SSM. Neutrino oscillations could be a good explanation of the deficit but it was difficult to be sure.

A strong hint to the solution of the solar neutrino problem came with the Sudbury Neutrino Observatory (**SNO**) experiment [15, 16]. The neutrino target was 1000 ton of 99.92% isotopically pure D_2O , contained inside a 12 m diameter acrylic vessel.

An array of 9456 20 cm PMTs mounted on an 18 m diameter stainless steel geodesic structure, was used to detect Cherenkov radiation. The acrylic vessel and the geodesic sphere are immersed in pure H_2O to provide shielding against radioactivity background.

Low energy neutrinos interact with deuterium via three different reactions:

- Charged current (CC) interaction of electron neutrinos with deuterium: $\nu_e + H^2 \rightarrow p + p + e^-$;
- the neutral current (NC) dissociation of deuterium through the interaction by an active neutrino flavour: $\nu_x + H^2 \rightarrow n + p + \nu_x$;
- and elastic scattering (ES) on electrons: $\nu_x + e^- \rightarrow \nu_x + e^-$;

Sensitivity to these three reactions allow SNO to determine the electron and non electron active components of the solar neutrino flux.

The result of SNO experiment, was that the total neutrino flux ($\nu_e + \nu_\mu + \nu_\tau$ determined from NC interactions) is in good agreement with the SSM and that the ν_e flux is suppressed (as measured from CC). This is a good evidence that the lack

of neutrinos could be due to flavour changing processes that convert ν_e to other flavour as expected from the ν oscillations.

In conclusion combining the solar neutrino data of all the experiments arise a picture in which all the measurements, based on CC and ES, detect a number of events less than one expected from the theory, and that suppression is energy dependent. The Standard Model, in which neutrinos are massless, is not able to explain the data.

Assuming neutrinos with mass it is possible to calculate from the data a mass difference and the mixing angles. At present the best fit of all the data strongly favour the so-called Large Mixing Angle (LMA) solution with two-neutrino mixing parameters $\Delta m_{SUN}^2 \approx 7 \times 10^{-5} eV^2$ and $\tan\Theta_{SUN} \approx 0.4$.

1.5 Reactor experiments

Assuming CPT invariance it is possible to investigate the oscillation solution to the solar neutrino problem also using antineutrinos. The KamLAND [17] detector, in the Kamioka mine, Japan, searched for the disappearance of $\bar{\nu}_e$ in the flux coming from nuclear power plants in Japan. This experiment explored a region of oscillation parameters that is almost the same of the solar neutrino experiments (the average pathlength was ≈ 200 km and the $\bar{\nu}_e$ energies are in the MeV region). The KamLAND result is important because it is a proof independent from the SSM of the sun.

The KamLAND experiment consisted of 1 kton of ultra-pure liquid scintillator contained in a transparent nylon-based balloon suspended in non scintillator oil. The balloon was surrounded by an array of 1879 PMTs monted on the inner surface of an 18 m diameter spherical stainless steel containment vessel.

Electron antineutrinos were detected via the inverse β -decay reaction ($\bar{\nu}_e + p \rightarrow e^+ + n$) with a 1.8 MeV $\bar{\nu}_e$ energy threshold.

In absence of $\bar{\nu}_e$ oscillations the number of expected events above the 2.6 MeV threshold is 365. The number of observed event was 258. The ratio between observed

and expected, without oscillations, is :

$$R = 0.658 \pm 0.044(stat) \pm 0.047(syst)$$

(see also Fig. 1.3).

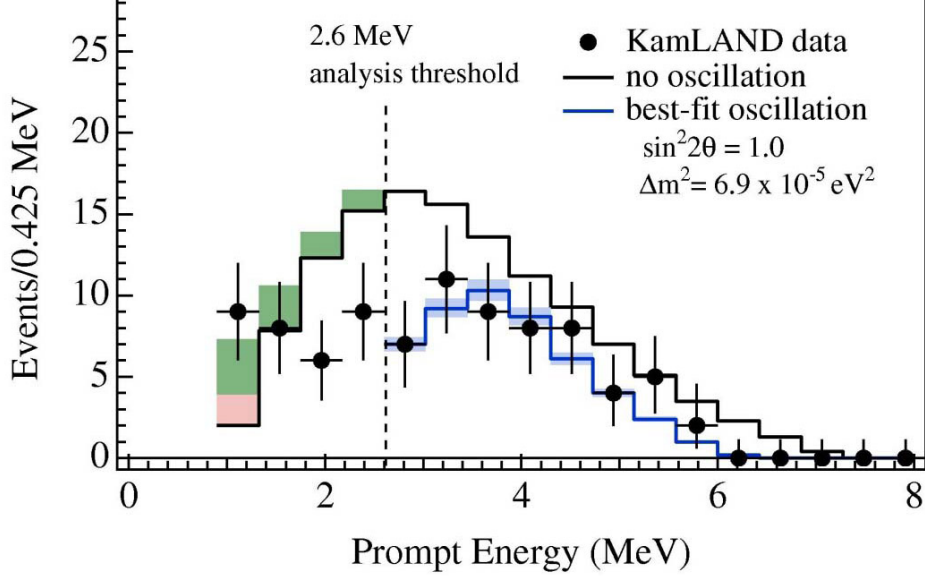


Fig. 1.3: Up: expected energy spectrum of reactor $\bar{\nu}_e$ with geolical neutrinos and background. Down: measured energy spectrum of observed events, compared with the expectations with and without neutrino oscillations

Figure 1.4 shows the combined solution of the oscillation parameters of solar neutrinos and KamLAND: the values for Δm_{12}^2 and θ_{12} obtained combining KamLAND and solar experiments are:

$$\Delta m^2 = 7.9_{-0.5}^{+0.5} \times 10^{-5} eV^2 \quad tg^2\theta = 0.40_{-0.07}^{+0.10} \quad (1.19)$$

Other reactor experiments were made, among these we recall CHOOZ [18] and Palo Verde [19].

Both were reactor $\bar{\nu}_e$ disappearance experiments. CHOOZ consisted of a 5 tons of liquid scintillator in which antineutrinos were detected, 1 km from the source, using the inverse β -decay reaction: $\bar{\nu}_e + p \rightarrow n + e^+$, with a thresholds of 1.8 MeV.

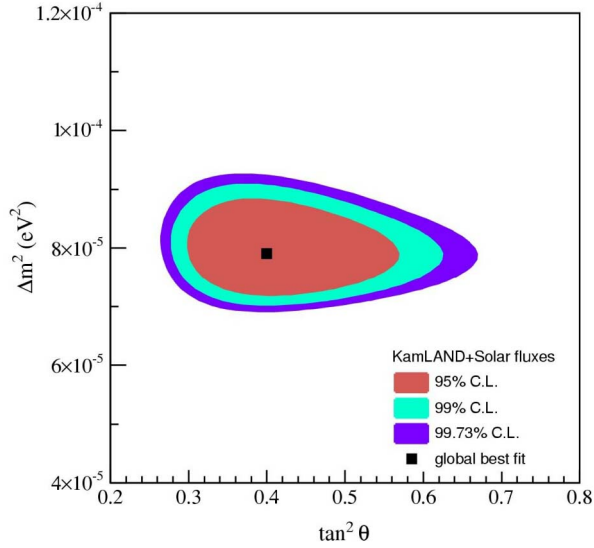


Fig. 1.4: Allowed region of KamLAND + Solar global analysis.

The ratio of observed and expected number of events in the CHOOZ experiment was: $N_{obs}/N_{exp.} = 1.01 \pm 0.04$ showing no indication on any electron antineutrino disappearance and setting an upper limit of:

$$\sin^2 2\theta_{13} < 0.10 \tag{1.20}$$

1.6 Atmospheric Neutrinos

Atmospheric neutrinos arise from the decays of the reaction product (π^\pm , K^\pm and then μ^\pm) of primary cosmic rays (p,N) with the nuclei of the earth atmosphere (N, O).

The primary cosmic ray flux is isotropic and the target (the atmosphere) has a spherical symmetry that assures the total neutrino flux must be up/down symmetric with respect to the horizon.

Atmospheric neutrinos are well suited for the study of neutrino oscillations, as they have energies ranging from a fraction of GeV up to more than 100 GeV and from the point of production to the detector they travel distances L from few tens

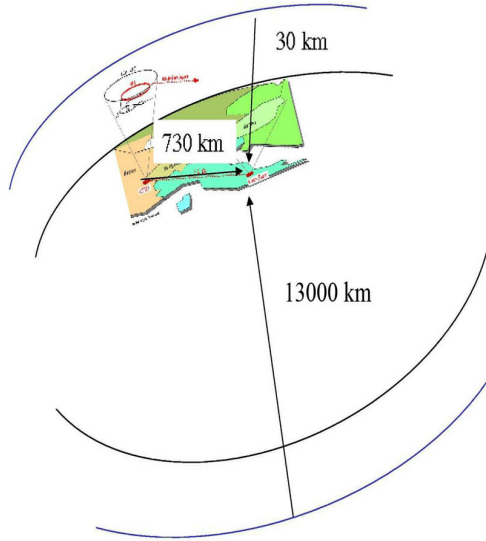


Fig. 1.5: Schematic view of atmospheric neutrino measurements. A neutrino detector (for example located at Gran Sasso lab.) is able to measure neutrinos simultaneously from a large range of distances.

of km (when arriving from above) up to 13000 km (from below) (Fig 1.5): thus L/E_ν ranges from ≈ 1 km/GeV to 10^5 km/GeV. Atmospheric neutrinos are useful to study oscillations for small Δm^2 , and matter effects can be studied with their high energy component.

The early underground experiments on atmospheric neutrinos used detectors designed to study proton decay, that is water Cerenkov detectors and tracking calorimeters. As far as neutrino interactions the results were expressed in terms of the double ratio $R' = R_{obs}/R_{MC}$, where $R_{obs} = (N_{\nu_\mu}/N_{\nu_e})_{obs}$ is the ratio of observed μ and e events and $R_{MC} = (N_{\nu_\mu}/N_{\nu_e})_{MC}$ is the same ratio for Monte Carlo (MC) events.

The R' double ratios from IMB [20] and Kamiokande [21] were smaller than expectations, while the NUSEX [22] and Frejus [23] data agreed with expectations. The Baksan [24] scintillation telescopes detected upthroughgoing muons at the expected rate but gave indications of an anomalous angular distribution.

It was in 1998, during the Neutrino 1998 conference in Takayama, Japan, that SOUDAN II, MACRO and SuperKamiokande (SK) presented experimental results which showed strong indications in favour of $\nu_\mu \leftrightarrow \nu_\tau$ oscillations [25, 26, 27].

After 1998 new results of these three experiments were presented, with new and improved MC predictions for neutrino fluxes. In the past were used only uni-dimensional MC codes, Bartol96 [28] and HKKM95 [29]. Recently improved three dimensional MCs were made available by the HKKM01 [30] and FLUKA [31] groups. The new MCs yield predictions for the non oscillated and oscillated ν_μ fluxes equal to within few %; but these predictions are lower than the measured fluxes (25% at high energies, 12% at low energies). The shapes of the angular distributions for oscillated and non oscillated fluxes are equal for the four MCs to within few %.

Soudan II experiment used a modular fine grained tracking and showering calorimeter of 963 t, located underground in the Soudan Gold mine in Minnesota at a depth of 2100 meter water equivalent (mwe). The bulk of the mass consisted of 1.6 mm thick corrugated steel sheets interleaved with drift tubes. The detector was surrounded by an anticoincidence shield. Figure 1.6 shows a longitudinal cross section of the apparatus and the topologies of the events observed.

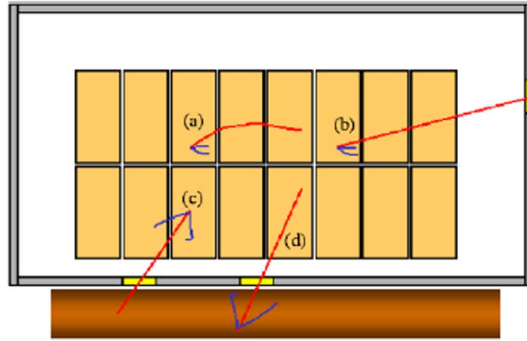


Fig. 1.6: Longitudinal cross section of the Soudan II detector and observed event topologies: (a) Fully contained Events $\langle E_\nu \rangle = 1$ GeV, (b) Partially contained Events $\langle E_\nu \rangle = 6$ GeV, (c) In-down muons $\langle E_\nu \rangle = 2.4$ GeV, (d) Up-stopping muons $\langle E_\nu \rangle = 6.2$ GeV

The Soudan II collaboration, selecting a high resolution (Hi-Res) sample of

events, reported an anomaly on the measurement of the double ratio for the whole zenith angle range ($-1 \leq \cos\theta \leq 1$) $R' = 0.69 \pm 0.12$, consistent with muon neutrino oscillations. The ν_e data agreed with the no oscillation MC predictions, while the ν_μ data were lower, with the exception of the forward zenith bin.

The MACRO experiment, located in Hall B of the Gran Sasso lab, at an average rock depth of 3700 mwe, was designed to search for rare events and rare phenomena in the penetrating cosmic radiation. It started data taking with part of apparatus in 1989; it was completed in 1995 and was running in its final configuration until the end of 2000.

The detector had a global dimension of $76.6 \times 12 \times 9.3$ m³; vertically it was divided into a lower part containing 10 horizontal layers of streamer tubes, 7 rock absorbers and 2 layers of liquid scintillators, and an upper part which contained the electronics and was covered by 1 scintillator layer and 4 layer of streamer tubes. The sides were covered with 1 vertical scintillator layer and 6 of limited streamer tubes. Figure 1.7 show a cross section of the detector and the event topologies studied.

MACRO detected upgoing ν_μ via charge current interactions $\nu_\mu \rightarrow \mu$; upgoing muons were identified with the streamer tubes (for tracking) and scintillators (for time of flight measurements).

Upthroughgoing muons came from interactions in the rock below the detector of ν_μ with $\langle E_\nu \rangle \approx 50$ GeV. MACRO compared the data with the predictions of the Bartol96, FLUKA and HKKM01 and showed that different flux simulations agree in form of the zenith angular distribution at the level of few %; but the new MCs are low by 25% for upthroughgoing muons (Fig. 1.8 (a)). *Semiconained upgoing muons* (IU) come from ν_μ interactions inside the lower apparatus. The average parent neutrino energy for these events is ~ 2 -3 GeV. *Up stopping muons* (UGS) are due to external ν_μ interactions yielding upgoing muons stopping in the detector; the *semiconained downgoing muons* (ID) are due to downgoing ν_μ 's with interaction vertices i the lower detector. The lack of time information prevents to distinguish between the two subsamples. An almost equal number of UGS and ID events is expected. The number of events and the angular distributions are compared with

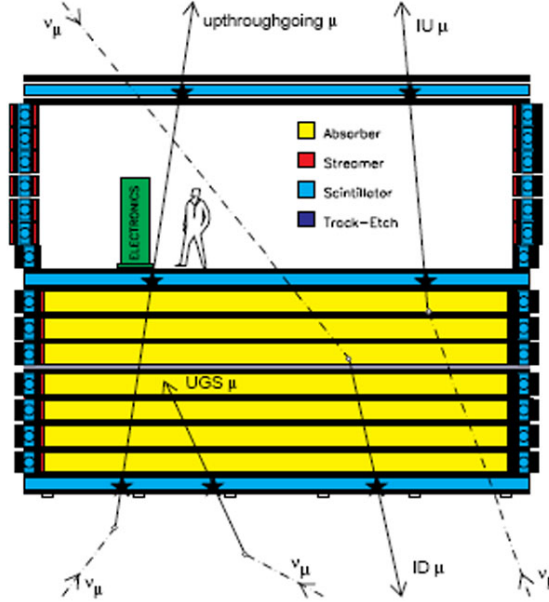


Fig. 1.7: Cross section of the MACRO detector. Event topologies induced by ν_μ interactions in or around the detector: IU $_\mu$ = semicontained Internal Upgoing μ ; ID $_\mu$ = Internal Downgoing μ ; UGS $_\mu$ = Upgoing Stopping μ ; Upthroughgoing = upward throughgoing μ .

the MC predictions without oscillations in Fig. 1.8b,c. The low energy data show a uniform deficit of the measured number of events over the whole angular distribution with respect to the Bartol96 predictions.

MACRO performed a global analysis using three samples of data corresponding to the 3 measured topologies (upthr., IU, ID+UGS). They also measured the muon energies via coulomb multiple scattering of the muons in the rock absorbers. The ratio measured/Bartol MC is shown in Fig. 1.9a: the ratio shows a deviation from 1 consistent with $\nu_\mu \leftrightarrow \nu_\tau$ oscillations.

MACRO excluded also the $\nu_\mu \leftrightarrow \nu_{sterile}$ considering the ratio between vertical events (with $-1 < \cos\theta < -0.7$) and horizontal events (with $-0.4 < \cos\theta < 0$), [32]. In this ratio most of the theoretical uncertainties on neutrino flux and cross section cancel. The measured ratio was 1.38, to be compared with $R_{\nu_\tau} = 1.61$ and

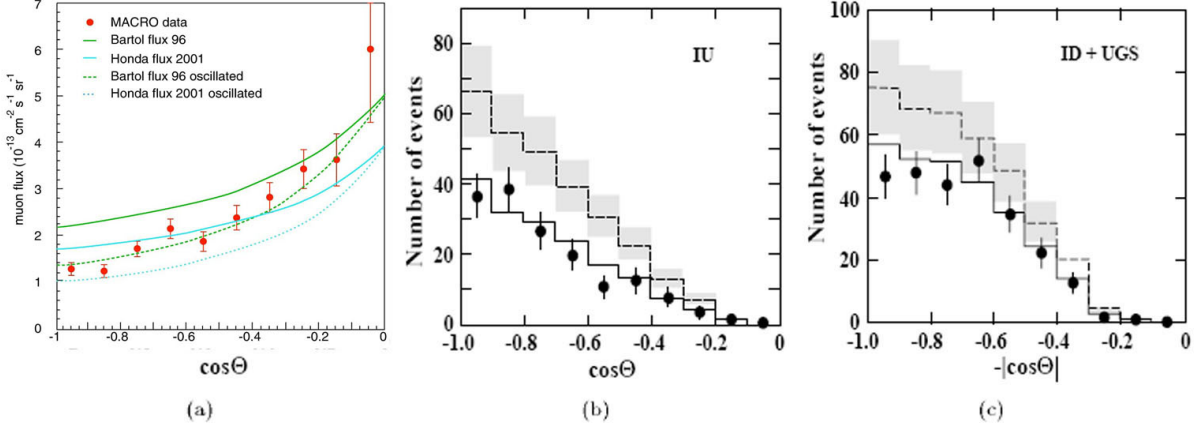


Fig. 1.8: Comparison between the zenith distribution of the MACRO upthroughgoing muons and the oscillated MC predictions given by the different MCs. Zenith distributions for (b) IU events and (c) for ID+UGS events (red points) compared with the no oscillation Bartol96 MC (green line); the dashed line is the prediction for $\nu_\mu \leftrightarrow \nu_\tau$ oscillations with $\Delta m^2 = 2.3 \cdot 10^{-3} \text{ eV}^2$ and maximal mixing.

$R_{\nu_{sterile}} = 2.03$, fig. 1.9(b); The $\nu_{sterile}$ possibility is excluded with a probability $\geq 99.8\%$.

In the final analysis in order to reduce the effects of systematic uncertainties in the MC simulations, MACRO used the following three independent ratios. It was checked that FLUKA, HKKM01 and Bartol96 MC simulations yield the same predictions to within 5%.

- i) Upthroughgoing High Energy Data: ratio between vertical nad horizontal events: $R_1 = N_{vert} / N_{hor}$
- ii) Upthroughgoing High Energy Data: ν energy measurement ratio: $R_2 = N_{lowE\nu} / N_{highE\nu}$
- iii) Low Energy Data: $R_3 = (Data/MC)_{IU} / (Data/MC)_{ID+UGS}$.

The no oscillation hypothesis has a probability $P \approx 3 \cdot 10^{-7}$ and is ruled out by $\approx 5\sigma$. By fitting the 3 ratios the $\nu_\mu \leftrightarrow \nu_\tau$ oscillation formulae, MACRO obtained

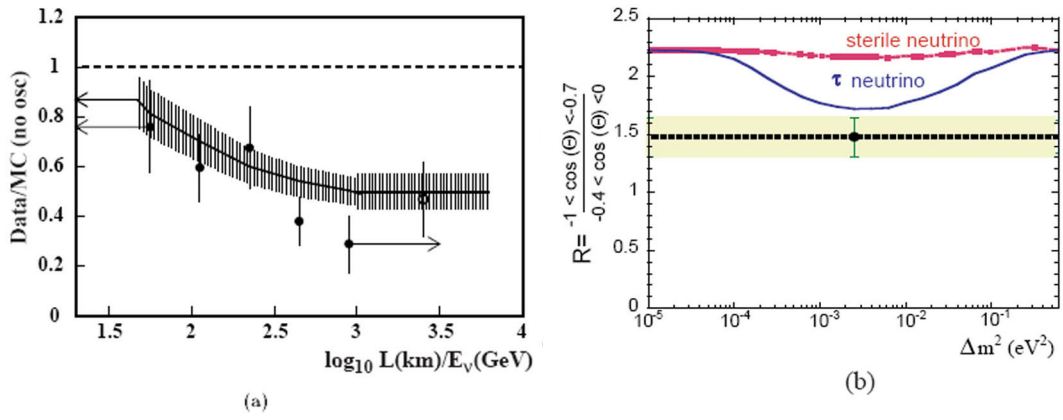


Fig. 1.9: (a) Ratio $\text{Data}/\text{MC}_{noosc}$ (Bartol96) as a function of the estimated L/E_ν for the upthroughgoing muon sample (black points). The solid line is the MC expectation assuming $\Delta m_{23}^2 = 2.3 \cdot 10^{-3} \text{eV}^2$ and $\sin^2 2\theta_{23} = 1$. The last point is obtained from the IU sample. (b) Ratio of MACRO events with $-1 < \cos \theta < -0.7$ to events with $-0.4 < \cos \theta < 0$ as a function of Δm^2 for maximal mixing. The black point is the measured value, the predictions for $\nu_\mu \leftrightarrow \nu_\tau$ and $\nu_\mu \leftrightarrow \nu_{sterile}$ oscillations are also shown.

$\sin^2 2\theta=1$ and $\Delta m^2 = 2.3 \cdot 10^{-3} eV^2$. If one adds the absolute values in comparison to the Bartol96 MC, one has the ratio $R_4=$ Upthroughgoing data/MC and $R_5=$ low energy up-going μ /MC in agreement with oscillations with maximal mixing and $\Delta m^2= 2.3 \times 10^{-3} eV^2$ (the no oscillations hypotheses is ruled out by $\sim 6\sigma$).

SuperKamiokande is a large cylindrical water Cherenkov detector of 39 m diameter and 41 m height containing 50 kt of water (the fiducial mass for atmospheric neutrino analyses is 22.5 kt); it was seen by 11146, 50-cm-diameter inner facing phototubes. The 2 m thick outer layer of water, acting as an anticoincidence, was seen by 1885 smaller outward-facing photomultiplier.

Atmospheric neutrinos are detected in SK by measuring the Cherenkov light emerging from the charged particles produced by neutrino CC interactions with the protons and oxygen nuclei. The large mass allows to collect a high statistics sample of fully contained events (FC) up to ≈ 5 GeV. Fully contained events can be further subdivided into two subsets, the so called sub-GeV (energies below 1.33 GeV) and multi-GeV events (energy above 1.33 GeV).

The *partially contained* events (PC), are defined as those CC interactions where the vertex is in the fiducial volume, but at least a primary charged particle, typically the muon, exits the detector without releasing all of its energy. In this case the light pattern is a filled circle.

Upward-going muons (UPMU), produced by neutrinos coming from below and interacting in the rock, are further classified into *stopping muons* (with average energy ~ 7 GeV) and *upthroughgoing muons* (with an average energy of 70 - 80 GeV).

In SK the particle identification is performed using likelihood functions to parametrize the sharpness of the Cherenkov rings; these are more diffuse for electrons than for muons, Fig 1.10.

The results based on the data taken from 1996 till 2001 with the detector in full configuration, are shown in figure 1.11; in the figure are reported the zenith distributions for e-like and μ -like sub-GeV and multi-GeV events, for PC events and for upward throughgoing and stopping muons.

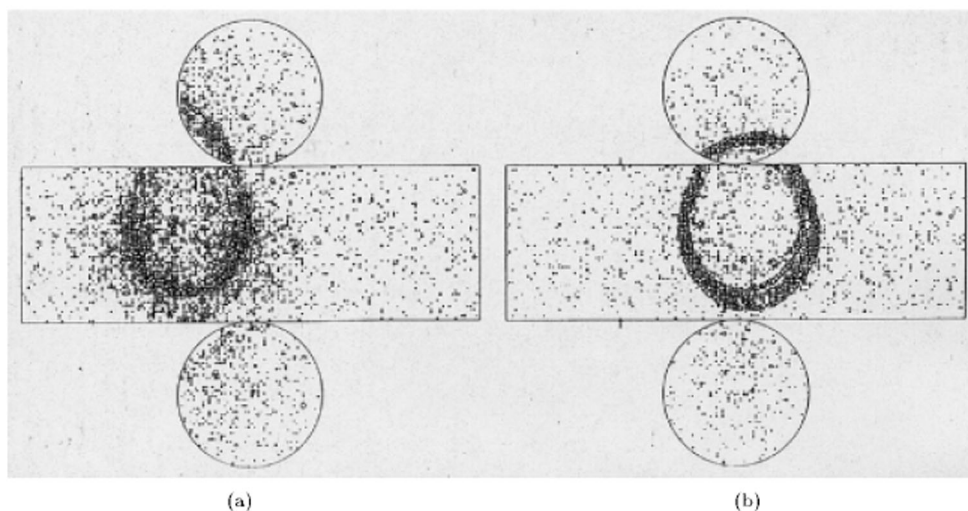


Fig. 1.10: Cherenkov rings produced in the SK detector, by (a) an electron and (b) a muon.

In SK the data for electron-like events were in agreement with the HKKM95 MC predictions in absence of oscillations, while for μ -like event were lower than the non oscillated MC predictions. The new MC predictions are low for electron-like events.

The new analyses leave free the normalization; they give, $R' = 0.658 \pm 0.016_{stat} \pm 0.032_{syst.}$ for the sub-GeV sample and $0.702 \pm 0.031_{stat} \pm 0.099_{syst.}$ for the multi-GeV sample. SK showed also a dip in the oscillation probability (Fig. 1.12(a)). The best fit of SK data corresponds to maximal mixing and $\Delta m^2 = 2.4 \cdot 10^{-3} eV^2$. Figure 1.12(b) shows the 90% allowed region in the $\sin^2\theta - \Delta m^2$ plane compared with MACRO and Soudan II.

MACRO and SK have also searched for subdominant oscillations due to possible Lorenz Invariance Violation: they established stronger upper limits [34, 35]. Solar neutrino decay has been searched by [36]

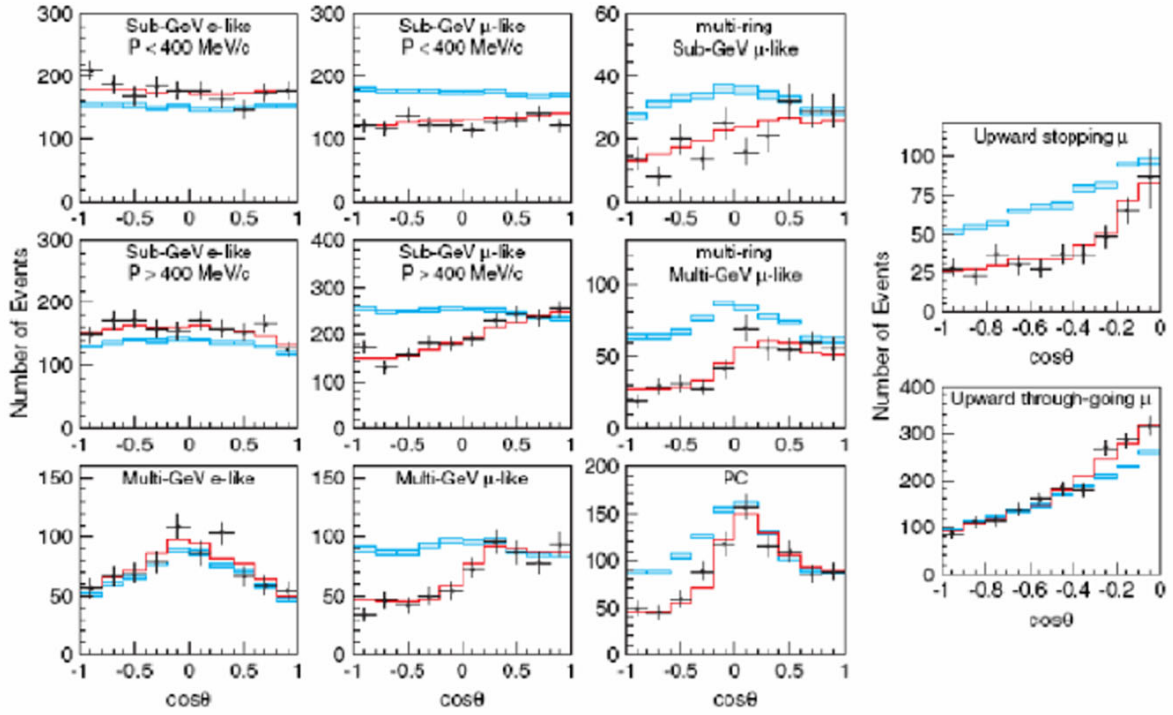


Fig. 1.11: SK data taken from 1996 till 2001. Zenith distributions for e-like and μ -like events, for PC events and for upthroughgoing and stopping muons. The boxes are the no oscillation HKKM01 predictions, the solid line refer to $\nu_\mu \leftrightarrow \nu_\tau$ oscillation with maximal mixing and $\Delta m^2 = 2.4 \cdot 10^{-3} \text{ eV}^2$

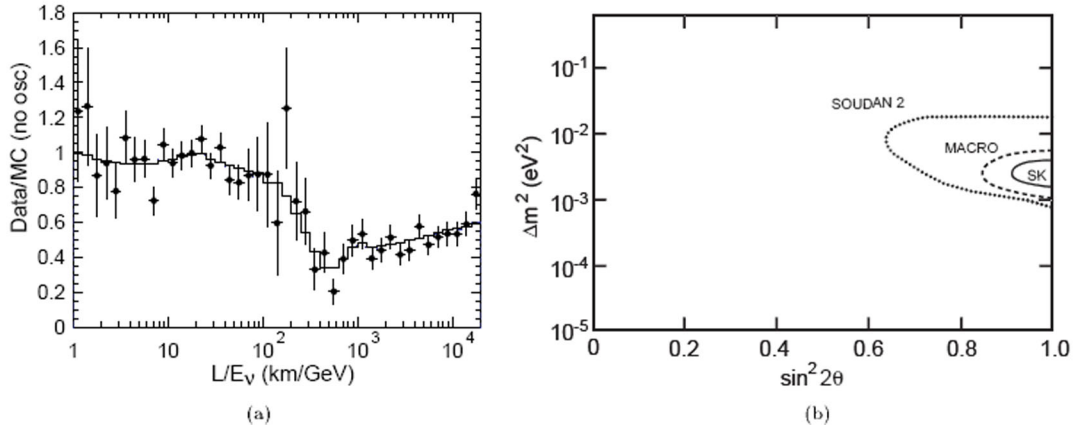


Fig. 1.12: (a) Ratio of data to MC events without neutrino oscillation (black points) as a function of the reconstructed L/E_ν compared with best fit expectation for $\nu_\mu \leftrightarrow \nu_\tau$ oscillations. (b) 90% C.L. allowed regions for oscillations obtained by SK, MACRO and Soudan II experiments

1.7 Long Base Line Experiments

Till today, two long base line experiments are providing results on neutrino oscillations in the energy region of atmospheric neutrinos.

The K2K experiment, in Japan, has already completed the data taking; the MINOS collaboration has reported the first years of data collected.

The **K2K** experiment (K2K) used the KEK accelerator to produce a ν_μ beam and pointed it to the Kamioka mine. The neutrinos are measured first by detectors located ≈ 300 meters from the proton target and then by the Super-Kamiokande (SK) detector, 250 km away.

The data, taken between June 1999 and November 2004, yielded 112 beam-originated neutrino events were observed in the fiducial Super-Kamiokande volume to be compared with a MC expectation of $158.1^{+9.2}_{-8.6}$ events without oscillations. A distortion of the energy spectrum is also observed. The probability that the observations are in agreement with no neutrino oscillation is 4.3σ away. In a two flavor oscillation scenario, the allowed region at $\sin^2 2\theta = 1$ is $1.9 \lesssim \Delta m^2 \lesssim 3.5 \cdot 10^{-3} \text{eV}^2$ at the 90% C.L., with a best-fit value of $2.8 \times 10^{-3} \text{eV}^2$ [39].

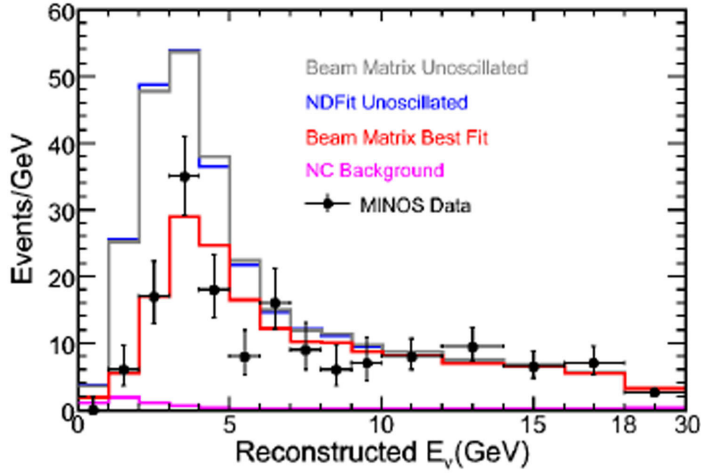


Fig. 1.13: Distributions of energy reconstructed for the neutrinos reaching the FD as expected with no oscillations, calculated with different MCs, and data points of the first measures performed by MINOS.

MINOS. In the Main Injector Neutrino Oscillation Search (MINOS) the 120 GeV/c Main Injector of Fermilab (Chicago) produces a muon neutrino beam aimed to the Soudan mine, 735 km away. There is a first detector at 1000 m from the beam production (called near detector, ND)); the main detector (far detector, FD) is in the Soudan iron mine (Minnesota). ND measures the beam before oscillations and the FD measures the distortion.

The physics goals of MINOS are: an accurate measurement of $\sin^2 2\theta_{23}$ and Δm_{23}^2 ; search for $\nu_\mu \leftrightarrow \nu_e$ oscillations; search or constrain exotic phenomena ($\nu_{Sterile}$, ν decay); compare ν , $\bar{\nu}$ oscillations.

Data taking started in 2005. The measurements performed were obtained with the beam optimized in low energy configurations. The neutrino energy spectra reconstructed in the ND are used to predict the neutrino energy distribution in the FD. The prediction together with the data obtained for 1.2×10^{20} pot are shown in figure 1.13 and given in the table 1.2.

The data agree with $\nu_\mu \leftrightarrow \nu_\tau$ oscillations with parameters $|\Delta m_{32}^2| = (2.74_{-0.26}^{+0.44}) \times 10^{-3} eV^2$ and $\sin^2 2\theta_{23} = 1_{-0.13}$.

Data Sample	FD data	Expected	Ratio Data/MC
ν_μ (>30 GeV)	215	336.0 ± 14.4	0.64 ± 0.05
ν_μ (>10 GeV)	122	238.7 ± 10.7	0.51 ± 0.05
ν_μ (<5 GeV)	76	168.4 ± 8.8	0.45 ± 0.06

Tab. 1.2: First MINOS measurements after 2 years data taking. The MC used for the expected and ratio values is the Matrix Method

OPERA is the only long baseline experiment that will study $\nu_\mu \leftrightarrow \nu_\tau$ oscillations in ν_τ appearance mode. The electronic detector is almost complete and have already performed a first test-run with the CNGS beam. The brick production is in progress. Details of the OPERA experiment will be given in the next chapter.

1.7.1 Direct Neutrino Mass Search

It is not really correct to speak of the mass of ν_e, ν_μ, ν_τ since the mass are ν_1, ν_2, ν_3 . It is nevertheless usual to speak of searches for ν_e, ν_μ, ν_τ mass.

The *electron neutrino mass* is studied in tritium decays (corresponding to $n \rightarrow p e^- \bar{\nu}_e$) investigating the electron energy spectrum (β spectrum).

The phase-space region of low energy anti-neutrinos, where the highest sensitivity to the neutrino mass is achieved, corresponds to the very upper end of the β -spectrum.

The Mainz and Troitsk [41] tritium experiments, gave $m_{\nu_e} \leq 2.2$ eV at 90% C.L. Recently the Mainz group installed a new electrode system to check new ideas for the KATRIN experiment to reduce the background by a factor ~ 3 trying to reach a sensitivity of 0.2 eV at 90%.

The muon neutrino mass was investigated in the two-body decay of a pion:

$$\pi^+ \rightarrow \mu^+ + \nu_\mu \quad , \quad \pi^- \rightarrow \mu^- + \bar{\nu}_\mu$$

The present limit is [42]:

$$m(\nu_\mu) < 190 \text{ keV} \quad (90\%C.L)$$

For what concerns tau neutrino mass, the most sensitive investigation comes from experiments at LEP [43]:

$$m(\nu_\tau) < 18.2 \text{ MeV} \quad (95\%C.L)$$

1.7.2 Neutrinoless double- β decay

The neutrinoless double β decay ($0\nu\beta\beta$) is an Lepton-violating decay,

$$(A, Z) \rightarrow (A, Z + 2) + 2e^-$$

in which a nucleus, containing Z protons and $A - Z$ neutrons decays, to a nucleus with $Z + 2$ protons emitting two electrons. Observation of this reaction would show that the neutrinos were indeed Majorana particles.

It was shown that the amplitude for $0\nu\beta\beta$ is proportional to the quantity

$$\left| \sum_i m_i U_{ei}^2 \right| \equiv | \langle m_{\beta\beta} \rangle |, \quad (1.21)$$

commonly referred to as the *effective Majorana mass for neutrinoless double beta decay* [44].

Several approaches were used to search for $0\nu\beta\beta$ decay. The most sensitive experiments was the Heidelberg-Moscow experiment [45] that reported an upper limit on the effective neutrino mass

$$m_{ee} \leq 0.35 \text{ eV} \quad (90\% C.L.).$$

In 2001, a subgroup of the Heidelberg-Moscow collaboration published evidence for a $0\nu\beta\beta$ decay signal. This signal corresponds to a mass $m_{\beta\beta} \sim 0.39 \text{ eV}$ with a significance of 2-3 σ [46]; however, this claim is controversial and cannot be considered a definitive proof [47].

Chapter 2

The OPERA experiment

2.1 The OPERA experiment

OPERA (**O**scillation **P**roject with **E**mulsion-**t**Racking **A**pparatus) [48] is a long baseline experiment designed primarily to conclusively test the $\nu_\mu \rightarrow \nu_\tau$ oscillation hypothesis by means of the direct observation of ν_τ in an initially pure ν_μ beam. The detector is located in the Hall C of the Gran Sasso Underground Laboratory at a distance of 730 km from CERN, where the neutrino beam (CNGS)[49] has been constructed. The average energy of the neutrinos is above the τ lepton production threshold, in the oscillation parameter region indicated by atmospheric neutrino experiments.

2.1.1 The CNGS neutrino beam

The CNGS neutrino beam was designed and optimized for the study of $\nu_\mu \rightarrow \nu_\tau$ oscillations in appearance mode, by maximizing the number of charged current (CC) ν_τ interactions at the LNGS site. A 400 GeV proton beam is extracted from the CERN SPS in 10.5 μ s short pulses with a design intensity of 2.4×10^{13} proton on target (p.o.t) per pulse. The proton beam is transported through the transfer line TT41 to the CNGS target T40 [49]. The target consists of a series of thin graphite rods helium-cooled. Secondary pions and kaons of positive charge produced in the

target are focused into a parallel beam by a system of two magnetic lenses, called horn and reflector, Fig. 2.1.

A 1000 m long decay-pipe allows the pions and kaons to decay into muon-neutrinos and muons. The remaining hadrons (protons, pions, kaons, ...) are absorbed by an iron beam-dump. The muons are monitored by two sets of detectors downstream of the dump; they measure the muon intensity, the beam profile and its centre. Further downstream the muons are absorbed in the rock while neutrinos continue to travel towards Gran Sasso (Fig. 2.1).

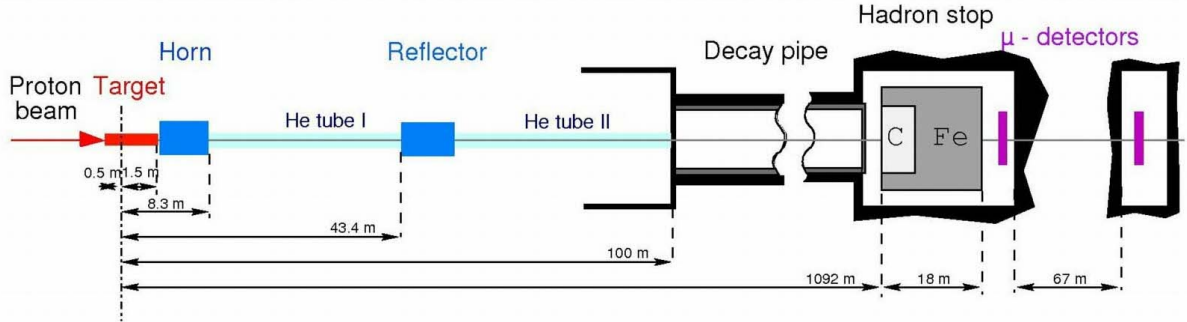


Fig. 2.1: Sketch of the CNGS components at the SPS of CERN

The average neutrino energy at the LNGS location is 17 GeV. The $\bar{\nu}_\mu$ contamination is 4%, the ν_e and $\bar{\nu}_e$ contaminations are lower than 1%, while the number of prompt ν_τ from D_s decay is negligible. The average L/E_ν ratio is 43 km GeV^{-1} . Due to the Earth curvature neutrinos from CERN enter the LNGS halls with an angle of about 3 degrees with respect to the horizontal plane. Assuming a CNGS beam intensity of 4.5×10^{19} p.o.t. per year and a five year run, about 31000 CC plus neutral current (NC) neutrino events will be collected by OPERA from interactions in the lead-emulsion target. Out of them 95 (214) CC ν_τ interactions are expected for $\Delta m^2 = 2 \times 10^{-3} \text{ eV}^2$ ($3 \times 10^{-3} \text{ eV}^2$) and $\sin^2 2\theta_{23} = 1$. Taking into account the

overall τ detection efficiency the experiment should gather $10 \div 15$ signal events with a background of less than one event.

About 50000 muons will be produced in the CC interactions of the ν_μ in the rock upstream of OPERA.

2.1.2 The detector

The OPERA apparatus consists of 2 identical parts called *super-modules* (SMs). Each super-module consists of ~ 100000 lead/emulsion bricks arranged in 31 target planes (Fig. 2.2), each brick wall is followed by two scintillator planes with an effective granularity of $2.6 \times 2.6 \text{ cm}^2$.

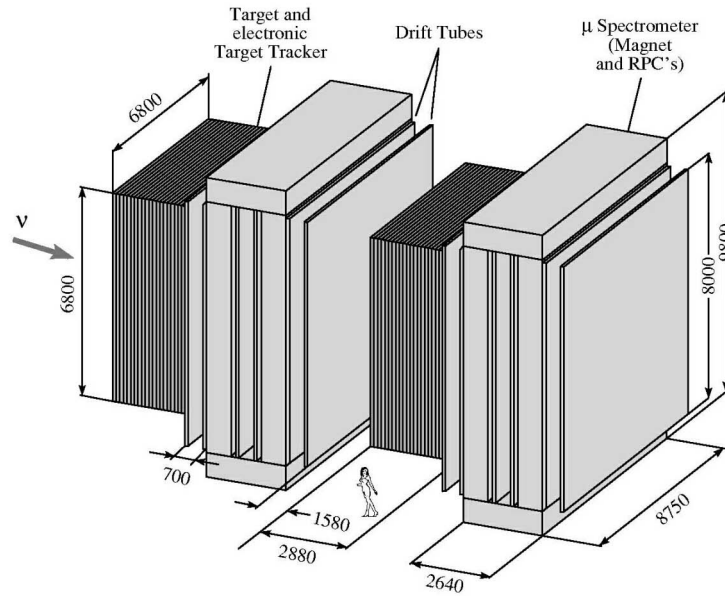


Fig. 2.2: Schematic drawing of the OPERA experiment

These planes serve as trigger devices and allow selecting the brick containing a neutrino interaction. A muon spectrometer at the downstream end of each SM

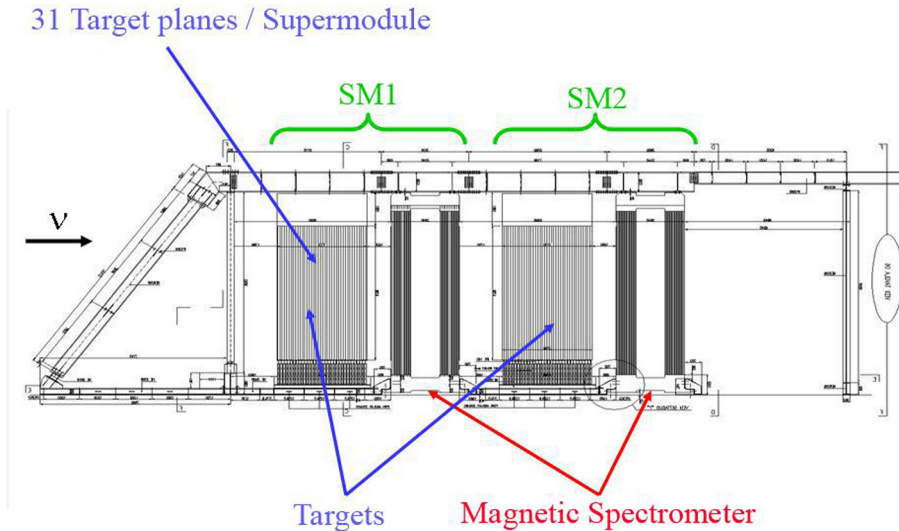


Fig. 2.3: Side view of OPERA detector. From the left is visible the large size anti-coincidence detector placed in front of SM1.

allows to measure the muon charge and momentum. A large size anti-coincidence detector placed in front of the first SM allows to veto (or tag) interactions occurring in the material and in the rock upstream of the target (Fig. 2.3).

Electronic detectors

Target Tracker. Between two consecutive lead/emulsion brick walls, electronic detectors trigger the ν interaction and identify the brick containing the candidate event.

An electronic target tracker module consists of two planes of 6.6 m long scintillator strips in each transverse directions (X and Y, horizontal and vertical) (see Fig. 2.4). The strips, 2.6 cm wide and 1 cm thick, have Wave Length Shifting (WLS) fibers for readout by 64 multi-anode photomultiplier tubes. The transverse resolution is about 1.5 cm for CC events and 3.0 cm for NC events.

The selection of the brick containing the neutrino interaction vertex is performed by combining different algorithms based on the observed transverse and longitudinal

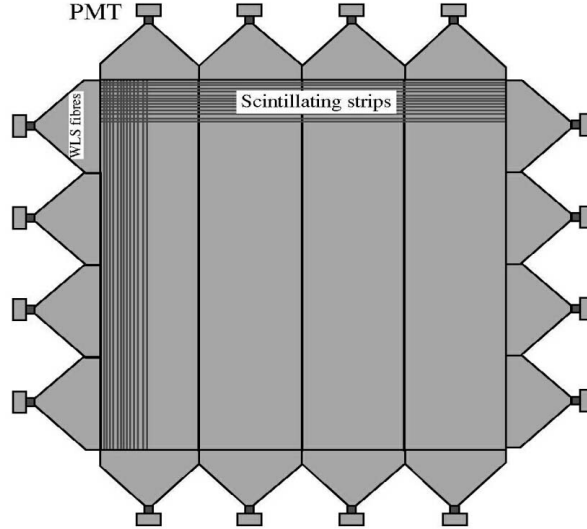


Fig. 2.4: Schematic structure of a Target Tracker scintillator plane

event profiles as well as on the presence of individual reconstructed tracks. The overall efficiency to find the right brick is $\sim 80\%$.

Muon Spectrometers. In each supermodule, at the end of the target section, a spectrometer measures the muon momentum and charge. These measurements are needed for the study of the muonic τ -decay channel and for the suppression of the background from the decay of charmed particles.

Each spectrometer magnet is made of two magnetized iron walls magnetically connected by an upper and a lower yoke. The magnet walls are made of 12 iron layers 50 mm thick, with 11 gaps of 20 mm to house the Inner Trackers (Fig. 2.5). Externally, the transverse dimensions of a magnet are 8.75 m (horizontal) and 10 m (vertical) providing the needed geometrical acceptance for muons originating upstream in the target volume.

Each muon spectrometer is equipped with six planes of Precision Trackers (PT),

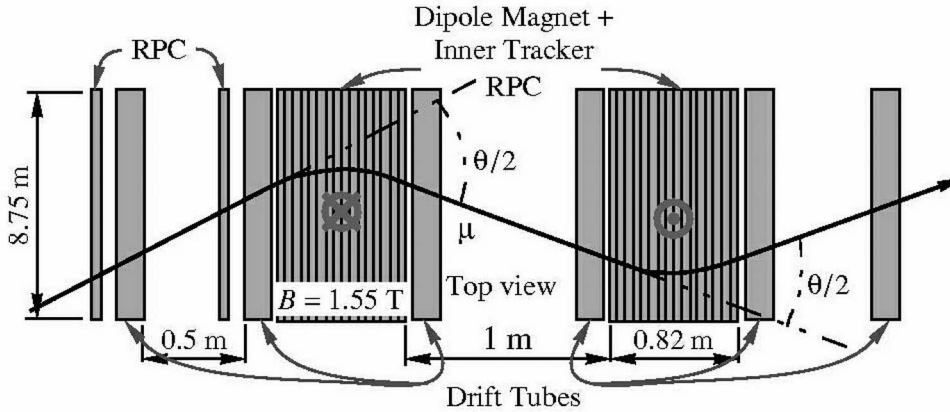


Fig. 2.5: Top view of an OPERA spectrometer

two upstream, two between the iron walls and two downstream (Figure 2.6). The PTs consist of vertical drift tube planes with an intrinsic resolution of 0.3 mm in the bending direction. Allowing for some misalignment, an overall resolution on each measured coordinate of 0.5 mm is expected. The momentum resolution $\Delta p/p$ is expected to be better than 30% in the relevant kinematical domain.

11 + 11 Inner Trackers (RPC chambers) are inserted between the iron plates of the two walls of each magnet. On each face of the chambers, the induced pulses are collected by 3 cm wide pickup copper strips in the horizontal and vertical directions. The Inner Trackers allow a coarse tracking inside the magnet to identify muons and facilitate track matching between the Precision Trackers. They also provide a measurement of the tail of the hadronic energy leaking from the target and of the range of muons which stop in the iron.

Emulsion Cloud Chambers (ECC)

The ν_τ appearance search is based on the observation of τ^- events produced by CC interactions, with the τ^- decaying in all possible decay modes. The possible τ^-

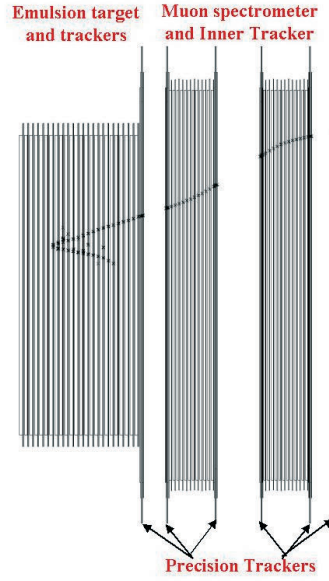


Fig. 2.6: A schematic layout of the detectors installed in one OPERA supermodule. It is also shown a ν_μ CC interaction. The muon track is bent in the spectrometer.

decays are:

$$\begin{aligned}
 \tau^- &\rightarrow e^- \nu_\tau \bar{\nu}_e \\
 \tau^- &\rightarrow \mu^- \nu_\tau \bar{\nu}_\mu \\
 \tau^- &\rightarrow h^- \nu_\tau (n\pi^0) \\
 \tau^- &\rightarrow 3\pi \nu_\tau
 \end{aligned}
 \tag{2.1}$$

Since the expected event rate is small, it is crucial to separate efficiently the ν_τ CC events from all the other flavor neutrino events, and to keep the background at a very low level. For this purpose, the detectors will have to identify the event by exploiting the τ decay specific properties, characterized by a short lifetime and the presence of missing transverse momentum due to the ν_τ in the final state.

In order to have large mass (1.8 kton) and high granularity the emulsion sheets are interleaved with 1 mm thick lead plate. The emulsions used to build ECC are $44\mu\text{m}$ -thick layers placed at the up and down surfaces of a $205\mu\text{m}$ -thick plastic base (fig. 2.7).

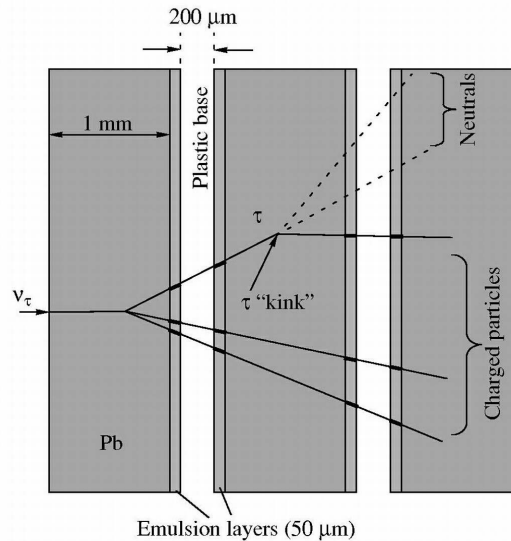


Fig. 2.7: Schematic view of an ECC cell. With four track segments in the emulsion film it is possible to reconstruct in space the τ decay kink.

The basic structure of the emulsion detector is called Emulsion Cloud Chamber (ECC) and is composed ECC *bricks*. Each brick is made of 57 emulsion sheets interleaved with 56 lead plates 1 mm thick. The *Brick Assembling Machine* (BAM) consists of robotized stations that assemble and pack the bricks. The BAM has produced till now 7222 bricks. At the downstream end of each brick a small plastic box, containing two emulsion sheets, named *Changeable Sheets* (CS) is further attached (Fig. 2.8). The CS can be easily removed and analyzed, without opening the whole brick. The information of the CS is used for a precise prediction of the position of the tracks in the most downstream films of the brick, hence guiding the so called scan-back vertex finding procedure.

The bricks produced by the BAM are allocated on circular drums that are then handled by the *Brick Manipulator System* (BMS), which is made of two robots, each operating at one side of the detector. An arm is used to insert the bricks. The extraction of a brick, in the region indicated by electronic detectors, is done by a vacuum sucker of the BMS.

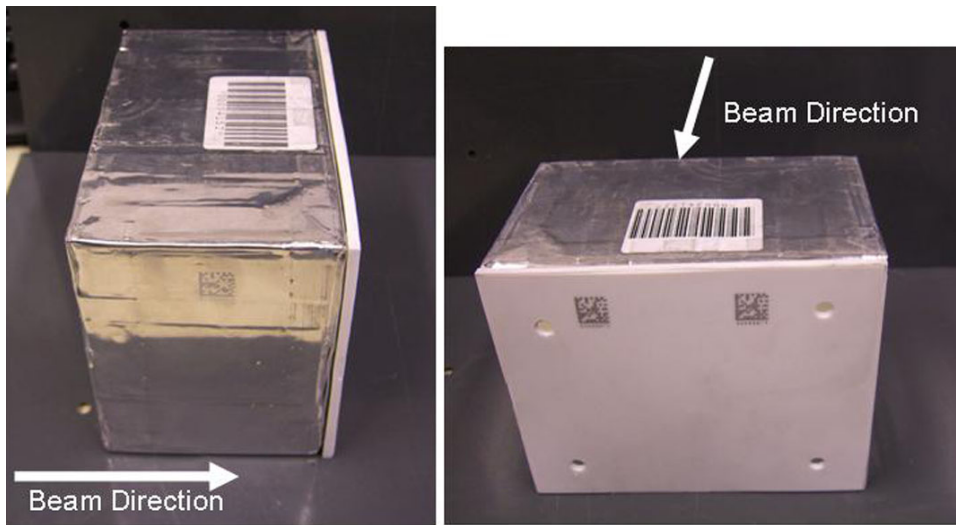


Fig. 2.8: Photography of an OPERA brick delivered by the BAM. The picture shows the CS box attached to the brick at its downstream side.

The dimensions of a brick are $12.5 \times 10.2 \times 7.5 \text{ cm}^3$, the weight is 8.3 kg. In terms of radiations length, a brick corresponds to a thickness of $10 X_0$ which is long enough to allow the identification of electrons by electromagnetic showers and to measure momentum by multiple Coulomb scattering following the tracks in consecutive emulsion sheets [50].

The process of installing bricks on the walls has started; when this task will be completed almost 200000 bricks will be installed on the walls.

Details on the emulsions and of the techniques of analysis will be given in Chapters 3 and 4.

2.1.3 Data-acquisition, brick extraction, microscope scanning

The electronic detectors provide the trigger for brick extraction, and a probability map on the preceding brick walls. The brick located in the most probable area is extracted by the BMS.

The candidate bricks are transported in a dedicated area, where the CSs are

removed for a prompt analysis in order to confirm/reject the neutrino interaction. If the CSs do not confirm the interaction, the brick is equipped with two new emulsion sheets and placed back in the detector.

If the CSs confirm the presence of the interaction, the brick is transported to the outside laboratories and exposed for about one day to cosmic-ray muons. This procedure allows to provide emulsions with enough muons for a correct alignment: the bricks are exposed without CSs, so as to separate the traces referring to neutrino events from the ones referring to cosmic-ray muons.

Subsequently, the brick is disassembled and each emulsion is labeled with an Id number and a set of spots, which will provide a reference system during the scanning. Emulsions are developed at LNGS by means of an automatic system, and sent to the scanning laboratories.

2.2 Physics performances: $\nu_\mu \rightarrow \nu_\tau$ search

2.2.1 τ detection

The signal of the occurrence of $\nu_\mu \leftrightarrow \nu_\tau$ oscillations is the CC interaction of ν_τ 's in the detector target ($\nu_\tau N \rightarrow \tau^- X$), through the decay topologies of its decay into an electron, a muon or a single charged hadron. The branching ratios (BR) of the three single-prong decay modes are 17.8%, 17.7% and 49.5% for the electronic, muonic and hadronic channel, respectively [51]. For the typical τ energies expected with the CNGS beam one obtains the decay length distribution shown in Fig. 2.9.

When a τ is produced in a lead plate it will decay either in the same plate (short decay) or further downstream (long decay), see Fig. 2.10. For long decays, the τ is detected by measuring the angle between the charged decay daughter and the parent τ direction. For this measurement the directions of the tracks before and after the kink are reconstructed (in space) by means of the pair of emulsion films sandwiching the lead plate where the decay vertex occurred. The τ can also decay in the same lead plate in which the primary interaction occurred or in one of the films or in the plastic base downstream of the vertex plate (short decay). The kink angle

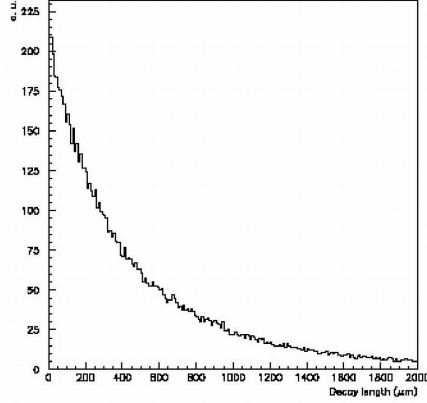


Fig. 2.9: Expected τ decay length distribution in emulsion.

is reconstructed, albeit with a lower angular resolution, from the track segments in the emulsion layers on either side of the base. A fraction of the short decays is detectable by measuring a significant impact parameter (IP) of the daughter track with respect to the tracks originating from the primary vertex.

The detection of the τ decay into an electron benefits from the dense ECC structure, which allows electron identification through its showering in the downstream emulsion sheets.

2.2.2 Background

For the muonic decay mode the presence of the penetrating (often isolated) muon track allows an easier event vertex finding. The potential background from large angle scattering of muons produced in ν_μ CC interactions can be reduced to a tolerable level by applying cuts on the kink angle and on the transverse muon momentum at the decay vertex.

Hadronic decay modes have the largest branching ratio but are affected by background due to hadron reinteractions. One of the primary hadrons may interact in the first lead plates and simulate the charged single-prong decay of the τ . Kinematic cuts are used to reduce this background.

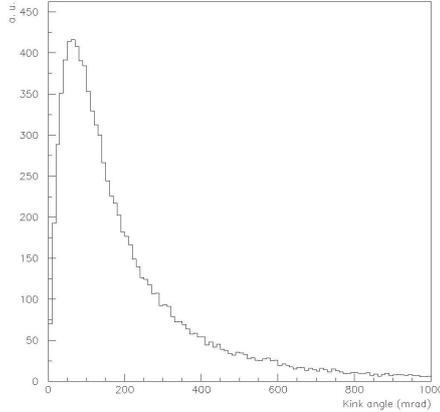


Fig. 2.10: Expected τ kink angle distribution for the $\tau \rightarrow e$ decay mode.

An important tool for background rejection is the determination of the transverse momentum of the daughter particle with respect to the direction of the τ track candidate. For $\tau \rightarrow e$ decays the ECC technique is well suited to identify electrons and to determine their energy by measuring the density of track segments associated to the shower in the brick. For charged hadrons and muons, the momentum is deduced from the measurement of the multiple scattering in the lead plates.

The background due to prompt ν_τ production in the primary proton target and in the beam dump is negligible. The number of interactions due to these ν_τ is estimated [52] to be $O(10^{-6}) \times N_{CC} \times \epsilon_\tau$, where N_{CC} , the total number of ν_μ CC events collected, is of the order $O(10^4)$ and the τ detection efficiency, ϵ_τ is 10%. The total number of background events in 5 years of data taking is estimated to be 0.71.

2.3 First test run with the CNGS neutrino Beam

The first test run with neutrinos coming from CERN was from 18 to 30 August 2006 with a total integrated intensity of 7.6×10^{17} protons on target (p.o.t). The beam was on for a time equivalent to about 5 days. The low intensity was partly due to the chosen SPS cycle and to the intensity of the spill that was 55% of the nominal value during the first part of the run and 70% during the second part.

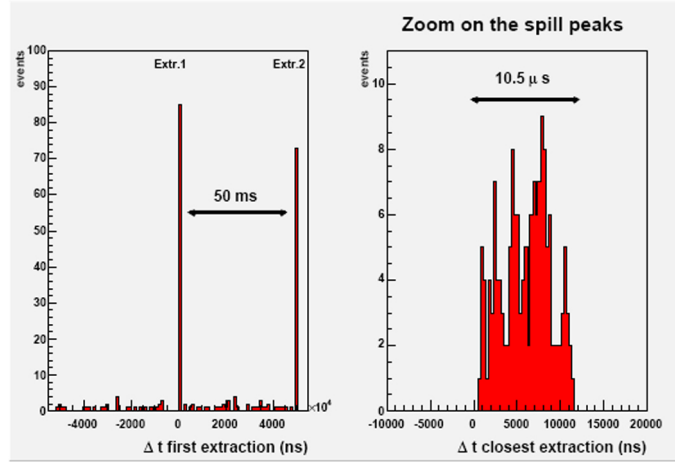


Fig. 2.11: Time distribution of events collected in the neutrino run. The event time difference with respect to the closest extraction is shown in the right histogram.

Before data taking a GPS clock was used to synchronize and fine tune the CERN accelerators and OPERA.

The OPERA detector started collecting neutrino interactions from the very first beam spills with nearly all electronic detectors operating. Altogether, 319 neutrino events, with an estimated 5% systematic uncertainty, were taken by OPERA during the August run. This is consistent with the 300 expected events for the given integrated intensity.

The event analysis was performed in two ways. In the first one the event timing information was treated as a basic selection tool, since the time window of beam events is well sized in a $10.5 \mu\text{s}$ interval, while the uniform cosmic ray background corresponded to 10^{-4} of the collected statistics (see Fig. 2.11). The second analysis dealt with the reconstruction of track-like events disregarding timing informations.

In Fig. 2.12 some neutrino events are shown; they are classified as: (i) CC neutrino interactions in the rock upstream of the detector or in the material present in the hall C before OPERA leading to a penetrating muon track (fig. 2.12, top left); (ii) CC and (iii) NC neutrino interactions in the target material (fig. 2.12, top right and bottom right) and (iv) CC interaction in the iron of the spectrometers

(2.12, bottom left).

The θ angular distribution with respect to the horizontal axis obtained by selecting single-track events is shown in figure 2.13. Events were selected with a minimum number of six layers of fired RPCs in each spectrometer. In the same figure, the distribution of simulated cosmic rays muons from [53] is also shown.

A gaussian fit to the θ angle of the events on-time with the beam (shown in the inset of figure 2.13) yielded a mean muon angle of 3.4 ± 0.3 degrees in agreement with the value of 3.3 deg expected from neutrinos originating from CERN and travelling under the earth surface to the LNGS underground halls.

For what concerns the analysis of the CS plane detector, 9 muons produced by neutrino interactions in the rock surrounding the detector crossed the CS plane surface. Five muon tracks predicted by the electronic detectors were found by scanning the emulsion films. This inefficiency can be traced back to the tight cuts applied in this preliminary analysis and on the effective decrease of the fiducial volume due to the dead space between adjacent emulsion films ($\approx 10\%$) and to emulsions scanning which excluded 3 mm from the film edge. These cuts lead to an overall dead space of $\sim 20\%$. A remarkable result of this run was the proof of the capability for passing from the centimetre scale of the electronic target tracker resolution to the micrometric resolution of nuclear emulsions. The angular difference between predicted and found tracks is better than 10 mrad, largely dominated by the electronic detector resolution. Figure 2.14 shows the display of one of the 5 reconstructed events.

The success of this first OPERA run with CNGS neutrinos is the first step towards the operation of the complete detector.

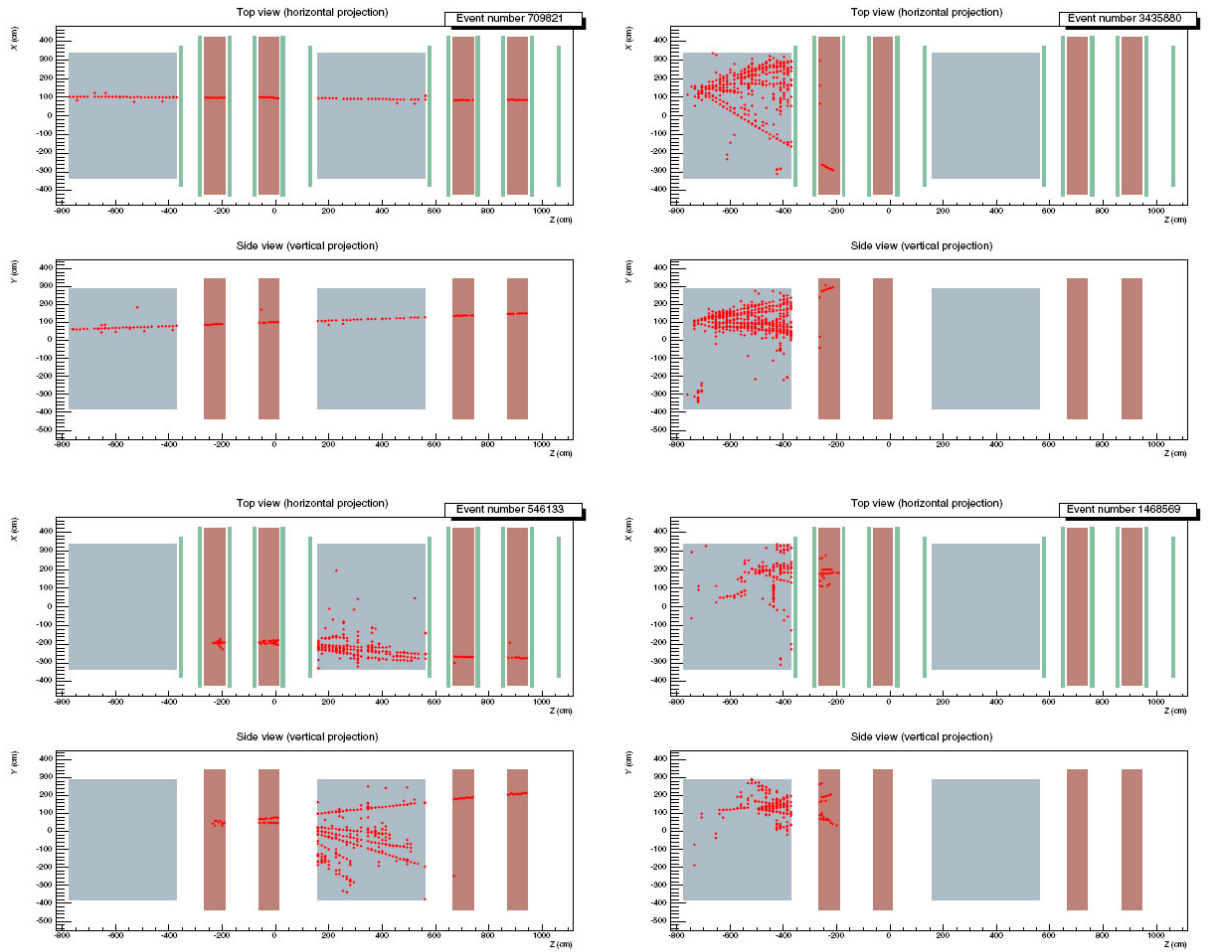


Fig. 2.12: Display of neutrino events from the CNGS run. For each event the top and side views are shown, respectively. The targets are indicated in blue, the spectrometers in light brown, TT and RPC hits in red.

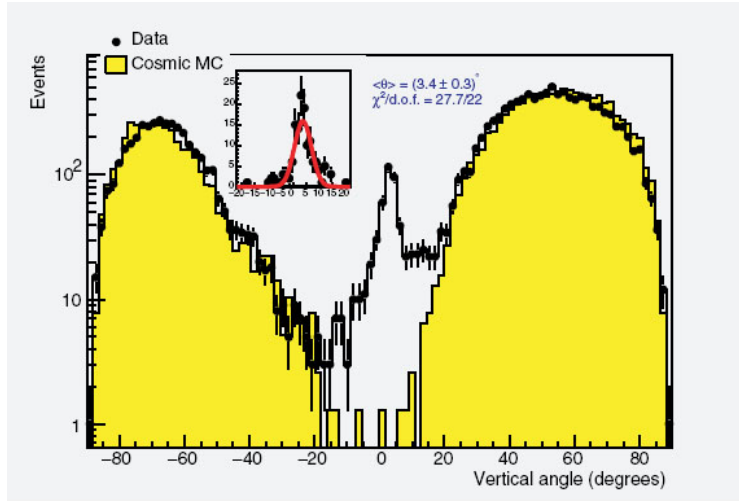


Fig. 2.13: Angular distribution of beam induced and cosmic-ray-muon events taken with the electronic detectors (black points). The histogram indicates the prediction from a cosmic ray simulation [53]. The inset shows the angular distribution of on-time beam events.

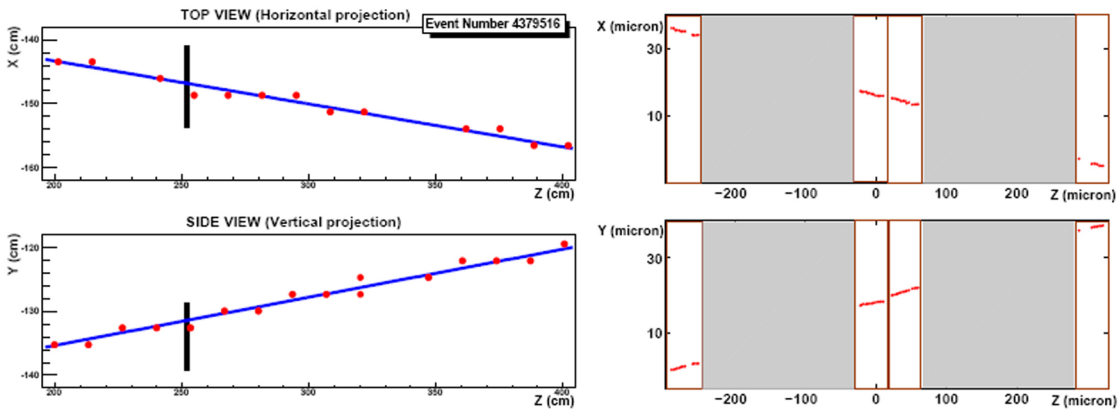


Fig. 2.14: Left: display of one event with the muon passing through the CS detector plane. Only hits of the electronic detectors close to the CS plane are shown, the vertical segment indicates the position of the CS doublet intercepted by the track. Right: display of the corresponding four micro-tracks reconstructed in the CD doublet.

Chapter 3

OPERA emulsion properties

3.1 Introduction

The starting point of the long and successfully life of the nuclear emulsion technique could be considered when H. Becquerel discovered radioactivity by observing the blackening of photographic plates accidentally in contact with uranium salts, in 1896.

Since then a lot of fundamental studies has been done using nuclear emulsions, among them we remember the discovery of the pion in 1947 by observing the $\pi \rightarrow \mu \rightarrow e$ decay chain in nuclear emulsions exposed to cosmic rays [58].

During the 50's and 60's emulsions were used for cosmic ray experiments, electromagnetic shower energy measurements and momentum measurements and several other particles were discovered.

Nuclear emulsions were successfully used in neutrino experiments like WA17 at CERN for charmed particles searches in neutrino charged current interactions [59], E531 at Fermilab for the measurement of charmed particle lifetimes in neutrino interactions [60], and WA75 at CERN searching for beauty particle production induced by a 350 GeV/c π^- beam [61]. Furthermore, the DONUT collaboration [62] observed the τ neutrinos by using nuclear emulsion.

Nuclear emulsion is still the detection technique with the best known three-

dimensional spatial resolution, less than 1 μm , and zero intrinsic dead time. The use of nuclear emulsions in massive experiments has made possible thanks to the development of automatised scanning systems during the last two decades.

3.2 Basic properties of emulsions

Emulsions used for charge particles recording are a mixtures of inorganic and organic components. Usually an equal amount of silver halide micro-crystals (a few tenth of a micron in diameter) and a "gel phase", consisting mainly of gelatin with a variable quantity of water and small amount of glycerol, sensitizes and possibly other organic substances.

The equilibrium water content depends on the relative humidity and temperature of the air in contact with the emulsion [56]. The silver halide is usually in the form of silver bromide crystals with a small amount of iodine in the crystal lattice; there have been also attempts to replace the gelatin matrix of the emulsion by synthetic materials, but thus far without complete success.

The sensitivity of the emulsion depends by the size of the silver halide crystals; large grains are more sensitive to ionizing radiation than small ones. Usually, a low sensitivity emulsion is used to detect high-energy particles, as there is plenty of energy available to free electrons. However, a more sensitive emulsion is required to detect very high-energy particles as they deposit very little energy along their tracks and travel too fast to be trapped by the silver halide crystals [57].

The size of the microcrystals in the OPERA emulsions is $\sim 0.2 \mu\text{m}$ and is well controlled by the current industrial technologies developed for photographic films

Nuclear emulsions are almost like standard photographic emulsions, but with some peculiar characteristics: in nuclear emulsions silver halide crystals are very uniform in size and sensitivity; the silver to gelatin ratio is much higher than in a conventional emulsion and there are very few crystals that may be developed without exposure to a charged particle.

A ionizing particle crossing emulsions, encounters a crystal and may render it

developable. After development, followed by fixing and washing to remove the undeveloped crystals, the gelatin became transparent and with a microscope the path of the particle that has travelled through the emulsion is visible as a trail of small dark silver grains.

3.2.1 The latent image

Silver halide crystals of an emulsion have the property to absorb energy when opportunely excited by light or charged particles. This absorption sensitizes the crystals in such a way that under the action of a chemical reducing agent, conversion of the halide to metallic silver will proceed more rapidly than in an unirradiated crystal. The physical property in the crystal that makes it developable is called *latent image*.

Any theory of latent-image formation must account for the way that light photons absorbed at random within the grain can produce these isolated aggregates of silver atoms. Most current theories of latent-image formation are modifications of the mechanism proposed by R. W. Gurney and N. F. Mott in 1938.

When solid silver bromide is formed, as in the preparation of a photographic emulsion, the silver atoms each give up one orbital electron to a bromine atom. The silver atoms, lacking one negative charge, have an effective positive charge and are known as silver ions (Ag^+). The bromine atoms, on the other hand, have gained an electron - a negative charge - and have become bromine ions (Br^-).

A crystal of silver bromide is a regular cubical array of silver and bromide ions. A crystal of silver bromide in a photographic emulsion is not perfect; a number of imperfections are always present. First, within the crystal, there are silver ions that do not occupy the "lattice position", but rather are in the spaces between. These are known as interstitial silver ions. The number of the interstitial silver ions is, of course, small compared to the total number of silver ions in the crystal. In addition, there are distortions of the uniform crystal structure. These may be "foreign" molecules, within or on the crystal, produced by reactions with the components of the gelatin, or distortions or dislocations of the regular array of ions. These may be classed together and called "latent-images sites."

The Gurney-Mott theory envisions latent-image formation as a two-stage process.

When a photon of light of energy greater than a certain minimum value is absorbed in a silver bromide crystal, it releases an electron from a bromide (Br^-) ion. The ion, having lost its excess negative charge, is changed to a bromine atom. The liberated electron is free to wander about the crystal, where it may encounter a latent image site and be "trapped" there, giving the latent-image site a negative electrical charge. This first stage of latent-image formation, involving transfer of electrical charges by means of moving electrons, is the *electronic conduction stage*.

The negatively charged trap can then attract an interstitial silver ion because the silver ion is charged positively. When such an interstitial ion reaches a negatively charged trap, its charge is neutralized, an atom of silver is deposited at the trap, and the trap is "reset". This second stage of the Gurney-Mott mechanism is called the *ionic condition stage*, since electrical charge is transferred through the crystal by the movement of ions, that is, charged atoms. The whole cycle can recur several, or many, times at a single trap, each cycle involving absorption of one photon and addition of one silver atom to the aggregate.

In this way, the absorption of energy in a excited crystal of silver halide leads to a concentration of a few silver atoms into an aggregate which can act as a development centre, i. e. a latent image.

The formation and preservation of the *latent image* depends on external conditions such as: temperature, humidity, pressure. As temperature and humidity increase, the sensitivity decreases and the latent image is less stable (*fading*). The fading can be artificially induced in order to erase the image of unwanted tracks accumulated before the exposition (*refresh*). Moreover, in particular conditions, it is possible to refresh emulsion without spoiling their sensitivity.

3.2.2 Development and fixation

Photographic development is the process by which the latent image in an emulsion is made visible by the reduction of silver ions to metallic silver. The reducing solution,

the developer, is a chemical agent that reduces completely those crystals containing a latent image centre, while leaving unchanged all the others.

The developing time is also an important parameter of the development process. It should be long enough for those crystals with a latent image centre to be reduced completely, but not so long that unexposed crystals are developed. Infact, a certain number of crystals will be developed even if they do not contain a development centre. These grains, when developed, constitute what is known as *fog* or background.

Developing product may be divided into two main groups, depending on the source of silver ions for reduction and in practice, most developers are a combination of the two type.

The first group is known as physical developing agents: in these kind of products, silver ions are provided from the solution in the form of a soluble complex; They are deposited on the latent image centre and are reduced to metallic silver. This produces spherical grains, the precise shape of which is affected by pH.

The Chemical developing agents are the second group and are more usually chosen to develop the nuclear emulsion also if the choose between the two type will mainly depend on the grain structure required in the image to analyze. In chemical development, silver ions are provided from the silver halide crystal containing the latent image centre. The action of a chemical developer produces a mass of filaments bearing little resemblance to the original crystal. If silver halide solvents such as sulphite are present in a chemical developer, an opportunity exists for some physical development to occur. In this case, the filaments in the processed plate will be shorter and thicker.

Chemical development, like many other chemical reactions, is dependent on temperature. In general, development occurs more rapidly at higher temperatures - below 10°C development virtually stops. For this reason it is important to keep the processing temperature constant during development, otherwise it will not be possible to assess the correct development time.

Another important parameter in developing the emulsions is the pH, as the

developer maintain a given activity within a narrow pH range. In general the less alkaline the environment is, the less active the developer will be; for this reason, at the end of the development is often recommended an acid stop bath. This stop immediately the process and control precisely the time.

The developers usually used to process nuclear emulsions are combined chemical and physical agents, sulphite and bromide are solvents of silver halide. In complex silver ions become metallic silver that precipitates in the gelatine allowing to obtain the silver grains. This causes physical development of the grains and fog. A successful development happens when the reaction in the grains containing the desired latent image proceed faster than the development of the fog.

The speed of the development often change owing to the presence in the developer of the sulfide. The sulfide is required in the recipe of developer because it tends to prevent oxidation of the developing agent by dissolved oxygen from the air.

The conventional photographic process steps are: presoak, development, stop, fix, wash and dry; others new procedures have been made necessary by the great thickness and concentration of the emulsion, and by the requirements that there be uniformity of development and low distortion. Also the conventional operation are rather deeply modified by these conditions.

The purpose of fixation bath is to remove all the residual silver halide, leaving the metallic silver to form the image. Without fixation silver halide remain in the emulsion becoming slowly brown and degrading the image progressively.

The fixing agent most widely used are sodium or ammonium thiosulphate, which form thiosulphate complexes with the silver halide. Silver thiosulphate is soluble in water and so may be removed from emulsion by washing with water. This is the reason why at the end of fixation process emulsions must be washed very thoroughly. If the washing step is not done correctly, any residual can break down, producing silver sulphite which is brown and can obscure the image.

During fixing and washing emulsion can suffer distortions because at that stage they are soft and fragile; another source of distortions is the drying procedure but these can be much more controllable by the use of alcohol-glycerin baths.

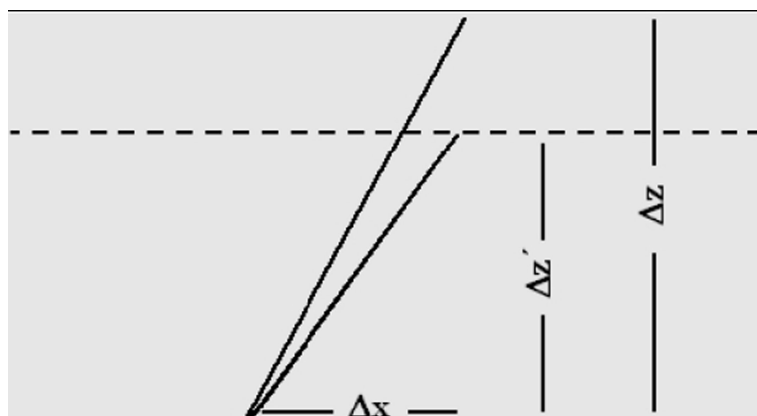


Fig. 3.1: The shrinkage effect: the measured track slope $\Delta z'/\Delta x$ does not coincide with the real slope $\Delta z/\Delta x$. The shrinkage correction is obtained by multiplying the measured slope by the shrinkage factor $\Delta z/\Delta z'$.

3.2.3 distortions and shrinkage factor

In the precise measurements of the emulsions two main effects due to the developing process must be carefully take into account: the *shrinkage* and the *distortion*.

the shrinkage factor occurs as the emulsion thickness before and after the development is different; infact, as we have seen previously, in the developing process some material are added in the volume of the emulsion to replace the silver halide dissolved by the fixer; this process lead to a reduction of thickness of the emulsion layer.

The shrinkage factor is defined as the the ratio between the values of the thickness of the emulsion before and after the development.

This factor is taken into account by the tracking algorithm (because the measured micro track slopes must be multiplied by this factor to obtain the real value). This effect is sketched in Figure 3.1;

Ideally, the processing of an emulsion should lead to a uniform contraction in thickness in the z-direction leaving unchanged the x,y coordinates of any points. In practice, owing to stresses accumulated in the gelatine layer, the position of the recorderd trajectories in the emulsion may suffer shifts on the surface giving

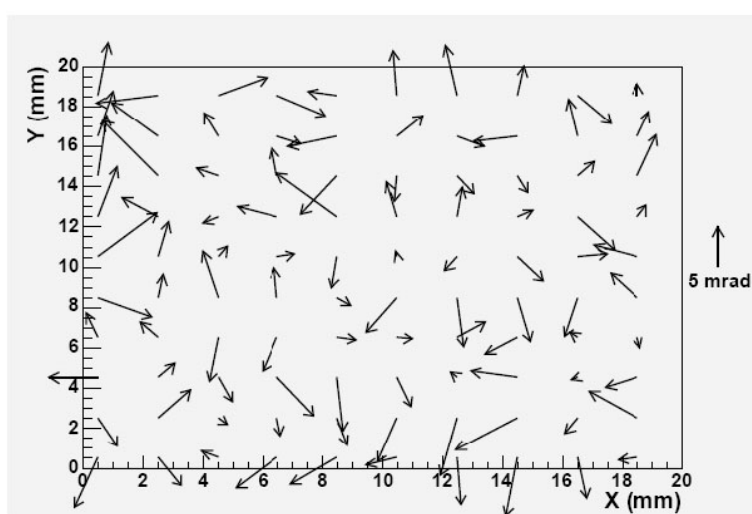


Fig. 3.2: A typical distortion map of an OPERA nuclear emulsion.

distortions.

The simplest form of general distortion is a uniform shear: straight tracks remain rectilinear but their direction and length change by an amount which depends on the magnitude and direction of the shear. A more serious source of error is due to differential shear of the emulsion in which both the magnitude and direction of the shear change with depth. Such distortion changes the tracks of an energetic particle from a line into a curve.

A typical distortion map measured in an OPERA emulsion is shown in Fig. 3.2

The use of double-sided emulsions coated on a plastic support plate, like OPERA films, improves the angular resolution at a level of 2 mrad, because the track direction can be defined by the two points near the support plate, which are practically free of distortions.

3.3 OPERA emulsion films

The OPERA detector will consist of 12 millions of nuclear emulsion films, the largest amount of emulsion ever used in high-energy physics. The emulsions used for the

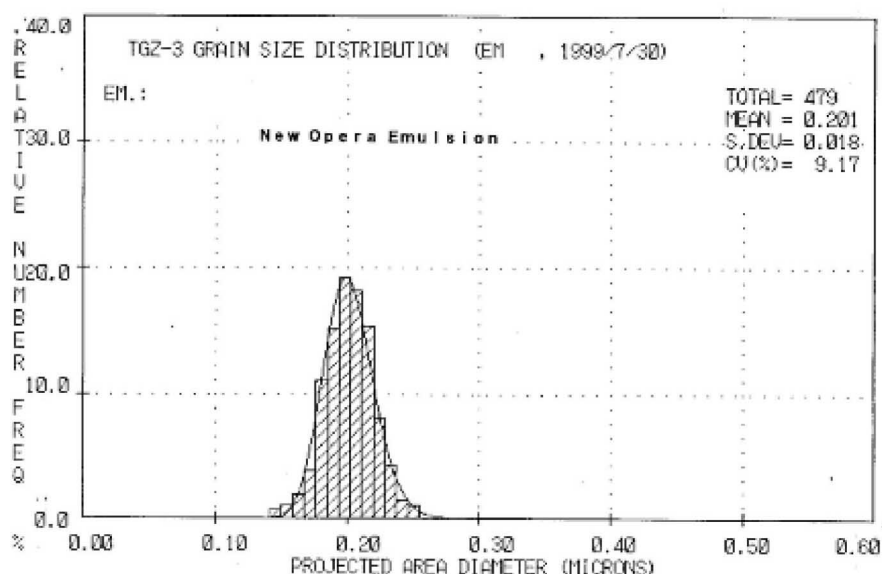


Fig. 3.3: Crystal diameter distribution of the Fuji emulsion layers. The distribution is rather uniform around $0.20 \mu\text{m}$.

past experiments, were poured by hand following standard procedures developed in many years of experience. The same procedure applied to OPERA would be prohibitively time consuming. To solve this problem, an R&D project has been carried out by Nagoya University and the Fuji Film company and after several tests to automatize the coating of emulsions, has been established that the OPERA emulsion film can be produced by commercial photographic film production lines.

Diversely from hand-made films, the thickness can be precisely controlled as in the case of commercial colour films. The measure of the film emulsion layer thickness after development shows a distribution with $\sigma \sim 1.3 \mu\text{m}$.

In addition, the presence of this protective layer allows direct contact with the lead plates, otherwise could happen chemical reactions between the lead plates and the silver halides contained in the emulsion.

During the process of automatic coating some dilution of the gel is required. Under normal conditions, the grain density, defined as the number of grains per

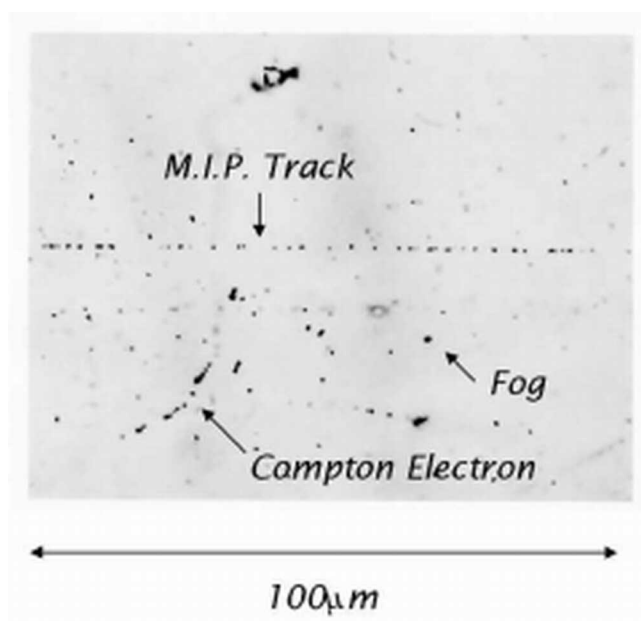


Fig. 3.4: Photograph of a minimum ionising particle (mip) recorded in an emulsion layer. The grain density is defined as the number of grains per $100 \mu\text{m}$ track; the fog density as the number of fog grains per $1000 \mu\text{m}^3$.

$100 \mu\text{m}$ along the particle trajectory, decreases almost linearly with the dilution factor although part of the sensitivity loss may be regained in the development phase. This problem has been solved by increasing the sensitivity of each crystal using the technology of crystal growth developed for standard photographic films.

As shown in Fig. 3.3, the crystal diameter distribution in the emulsion layer is rather uniform around $0.20 \mu\text{m}$. The currently achieved grain density of the machine-coated emulsion films is 30 grains/ $100 \mu\text{m}$ even in the case of a factor of two dilution.

As we have seen in the previous section, the so-called emulsion fog is due to accidentally developed grains randomly distributed in the emulsion volume (Fig. 3.4). In the OPERA emulsions the fog has to be kept at the level of ≤ 5 fog grains / $1000 \mu\text{m}^3$. This can be achieved by applying a moderate development to the emulsion films, still keeping a sufficient sensitivity of ~ 30 grains/ $100 \mu\text{m}$, as shown in Fig. 3.5.

The physics properties of emulsions are the following: density $\rho = 2.40 \text{ g/cm}^3$,

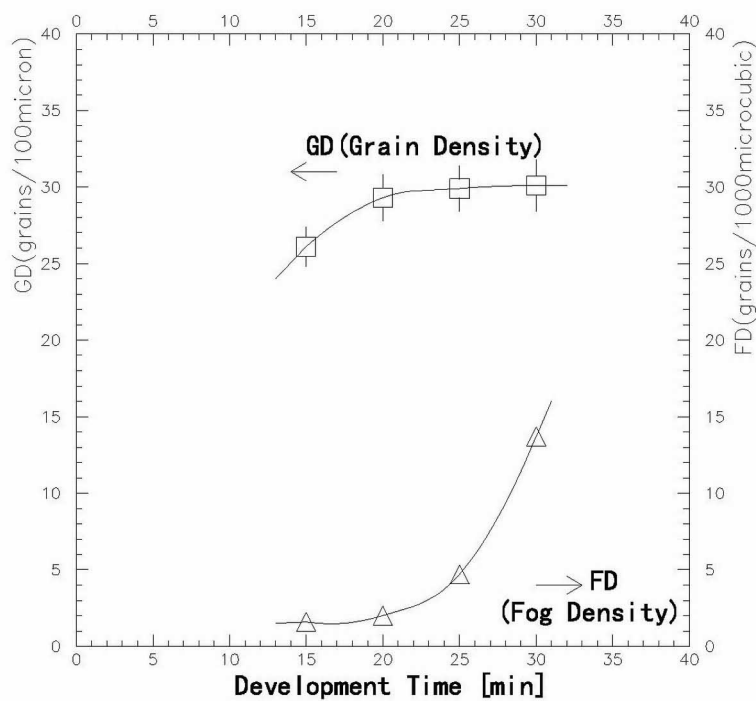


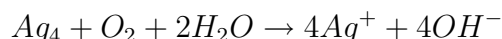
Fig. 3.5: Time dependence of the developed grain density and fog density. Conditions are: amidol developer at 20°C. A development time from 20 to 25 minutes gives satisfactory results.

average atomic number $\langle A \rangle = 18.2$, average atomic charge $\langle Z \rangle = 8.9$, radiation length $X_0 = 5.5$ cm, $(dE/dx)_{mip} = 1.55$ MeV/g/cm² or 37 keV/100 μ m, nuclear collision length $\lambda_T = 33$ cm and nuclear interaction length $\lambda_I = 51$ cm.

3.3.1 Refreshing at Tono mine.

OPERA emulsions are produced in Japan by Fuji Photo Film Company. Due to their continuous sensitivity, the emulsion plates collect latent track images, mainly from cosmic-rays and ambient radioactivity. As we have reported in previous section the

latent image of particle track gradually fades after exposure and this effect, when accelerated, can be used to erase unwanted background tracks. This procedure, which cancels about 96% of the latent tracks, is known as *refreshing*. The refreshing happens by the following oxidation reaction:



Regulating temperature and humidity is possible to control the velocity of the process. The best environment conditions to have a successful refreshing is RH \approx 90-99% and T \approx 20-29°C. A strict monitoring of temperature and humidity must be done during the procedure to avoid the increase of fog and preserve the emulsion sensitivity.

The refreshing is widely known since the beginning of nuclear emulsion research but the large amount of films that will be used in OPERA experiment has requested many efforts and intense R&D in order to guarantee stability, reliability and reproducibility.

Nagoya group has built a refreshing facility at Tono mine [63], designing and producing several refreshing units that work in parallel and they have reached a final speed of 150000 refreshed films/week.

Each refresh unit (Fig. 3.6) is a stainless steel chamber where a water supply on the basement provides humidity; air circulation is realized by a fan and several holes in the stainless walls guarantee a constant circulation speed. In a refresh room there are up to 14 chambers and the temperature is kept constant at 27°C, warm air can circulate through the chambers and humidification is independently tuned in each unit by its own water supplier.

Inside the chamber emulsions lay on plastic holder specifically designed in order to not disturb the air circulation and to avoid the direct contact between them.

The full refreshing cycle has a duration of one week and is realized in three phases:

- Pre-humidification: is the preliminary phase 24 hours long in which the films are stored in the chambers at 27°C and low humidity (\approx 60% RH). The air

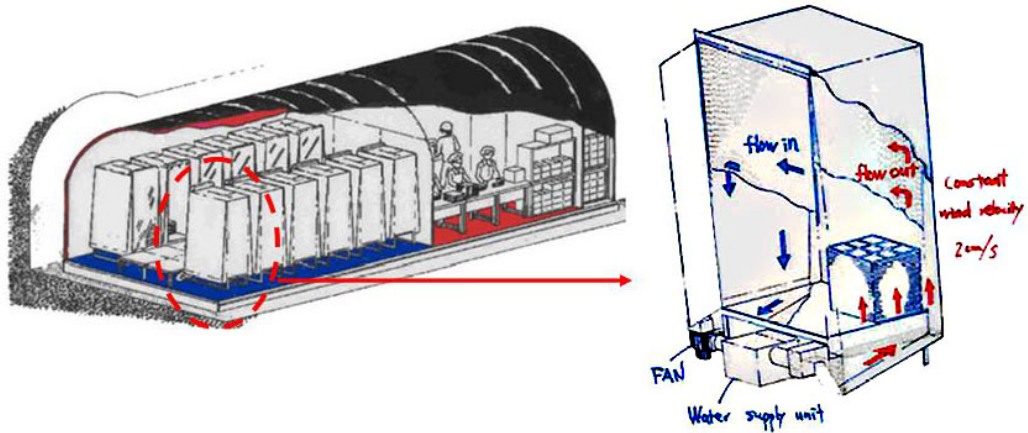


Fig. 3.6: Schetch of Tono mine underground refreshing facility. On the right a drawing of a refresh unit.

circulation is kept very fast and there must be a strong regeneration of air inside the chamber to avoid that a poisoning gas, emitted by emulsions at high temperature, can produce fog increase and sensitivity reduction.

- Refreshing: in this step, that lasts three days, the emulsions are kept at $RH \approx 85-99\%$ and $T \approx 26-29^\circ\text{C}$. In this case the air flows only inside the chamber and there is no air regeneration.
- Drying: after the refreshing films need to be gradually conditioned to 20°C and $50\%RH$ [78]. In this operation, three days long, films remain in the chamber but there is no water supply and there is very quick air circulation and regeneration.

After drying, the films are extracted from the chambers, packed under vacuum in stacks of 9 ECC basic units and stored in underground till the shipment to Europe.

3.4 LNGS development facility

As we have seen in the section 3.2.2 the principal step to develop nuclear emulsions are:

the presoak bath that prepare the emulsion to be penetrated by the developer inside the whole film; the development bath; the stop phase; fixation; washing; the alcohol and glycerine bath is used in order to have a stable thickness and a fast driwell immersion to avoid the occurrence of drops on emulsion surface.

The processing procedure that will be used for OPERA films large scale development has been dicussed with Fuji experts and Japanese collaborators in the last years; a lots of tests has been conducted [78] and the official base-line procedure emerging from these and planned for OPERA films is shown in the following Table 3.1.

Solution	time (min)	Composition	Volume (1 l)
Development	25	Demineralized water	750 ml
		Fuji developer (PDT)	250 ml
		Fuji starter (RD-90S)	20 ml
Stop	10	Acetic Acid (pure)	5 ml
		Demineralized Water	1 l
Clean	10	Demineralized Water	1 l
Fixation	35	Fuji fixer (UR-F1)	500 ml
		Water	500 ml
Wash (4 steps)	4 × 20	Water	500 ml
Glycerine + Driwell	20	Glycerine	200 ml
		Fuji driwell	5 ml
		Water	800 ml

Tab. 3.1: characteristics of bricks exposure.

The OPERA development has some difference respect the standard procedure.

The presoak bath can be avoided because OPERA emulsion is very thin; tests have shown that in the OPERA films there is no difference in grain density (GD) and no depth degradation occur in emulsion developed with or without presoak.

Between stop and fixation a 10 minutes bath in demineralized water has been introduced in order to preserve clean the fixer solution for a longer time; the goal of this bath is to avoid the direct moving of the films holder between stop and fixation tanks. Infact, tests show that, keeping clean the fixing solution, it is possible to obtain much more stability in emulsion quality several months after the development.

The thickner bath for OPERA emulsions has been modified avoiding to use alcool to respect safety regulation, in fact alcool is inflammable at room temperature. The last driwell short immersion has been removed as it has been verified [78] that there is no problem if we mix up it in the glycerine bath.

The specification for LNGS emulsion laboratory are the following:

- 30 liters tanks for developing, stopping and cleaning that can be used for 10 bricks (20 films/l);
- 45 liters tanks for fixation that can be used for 5 bricks (7 films/l);
- 45 liters tanks for washing;
- 30 liters tanks for thickener (glycerin + driwell), that can be used for 10 bricks (20 films/l);

When OPERA will reach its maximum performance, about 50 bricks every day will be identified by electronic detectors, extracted by BMS from the walls; their Changeble Sheets (CS) will be developed underground, scanned by microscopes and if the electronics predicted tracks will be found on the CS the respectively ECC will be brought to the ground and developed. This means that every day 65 bricks (130 CS films in the cavern and 3700 on the surface) must be developed.

To face such a commitment a development facility in the underground lab has been realized and already succesfully tested. For the ground laboratory as the number of films to develop per day is really huge, it has been needed an automatization of the full developing procedure; the procedure has been defined, tested and optimized in order to guarantee large scale quality and stability.

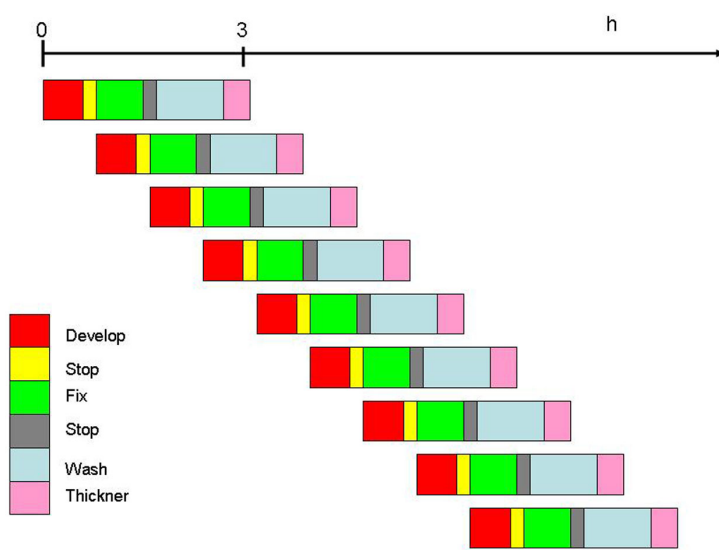


Fig. 3.7: Coceptual development schedule within one chain and one working day.

The duration of one complete process of development, from develop bath till the end of thickner, is 3 hours (see Fig. 3.7) so the first idea to raise the number of brick developable in one day is to start several processes in parallel, by introducing a suitable delay (at least 35', the fixation time being the longer step) between two subsequent developments. A conceptual shedule for full working day is described in Fig. 3.7

The maximun number of processes that can be done in one day is 9. To satisfy these requirements an automatized developing chains has been built; these chains must be activated in parallel and for each one a high level of automation is demanded [65]. In fact automatized developments needs control and overall scheduling of subsequent task such as: on-time displacement of emulsion film holder from one tank to the next, exhaustion of wasted chemicals, insertion of fresh ones when needed, process monitoring and related feedback monitoring. Thanks to the work and experience of University of Rome group 6 chains has been built in the surface lab at LNGS.

Commercial up-to-date technology (UNILINE Roll-On technology) has been adopted for the long belt chains, and high-quality, fully modular elements have



Fig. 3.8: Picture of 3 automatic chains for developing emulsions in the surface lab at LNGS

been selected for the mechanical structure. The arch structure, holding a jaw to pick-up and move the film holders, was designed custom (Fig. 3.8)

Custom made high quality stainless steel tanks and films holder has been adopted; each holder can host 60 emulsion films. A first test development on one automatic chain has been successfully conducted this summer.

The developing automatic chain is hosted in the surface OPERA building where every needs for brick handling and film processing has been studied and realized. Fig. 3.9 shows the plant of the plane with the description of different facilities.

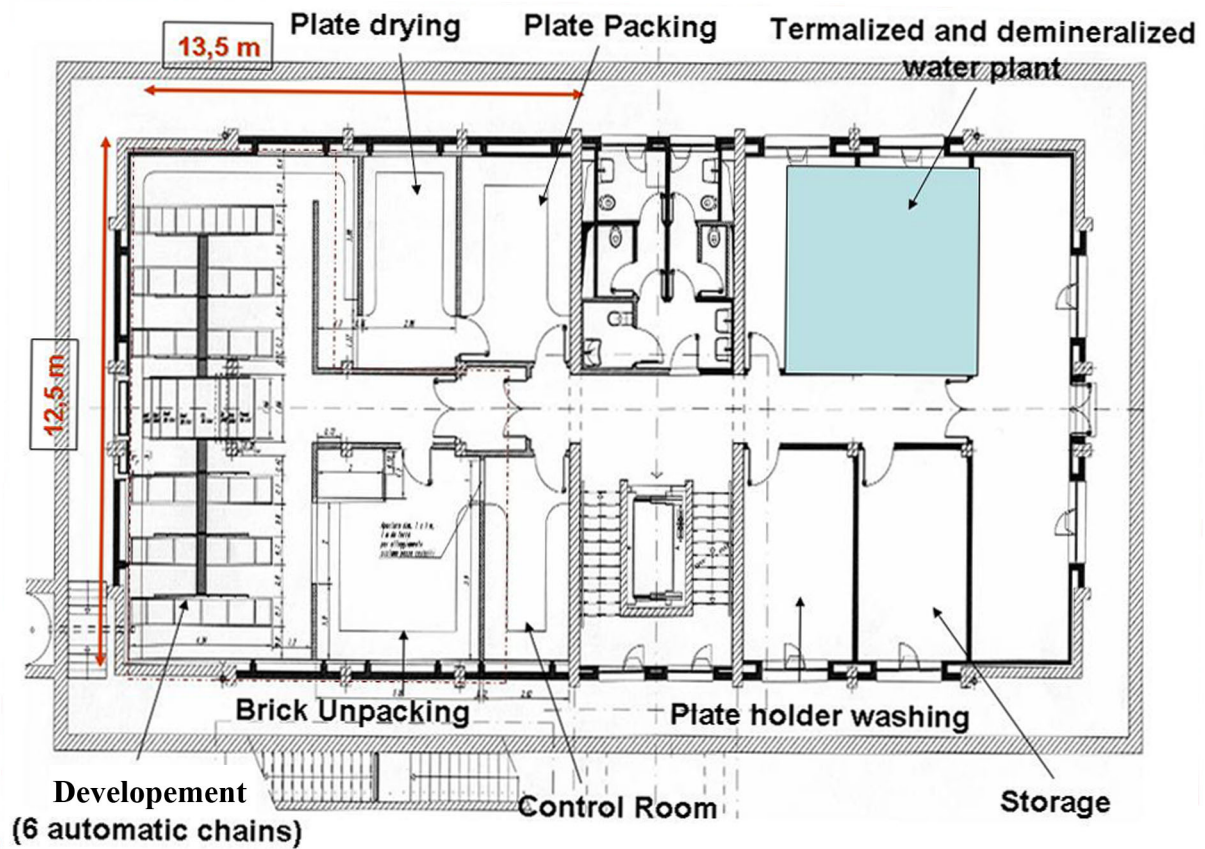


Fig. 3.9: Development floor plant of the OPERA building at LNGS.

Chapter 4

The European Scanning System

4.1 Introduction

The use of photographic emulsions technique in the particle physics has a long history, as we have seen in previous chapter; however, since the beginning, this technique required a lot of time in the eye inspection and analysis of the films.

The tight integration between microscopes and new computer-based technologies has permitted to use this technique also in massive target experiments inconceivable only a few years ago.

The automation of emulsion scanning has been pioneered by the group of Nagoya University (Japan) and the first complete application of an automatic system, called *Track Selector* TS, was used for the DONUT and CHORUS emulsion analysis [66, 67].

The Track Selector scan with a vertical resolution of a few microns; the three dimensional structure of the tracks is reconstructed by raising or lowering the best focus plane of the objective in order to span the whole emulsion thickness.

The basic TS tracking principle was used in its improved version *New Track Selector* and *Ultra Track Selector* taking advantage of the implementation of several image processors working in parallel. The maximum scanning speed is about 2 cm²/h.

The OPERA experiment requires an improvement of about a factor of ten in speed, i.e. a speed of about $20 \text{ cm}^2/h$. To achieve this goal, two different *R&D* programs are carried out.

The Nagoya University group aims to a further improvement of the UTS system (the so-called Super-UTS). The key features of the S-UTS are the high speed camera with 3 kHz frame rate and a piezo-controlled displacement of the objective-lens, synchronized to a continuous stage motion in order to avoid “go-stop” of the microscope stage while taking images. The system uses Fast Programmable Gate Arrays (FPGAs), fast memory and a grabber board connected to the CCD camera (512×512 pixel).

European groups followed a different approach, initiated by the Salerno group with the SySal system for the CHORUS experiment [68]. With this approach, called *multi-track system*, all tracks in each field of view are reconstructed regardless of their slope.

The philosophy of this project is that using the *state-of-art* commercial hardware components, conceived in a modular structure, it is possible to achieve the flexibility needed to upgrade the system following the technological progress.

The Bologna group joined the European Scanning project for the OPERA experiment in all the *R&D* phases and the first prototype was assembled and set-up in 2002 [?] with a scanning speed of about $1 \text{ cm}^2/h$. The last version of the system, upgraded both in hardware and software, has been set-up in 2004 and can reach the required scanning speed of $20 \text{ cm}^2/h$.

4.2 The design of the European Scanning System (ESS)

The main components of the microscope of the ESS are (Fig. 4.1):

- (i) a high quality, rigid and vibration free support table holding the components in a fixed position;

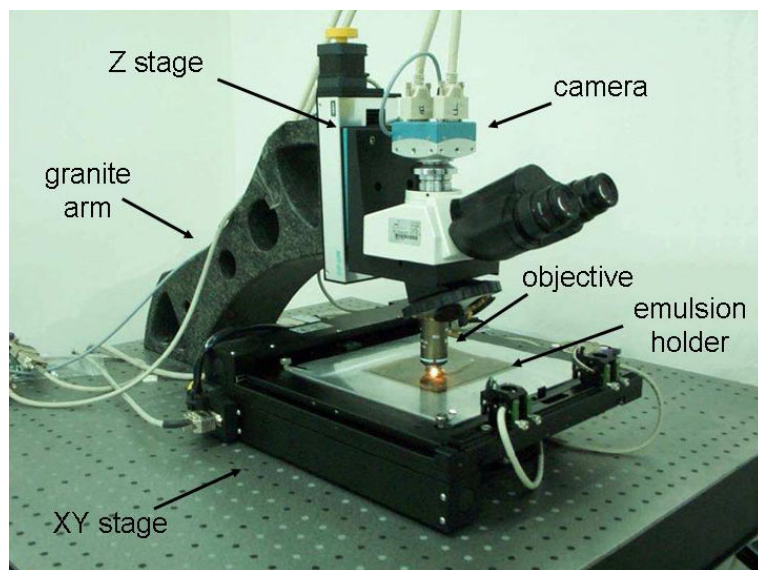


Fig. 4.1: A photograph of one of the European Scanning System

- (ii) a motor driven scanning stage for horizontal (XY) motion;
- (iii) a granite arm which acts as an optical stand;
- (iv) a motor driven stage mounted vertically (Z) on the granite arm for focusing;
- (v) optics;
- (vi) digital camera for image grabbing mounted on the vertical stage and connected with a vision processor;
- (vii) an illumination system located below the scanning table.

The emulsion is hold by a glass plate and his flatness is guaranteed by a vacuum system.

Moving continuously the focal plane of the objective through the $44 \mu\text{m}$ of the emulsion thickness, a sequance of 15 tomographic images of each field of view, taken at equally spaced depth levels, is obtained.

The images acquired are then converted into a grey scale of 256 levels, sent to a vision processor board, hosted in the control workstation, and analyzed to search

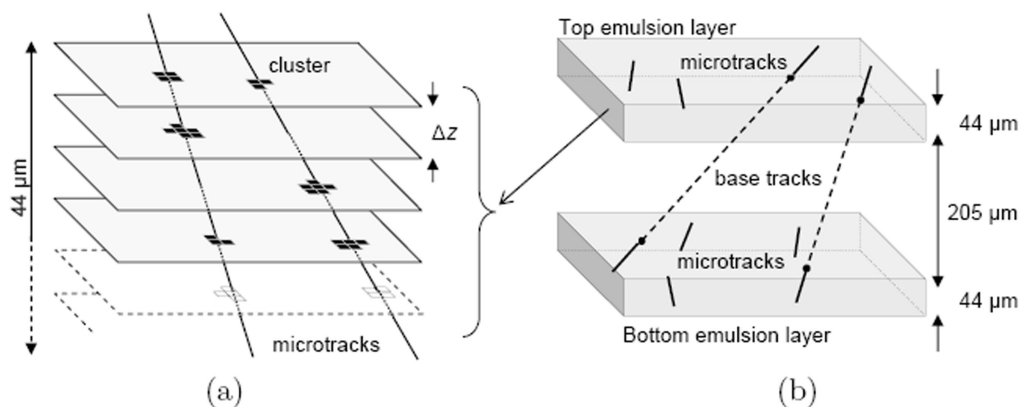


Fig. 4.2: (a) Microtrack reconstruction in one emulsion layer by combining clusters belonging to images at different levels. (b) Microtrack connections across the plastic base to form base tracks.

sequences of aligned grains (clusters of dark pixels of given shape and size). Some of these grains belong to tracks, others, most of them, are accidentally developed single grains (*fog*, see previous chapter).

A *microtrack* is defined as a three-dimensional sequence of grains, on a single emulsion layer, which is reconstructed by combining clusters belonging to images at different levels and searching for geometrical alignments (Fig. 4.2a).

Microtracks belonging to top and bottom emulsion layer are then connected across the plastic base to form the *base-tracks* (Fig. 4.2b). Track position and slope is determined by a linear fit to these clusters, [69].

The ESS has been designed following the specifications of:

- high speed computer controlled precision mechanics for both horizontal and vertical stages with submicron accuracy in order to move from one field of view to the next in less than 0.1 s;
- standard optical system but customized to the observation of a double sided emulsion with a total thickness of $\sim 300 \mu\text{m}$.
- high-resolution camera interfaced with a high-speed frame grabber and a vi-

sion processor able to grab and process images at rates > 350 frames per second (fps).

4.2.1 Mechanical stages

Horizontal stage. The scanning table and the vertical stage have been developed in collaboration with the Micos company ¹ by modifying commercial products; they are equipped with stepping motors Vexta NanoStep RFK Series 5-Phase Microstepping System produced by the Oriental Motor company ². The motors are driven by a 4-axis FlexMotion PCI-7344 board provided by National Instruments ³ and inserted into the host PC.

The ESS uses a Micos MS-8 scanning table with 20.5 cm range in both directions. The coordinates are read out by two linear encoders with a resolution of 0.1 μm . External optical limit switches are mounted on each axis and manually set.

The motion of the horizontal stage (maximum speed, acceleration, deceleration, ...) was set in order to minimize the time needed to move from one field of view to the next (typically $\sim 350 \mu\text{m}$).

Vertical stage. The vertical stage used by the ESS is the Micos LS-110 model. It is equipped with a linear encoder (resolution 0.05 m) and limit switches. During data taking, the vertical stage moves at constant speed calculated by taking into account the camera frame rate, the number of desired frames and the emulsion thickness (44 μm). With a frame rate of about 400 frames/s and 15 levels per emulsion layer, each image is acquired at a vertical distance of about 3 μm ; the resulting speed is about 1150 m/s; the time needed to scan an emulsion layer is about 55 ms (including the time for acceleration, deceleration and synchronization with the host).

¹Micos Gmbh, Freiburger Strae 30, 79427 Eschbach (Germany).

²Oriental Motor Co. Ltd., 6-16-17 Ueno, Taito-ku, Tokyo (Japan).

³National Instruments Corporation, 11500 N MoPac Expwy, Austin, TX (USA).

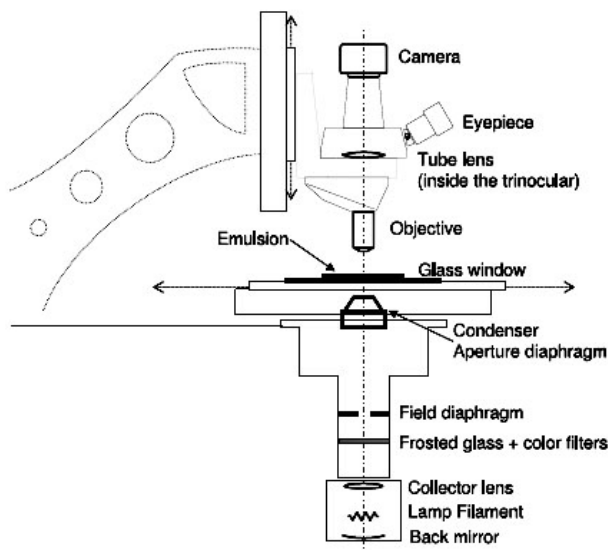


Fig. 4.3: Schematic layout of the ESS microscope optical system.

4.2.2 Optical system

The main component of the optical system adopted by ESS is composed of an objective, a lighting system, a condenser with aperture diaphragm, a glass window that hold the emulsion, a tube lens and a digital camera (Fig. 4.3).

Objective. We recall that the parameters that characterize an objective are: the numerical aperture (NA) that defines the ultimate image resolution (the minimal distance between two points seen as separate), the working distance (WD) and the magnification (M).

The requirements for an objective that must read an OPERA emulsion are $NA > 0.8$ since it is needed a submicron resolution, a $WD > 0.3$ mm (given the overall thickness of emulsion layers and plastic support) and a magnification that depends on the image sensor size; for a 20 mm wide megapixel sensors an objective with $M > 40$ is useful to cope the requirements of few pixels per micron and a large field of view to not reduce the microscope speed.

During the scanning of the bottom layer of the emulsion, the whole plastic base

and the top emulsion layer lay between the objective front lens and the focal plane, for a total thickness of 0.3 mm, while for the scanning of the top emulsion layer there is no intermediate medium. This variation of the thickness of intermediate medium has the effect to overcorrect or undercorrect the spherical aberration [70]. This effect is well corrected by using immersion oil objective, in fact oil, emulsion and plastic base have almost the same refractive index (~ 1.5) and the optical path is almost homogeneous.

After various tests the choice of ESS was the Nikon CFI Plan Achromat 50x oil, N.A. = 0.9, W.D. = 0.4 mm used in infinity-corrected system with a tube lens housed in its trinocular tube.

It is worth mentioning that for the OPERA experiment, where a very large number of emulsion films has to be scanned daily, the oil immersion objective is not the best practical choice. For this reason, an R&D activity on dry objectives is still in progress.

The illumination system. A transmitted illumination system is placed below the scanning table. It was developed jointly with Nikon-Italy; it was designed to obtain the Koehler illumination [70].

The light comes from a tungsten halogen lamp with a computer controlled power supply. The image of the lamp filament is focused by a lens (collector) on the aperture diaphragm of a condenser which concentrates the light into a cone that illuminates the emulsion sheet. A second diaphragm (field diaphragm) is adjusted to prevent emulsion illumination (and also heating) outside the field of view. The condenser numerical aperture should match that of the objective in order to have a wide illumination cone and an optimal optical resolution. The emulsion holder, described in the next section, requires that the condenser working distance is at least few mm.

The final choice was a Nikon achromatic condenser with NA = 0.8 and W.D. = 4.6 mm. A green filter and a frosted glass diffuser are inserted into the light path to obtain an illumination as uniform as possible over the entire field of view and to maximize the optical resolution.

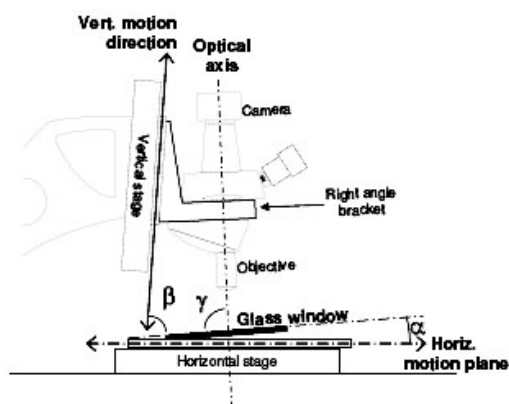


Fig. 4.4: The horizontal and vertical motion directions and the optical axis are aligned with reference to the glass window. The angles α , β and γ are measured using digital comparators and an autocollimator.

The emulsion holder and the alignment. The angular resolution needed for the ESS is few mrad; the systematic error introduced in the angular measurement by non-planarity of the glass window (which holds the emulsion) and by misalignments between the optical components and mechanical stage, has to be kept well below 1 mrad.

The glass window is equipped with a vacuum system to keep the emulsion steady during the scanning, and has a thickness of 4 mm thick. It has a thickness tolerance of less than 10 m per 10 cm length and its deviation from the parallelism is smaller than 1 mrad; the flatness is of a few fringes per inch ($\sim 0.5 \mu\text{m}$ per 1 cm). A 1 mm wide groove in the glass along the emulsion edge is connected to a vacuum pump. The stages and the optical axis are aligned with respect to the glass window (used as a reference plane). The angles between the glass window and the horizontal and vertical motion directions (angles α and β in Fig. 4.4) are adjusted with an accuracy = 0.1 mrad using a digital micrometric comparator. The right angle bracket in Fig. 4.4 is aligned using an autocollimator and the final alignment of the optical axis is ≤ 0.4 mrad (angle in Fig. 4.4). All the optical components shown in Fig. 4.4 are aligned using a centering telescope.

After alignment test have shown that the systematic uncertainty arising from

possible misalignments is 0.5 mrad.

Camera. The goal of 20 cm²/h scanning speed requires a frame acquisition time \leq 4 ms and megapixel resolutions. The ESS is equipped with a Mikrotron MC1310⁴ high-speed megapixel CMOS camera with Full Camera Link interface. Its image sensor is the Micron MT9M413⁵ which delivers up to 10-bit monochrome 1280 × 1024 images at over 500 frames per second. The sensor size is 20 mm (along the diagonal) and its pixels are 12 × 12 μm² large. This choice follows a detailed R&D work with a custom FPGA-driven camera equipped with the same sensor.

4.3 The on-line acquisition software

The online DAQ software for the emulsion automatic scanning and track segments reconstruction was developed using the object-oriented C++ language. It is based on a modular structure where each object carries out a well defined task. Selecting the object and opening the configuration window is possible to insert parameters in order to configure each step of the acquisition process. In Fig. 4.5 the program control panel and the parameter window of the main object are shown.

The list of all modules with their functionality is given in Tab. 4.1.

The scanning output is a collection of raw data files (in binary format) which are saved in Oracle Data Base.

4.3.1 Image acquisition and processing

The frame grabber and the image processor are integrated in the same board, a Matrox Odyssey Xpro⁶, specifically designed to perform onboard image processing.

The on-board processor is a Motorola G4 PowerPC supported by a Matrox custom parallel processor specifically designed to quickly perform local and point-to-

⁴Mikrotron GmbH, Landshuter Str.20-22 D-85716 Unterschleissheim (Germany).

⁵Micron Technology Inc., Boise, Idaho (USA). The sensor was produced before by Photobit Inc, Pasadena, CA (USA).

⁶Matrox Electronic Systems Ltd., 1055 St. Regis Blvd., Dorval, Quebec (Canada).

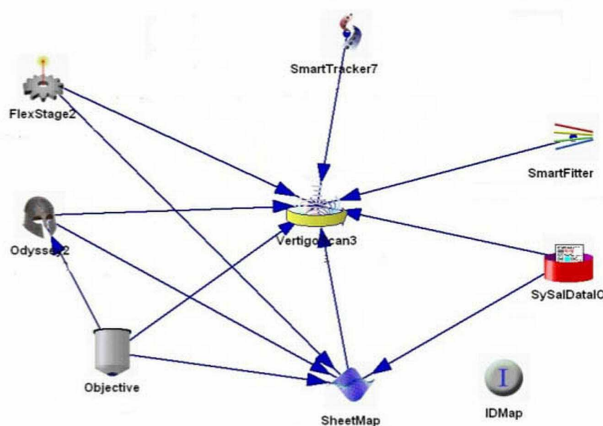


Fig. 4.5: The control panel of the online acquisition system, where the objects are represented.

point operations. It is equipped with a 1 GB DDR SDRAM memory; the internal I/O bandwidth can achieve over 4 GB per second transfer rate, while the external rate reaches 1 GB per second. A Full Camera Link connection allows an acquisition rate from the camera of up to 680 MB/s.

At present, a camera frame rate of 377 fps and 8-bit grey level images are used corresponding to an acquisition rate of 471 MB/s. By acquiring 15 frames per 44 μm emulsion layer, an acquisition time of about 40 ms is needed for each field of view.

Considering a synchronization time of 15 ms, a mean time of ~ 90 ms for the field of view change, a field of view of about $390 \times 310 \mu\text{m}^2$ and a superimposition between contiguous fields of $30 \mu\text{m}$, a scanning speed of about $22 \text{ cm}^2/\text{h}$ is obtained. The effective scanning speed is a bit lower ($\sim 20 \text{ cm}^2/\text{h}$) because sometimes the microscope has to scan the full sheet thickness to find the emulsion surfaces (focusing). For precision measurements [18] or in particular applications, the microscope can be used with other objectives and camera resolutions; the scanning speed changes accordingly.

The selected exposure time is limited by grain size ($\sim 1 \mu\text{m}$) and by vertical resolution ($\sim 3 \mu\text{m}$). Therefore, the exposure time should be smaller than the time

Name of the module	Functionality
Objective	stores the information related to the used objective and performs the pixel to micron conversion
Odyssey	drives the Odyssey board
FlexStage	is interfaced to the stage controllers and set the movements modalities
SmartTracker	is responsible for track pattern recognition, recognizing sequences of geometrically aligned clusters.
SmartFitter	performs the tracks fit.
DataIO	handles data Input/Output.
SheetMap	transforms coordinates and vectors from the current stage reference frame to the emulsion local reference system defined by a grid of fiducial marks printed on the emulsions).
VertigoScan	is the steering module, which uses all the other objects to control the scanning.

Tab. 4.1: List of the modules composing the on-line acquisition software.

needed to span $1 \mu\text{m}$. In our working condition the exposure time is smaller than 0.5 ms (the exposure time depends on the microscope and it ranges between 0.15 and 0.5 ms).

Once grabbed, each image is analyzed using image processing techniques like filters, binarization and clustering (for more details see [69]); the grains are recognized as clusters of black pixels. The number of clusters available for tracking depends on the threshold and on the selection cut in the cluster area.

The distribution of the clusters area in one emulsion layer image is shown in Fig. 4.6a. The cluster area as a function of the distance from the grain center-of-mass is shown in the Fig. 4.6b. The efficiency and the precision in grain finding depend on the cut in the cluster area (a lower area cut yields a lower precision and a higher grain finding efficiency). Taking into account the acquisition speed and the Z level distances ($\sim 3 \text{ mm}$) the cluster area cut is chosen in order to maximize the grain finding efficiency (normally 3 or 4 pixels).

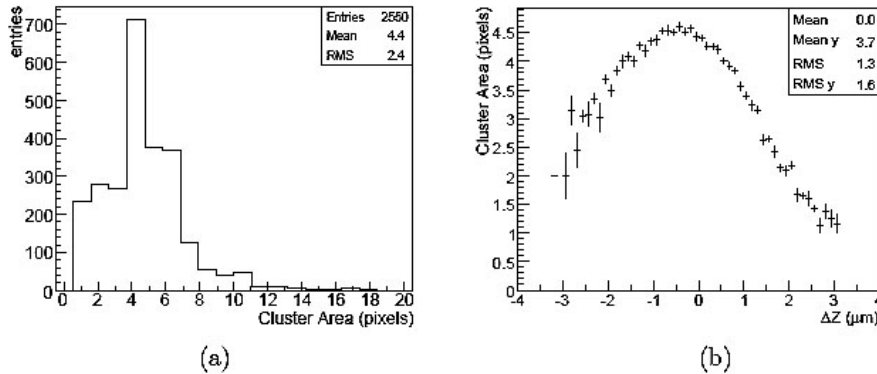


Fig. 4.6: (a) Cluster area distribution in one frame (after the image processing described in [?]). (b) The grain image area versus the vertical distance between the grain center-of-mass and the position where the image is grabbed; notice the asymmetry due to residuals of uncorrected spherical aberration.

4.4 The off-line track processing

The positions and angles of the detected tracks, for each emulsion layer, are recorded as micro-tracks and are connected off-line to form base-tracks, whose positions and angles are not affected by distortion. After collecting these base-tracks in a series of emulsion films, all the films are aligned and track reconstruction (i.e. connecting between films) is performed.

The off-line reconstruction tool used for the following analysis is FEDRA (Framework for Emulsion Data Reconstruction and Analysis), an object-oriented tool based on C++ language developed in Root framework [71].

4.4.1 Base-track reconstruction

After the microscope acquisition we have all the microtracks of the top and of the bottom layer of the emulsion. The next step is to combine in pairs this microtracks in order to obtain the base-tracks. In the reconstruction of a base-track, microtrack pairs are projected across the plastic base and an agreement is searched, within given position and slope tolerances. For each couple of micro-tracks a χ^2 is calculated as

$$\chi^2 = \frac{1}{4} \left[\frac{(\theta_{xt} - \theta_{xB})^2}{\sigma_x} + \frac{(\theta_{xb} - \theta_{xB})^2}{\sigma_x} + \frac{(\theta_{yt} - \theta_{yB})^2}{\sigma_y} + \frac{(\theta_{yb} - \theta_{yB})^2}{\sigma_y} \right] \quad (4.1)$$

where $\theta_{xt(b)}$ and $\theta_{yt(b)}$ are the projections of the top (t) and bottom (b) micro-track angles in the $z-x$ plane and $z-y$ plane, θ_{xB} and θ_{yB} are the same projections for the base-tracks (B) and σ_x and σ_y are the micro-tracks angular resolutions, defined as the angular difference between microtracks and basetracks.

If for one microtrack of the top is found more than one candidate microtrack on the bottom, reconstructing more than one basetrack, then the one with the smaller χ^2 is selected.

4.4.2 Emulsion film alignment

The mechanical accuracy of film piling in brick assembly is about 50-100 μm . Emulsion films are affected by environmental conditions, such as temperature and humidity, which may modify their original geometry; these effects must be taken into account as they could be the source of relative misalignments and deformations. To this extent, by computing a set of similar transformations (shift, rotation and expansion) relating track coordinates in consecutive films, it is possible to define a global reference system (hereafter referred to as *brick* reference system) prior to track reconstruction.

The film alignment is accomplished exposing each brick to a controlled flux of cosmic rays before disassembly, as described by [72], and applying the following procedure film by film.

From a set of independent measurements in single emulsion films, an aligned volume is created through an iterative pattern matching procedure computing the parameters of the transformations

$$\begin{pmatrix} x^{brick} \\ y^{brick} \end{pmatrix} = \begin{pmatrix} a_{11} & a_{12} \\ a_{21} & a_{22} \end{pmatrix} \begin{pmatrix} x^{film} \\ y^{film} \end{pmatrix} + \begin{pmatrix} b_1 \\ b_2 \end{pmatrix} \quad (4.2)$$

where x^{film}, y^{film} , are single film track coordinates and x^{brick}, y^{brick} are the corresponding aligned ones. A least square fit is applied after maximising the number of matching pairs within predefined position and slope tolerances measured in three zones, typically chosen at the corners of the scanned area in order to maximise the lever arm and thus disentangle the contributions due to rotation and translation.

Once all plates are aligned, the track reconstruction algorithm finds and fits all the measured base-tracks of an emulsion film extending in both the directions of the brick. In this way a number of connected base-tracks (not necessarily adjacent) forms a *volume-track*. The connecting base tracks process can be arrested when some inefficiency of tracking algorithm occurs or when a decay or interaction track is found.

4.4.3 Performances of the EES

A test beam exposure with emulsions was performed at CERN in June 2004 to measure the angular resolution and the efficiency. A sample of 64 emulsions sheets was assembled manually to form a brick without lead in order to minimize multiple scattering. The brick was exposed to a 10 GeV/C π^- beam at different angles.

The instrumental background was evaluated at the level of 1 fake base track/ cm^2 analyzing one emulsion not exposed to the beam. The base track efficiency was evaluated after emulsion sheet alignment and the volume tracks were reconstructed. The efficiency, defined as the number of measured passing-through volume tracks measured which hit one sheet with respect to the total number of passing through volume tracks, has been estimated at the level of 90%.

The measured base track angular and position resolutions are shown in Fig 4.7. The angular resolution of a base track is one order of magnitude better than the microtrack resolution (which are spread by emulsion distortion and shrinkage effects).

The scanning speed reached for these measurements is ~ 20 cm²/h per 44 μ m thickness of emulsion layer. About 20 ESS have been installed in European labora-

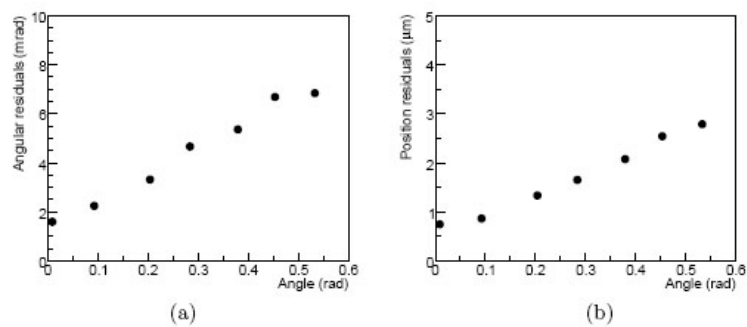


Fig. 4.7: (a) The angular resolution of base tracks as function of the reconstructed angle. (b) The position resolution of base tracks. The errors (that are inside the dimension of each point) are only statistical.

tories involved in the OPERA experiment.

Chapter 5

The experimental test PEANUT

5.1 Introduction

The test-experiment Petit Exposure At NeUtrino beamline (PEANUT) has been performed at Fermilab from August till December 2005. In this test a detector composed by OPERA-like ECCs and electronic detector has been exposed to the NuMI neutrino beam in the MINOS Near Detector (ND) hall at Fermilab. The goal of this test is to validate the OPERA analysis procedures and to study backward particle production in neutrino interactions, which is of interest to the OPERA collaboration as well as to the neutrino community in general.

5.1.1 The NuMI neutrino beam

Neutrinos at Main Injector (NuMI) is a conventional, two horn focused, accelerator neutrino beam intended for short and long baseline neutrino experiment. The neutrino beam provide an intense, high-energy (2-20 GeV) flux of muon-neutrinos, with low contamination of electron-neutrinos.

NuMI is designed to use the 120 GeV/c proton beam provided by the Fermilab Main Injector at an average power of 400 kW. The primary beamline bends the particles downward to achieve a 58 mrad vertical angle that directs the beam toward the Soudan mine, in northern Minnesota, as shown in Fig 5.1. The primary proton

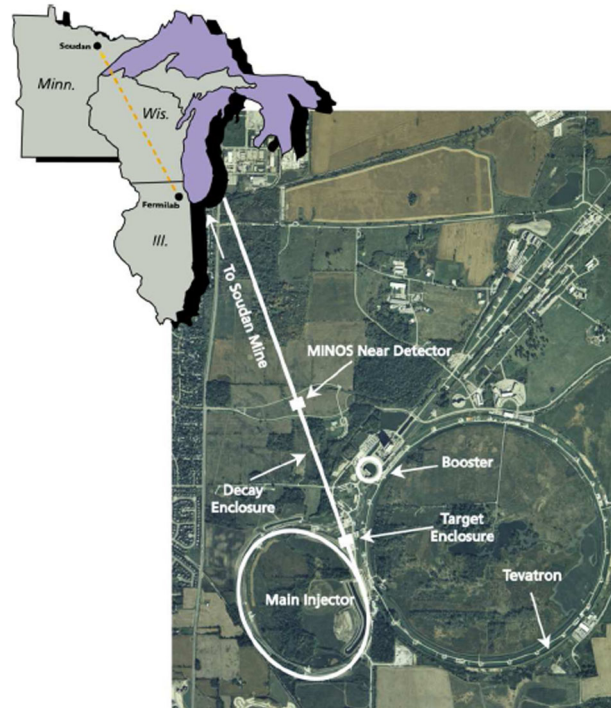


Fig. 5.1: Maps of the Upper Midwest and Fermilab, with the NuMI beam superimposed.

beamline includes instrumentation to measure the intensity, trajectory, and size of the proton beam.

The NuMI beamline converts the intense proton beam into a focused neutrino beam; the major components are illustrated in Fig. 5.2.

The protons are stirred into a solid carbon target to produce mesons through hadronic interactions. The production of mesons from the target is not directly measured in the experiment, but is estimated through the use of standard Monte Carlo codes. This estimation uses input from separate particle production experiments (among others [73, 74, 75]). The most relevant mesons for the production of neutrino beams are pions (π^+ , π^-) and kaons (K^+ , K^- , K^0); those mesons are produced in the greatest numbers and are likely to decay into neutrinos.

After production, the charged mesons are focused by a pair of pulsed, toroidal

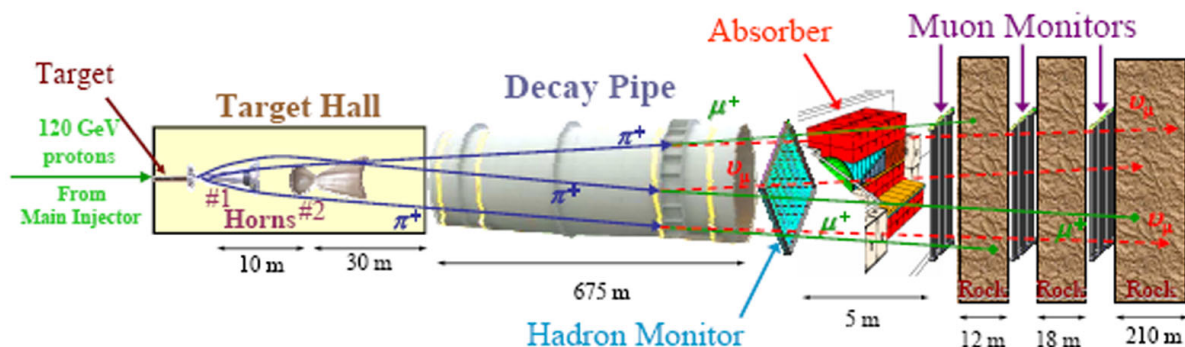


Fig. 5.2: Illustration of the major NuMI beam components.

magnets called horns. A horn is a coaxial, transmission-line magnet with an air gap between the conductors. The inner conductors of the NuMI horns have parabolic profiles, such that they allow momentum selection of the pions through focusing.

Subsequent to the horns is 675 m long vacuum pipe in which forward-focused mesons are conducted (decay pipe). In the pipe, mesons decay into muon and muon neutrino pairs, establishing the neutrino beam.

The Hadron Monitor Detector rests at the end of the decay pipe and measures the remnant beam of uninteract protons and non-decayed mesons;

Immediately following the Hadron Monitor is the Adron Adsorber, a mass of steel, concrete and alluminium that stops the hadrons. Muons penetrate the adsorber and continue into unexcavated rock, where they range out over a distance proportional to their energy (≈ 170 m). Before the start of the rock, and in two excavations into the rock, Muon Monitor detectors are installed to measure the spatial distributions of three energy ranges of the muon beam.

Variable Energy Beam

The NuMI target and horns system is designed to allow production of different energy neutrino beams with the same energy of incident protons. This different energy

beams can be used to explore different ranges of neutrino oscillation parameters.

There have been studied two modes of reconfiguration that allow to vary the beam energy: movement of both horns and target [76] to best focus high energy pions, and movement of only the target upstream of the horn system [77].

The first mode, considered in the design stage, requires several weeks for reconfiguration and recommissioning. Three configuration of target and horn spacings were defined as the low-energy (LE), medium-Energy (ME), and high-energy (HE) beams (Fig.(5.3). The higher-energy beams generally produced a greater number of total neutrino interactions as the cross section is higher.

During the PEANUT exposure the NuMI beam has been provided in LE configuration.

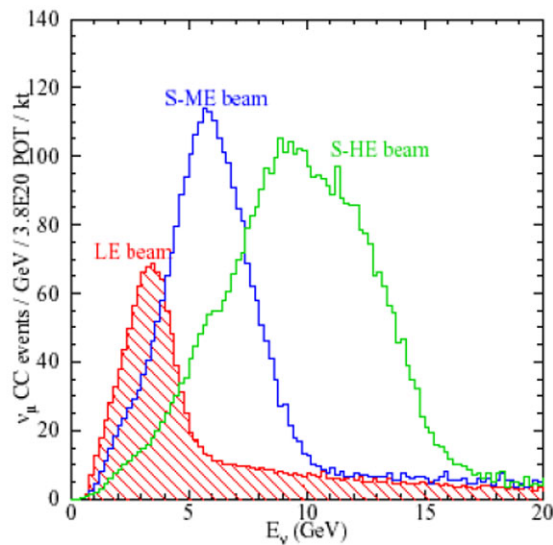


Fig. 5.3: The three configuration available with the NuMI beam. The Low Energy (LE) configuration has been used for the test exposure PEANUT:

The second mode of energy variation involves moving only the target to a different position upstream of the horns (Fig. 5.4)

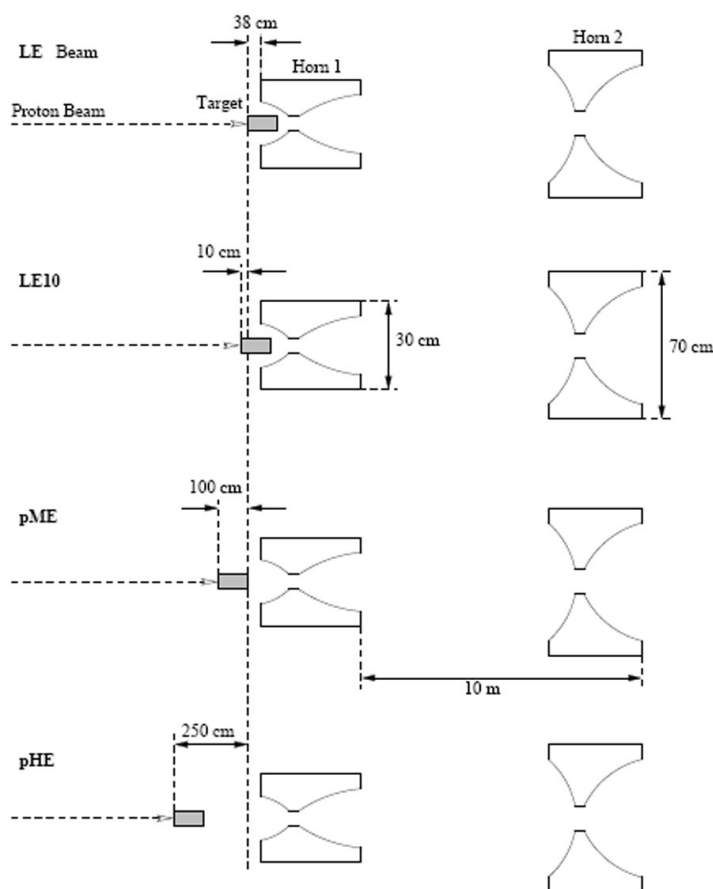


Fig. 5.4: Four potential configurations for the target and horns to produce different neutrino beams. In the LE beam, the target sits substantially inside of the inner conductor of the first horn. The other beams are produced by moving the target upstream of the horns, increasing the average energy of well focused pions.

5.1.2 The PEANUT detector

Very close to MINOS near detector has been installed the Peanut detector. (Fig. 5.5)

The PEANUT detector is composed of an aluminium structure in which is hosted matrices of 4 x 3 bricks interleaved with Scintillating Fiber Tracker (SFT). The bricks were filling in a structure called *miniwall* (see Fig. 5.6).

The total number of miniwalls is four, and after each miniwall a two couples of



Fig. 5.5: Picture Peanut test experiment. Behind Peanut structure is well recognizable the MINOS near detector.



Fig. 5.6: Side view of PEANUT structure. It is well recognizable the 4 miniwall interspaced with SFT.

SFT planes are installed. Each couple of planes, which are mounted perpendicular one another, take the coordinate (X,Y) of the hits. After the second miniwall a further fiber planes, 45 degree inclined, is installed, the U plane, and another 45 degree inclined planes put after the last miniwall, the V plane (5.7).

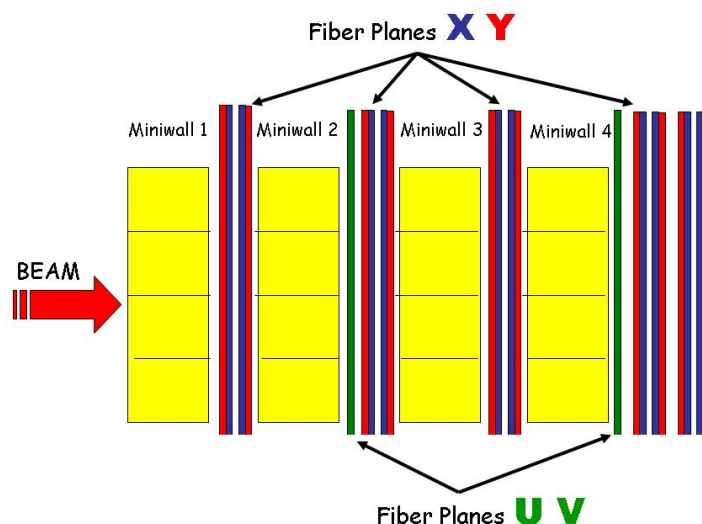


Fig. 5.7: Top side schema of PEANUT setup. The four miniwall interspaced with the SFT planes.

OPERA-like ECC

The ECC bricks used in PEANUT are composed by films produced by Fuji for OPERA experiment, and refreshed at Tono mine, in Japan, and lead plates produced by Gosslar, Germany.

The films, that have been shipped by airplane from Japan, has traveled in boxes. Each box contains three vacuum packed small boxes, each one containing emulsions to built 3 bricks.

Tracks, due to cosmic rays, accumulated during the fly, are present on the emulsions used for the test. In order to flag this tracks, during the construction of the

bricks, the emulsions have been piled in a way that is opposite respect the one in which they have travelled, without flipping the sheet (fig. 5.8).

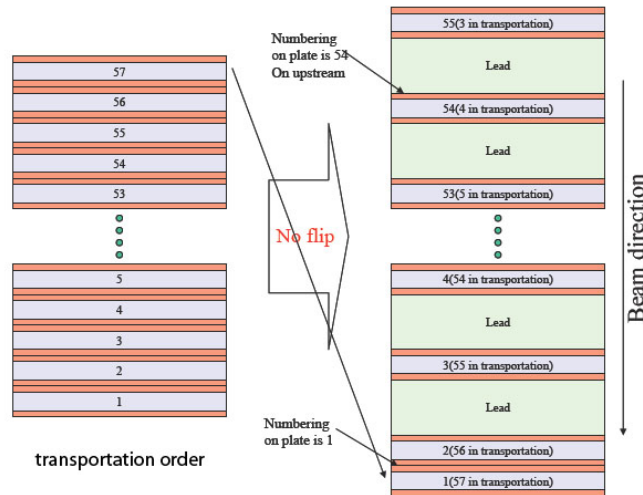


Fig. 5.8: Drawing of the piling mode used to assembly the bricks with the manual BAM

The assembly of the bricks has been done by a manual version of Brick Assembly Machine (BAM), built in Italy (fig.C).

An aluminium "spider" and a plastic box are placed together on the retractable BAM's base; the plastic box is disassembled in a way that the walls are connected to the basis but do not close the box.

Emulsion sheets and lead plates are then placed on the plastic base of the box with an alternate pattern, i.e. one emulsion plate after one lead plate, until having 57 emulsion plates and 56 lead plates. An exception is done for the first two plates, which are allowed be in contact as they act as changeble sheets.

As each sheet and plate is inserted in the pile, the operator checks their alignment by a special removable corner of the BAM, called reference corner. When the piling process is complete, the reference corner is removed and an idraulic piston pushes the pile down in the machine.

As the BAM's base retracts, the walls of the box are pushed so as to close the



Fig. 5.9: Picture of the manual BAM used to assembly PEANUT bricks.

box horizontally and, together with the spider, wrap the pile in the box. When this operation stops, the brick is mechanically closed and is secured by folding the arms of the spider.

The so obtained brick is then wrapped with alluminium tape, to avoid eventual light leakage, and brought to the MINOS Hall for exposition to the beam.

The Scintillating Fiber Tracker

The Scintillating Fiber Tracker (SFT) provided charged particle tracking downstream of each emulsion miniwall. Using hits in the SFT, tracks could be reconstructed for making predictions of the interaction vertex within the bricks.

The fibers are the same that were used in the DONUT experiment [62].

There were 6×10^4 fibers in the SFT. The fibers were Kuraray SCF78, 500 μm diameter. Light from the fibers was read out at one end, and the other end

was aluminized. The fibers were continuous (one pieces) to readout bundles, which simplify the construction without serious loss of light.

The fibers were arranged in layers, with 1200 fibers per layer. Each layer was coated with reflective TiO_2 loaded paint that also served as a glue. Each plane had an area of $0.56 \text{ m} \times 0.56 \text{ m}$.

In the structure there were globally 22 planes (10 for X, 10 for Y, 1 for U and 1 for V) arranged like in fig. 5.7. The Planes U and V are oriented at 45° respect to the X-Y planes.

The fibers were bundled and stacked to a rectangular geometry for readout by six image intensifier units (IIT). The IITs produced an amplified image of the bundled fibers that was digitized by a CCD camera.

After digitization and discrimination, all bright pixel information were stored on the disk of DAQ PC.

The offline process occurred in these stages:

- clustering of hit pixel in CCD coordinate;
- unpacking into real coordinate (X,Y,Z) from CCD coordinate using fiducial fibers (every 5 fibers can be illuminated by Electro Luminescence);
- track reconstruction.

5.1.3 PEANUT test data flow

During the PEANUT test 160 brick have been constructed by manual BAM. Among this 25 have been assembled with iron plates instead of lead. This bricks compete only the japanese colleague and will be usefull to the MINOS collaboration to understand the interactions of neutrinos with the iron; we recall that MINOS ND is almost completely built with iron.

The rests of the bricks, all containing lead plate, has been exposed to beam, in a well defined position among the miniwalls and for a well known period. Position

and time of exposure can be seen at the PEANUT online logbook at the following web address: <http://flab.phys.nagoya-u.ac.jp/peanut/>.

At the end of the exposition the bricks follow two different manipulations depending if they were delivered to Europe or Japan.

The procedure for plate to plate alignment of the ESS, is to expose to cosmic rays for a well defined period the packed bricks and then to print an intrinsic reference systems on each emulsion film.

A part of the bricks for the european labs were exposed to 12 hours cosmic rays and another part to two hours before dismounting them.

Further, during the bricks dismounting procedure, each film were marked by a prototipe machine developed by Salerno University [78]. The machine marked three corner with one single spot of about 60 μm diameter, and on the remaining corner a binary label indicating the brick Id and number of emulsion inside the brick.

After marking procedure the emulsion films were put on mecanical holder and developed following the standard procedure described in Chapter 3.

After developing process, the bricks are packed and assigned to each laboratory to analyze.

Chapter 6

Search for neutrino interactions

6.1 Introduction

The goal of this analysis is to validate the procedures used by the ESS laboratories to search for vertexes induced by neutrino events. The following sections describe the procedures that will be used in OPERA, and the results obtained applying these procedures on the bricks exposed to the NuMI neutrino beam.

6.2 Brick scanning

In Bologna we have 4 bricks of the PEANUT test experiment: bricks BL034, BL044, BL087 and BL088. Each brick was exposed for a well defined period to NuMI beam and to cosmic rays (see Tab. 6.1 for details).

The position of each brick inside the detector is indicated by a three digit (dec-

Brick Nr	Neutrino Exp (days)	Cosmic Rays Exp (hours)	Position
BL034	17.75	2	142
BL044	20.71	2	233
BL087	28.18	12	231
BL088	28.18	12	232

Tab. 6.1: Exposure times for the bricks assigned to the Bologna group.

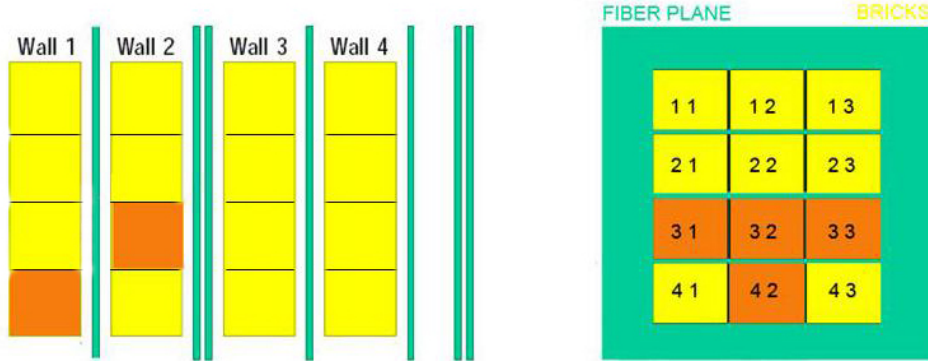


Fig. 6.1: On the left is shown the position in the walls of the bricks. On the right it is shown the position in the matrix of each bricks. The brick BL034 was on the miniwall 1, while the other three bricks were on the third row.

imal) sequence: miniwall, row and the column as shown in Fig 6.1. For example, Brick BL034 has 142 which means that it has been exposed in the first miniwall, 4th row and 2nd column.

Before starting the scanning, a fine tuning of the microscope parameters is required in order to reach a quite uniform microtracks density in each microscope field of view; this is done choosing the image clustering threshold that gives $\sim 350 \mu\text{tracks} / \text{view}$ for the top and bottom layers.

In Bologna lab, for the bricks BL088 and BL087, we have scanned a rectangular area of $10 \times 8 \text{ cm}^2$ for all the 57 emulsions of each brick. The scanning of one plate takes 9 hours at a speed of $\sim 20 \text{ cm}^2/\text{h}/\text{layer}$.

A general scanning with a larger area ($\sim 93 \text{ cm}^2$) is running on brick BL044; in this case the time required for one plate scanning is 12 hours at the same velocity.

On the BL087, we have acquired the first two plates in general scan and a data base driven scan back is running.

After scanning, raw data were processed as described in the Chapter 4; for each sheet we performed the microtrack connection between the top and bottom layer in order to form base tracks. The quality of the obtained base track is evaluated by

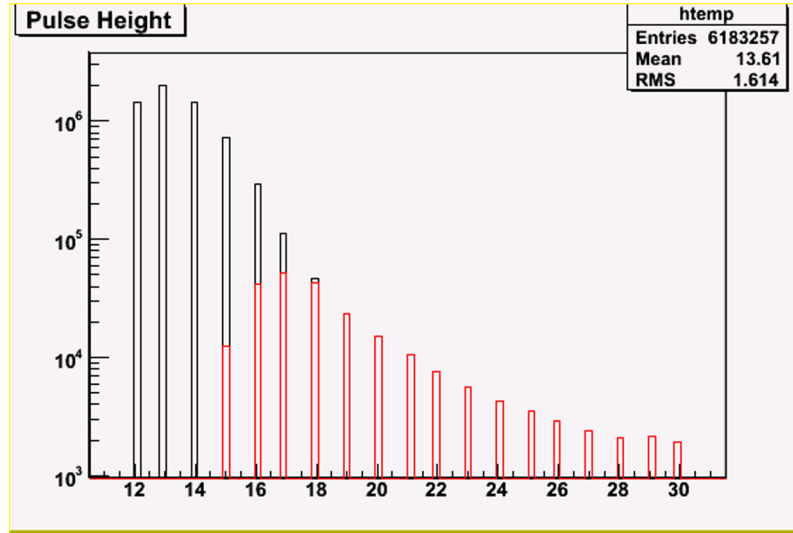


Fig. 6.2: Pulse height distribution for the tracks measured on one single plate. The black line refers to data acquired from microscope. The red line superimposed shows the distribution of the PH after the quality cut, and consequently the signal that we considered for the analysis.

two variables: χ^2 , obtained by the angular difference between microtracks and base track, and *pulse height* (PH) defined as the sum of the clusters that compose the two microtracks. Combining these two variables is possible to define a quality cut to separate the signal from background. The quality cut used for PEANUT brick analysis in Bologna is:

$$\chi^2 < PH * 0.66 - 9 \quad (6.1)$$

The effect of this cut on the distribution of the pulse height is shown in Fig. 6.2,

On the first two films of each brick (doublet) we have performed alignment by coupling the two emulsion sheets considering two different packing order:

- i) Transportation order: alignment in the way of the Japan-Fermilab fly,(Fig. 6.3a).
- ii) Assembly or exposure order: alignment in the way of the brick assembling (see previous chapter). In this case the two emulsion have the z direction reversed respect to the transportation order, without flipping the films,(Fig. 6.3b).

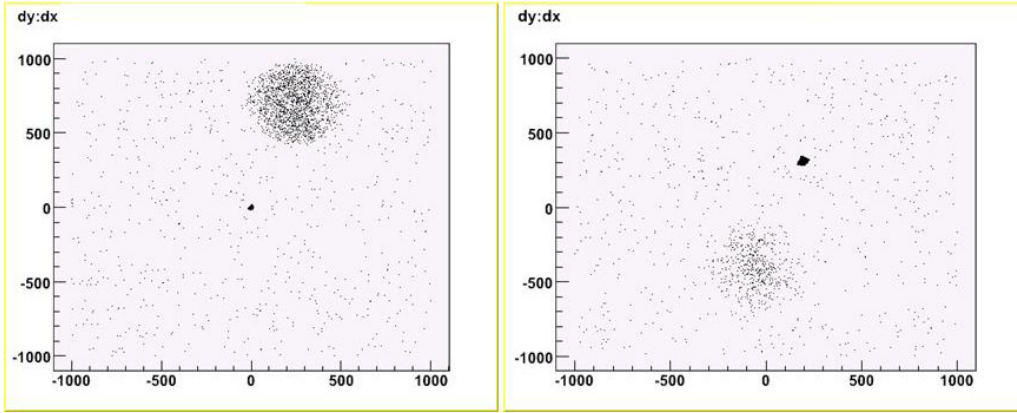


Fig. 6.3: (a):Pattern distribution of doublet in brick assembly order and (b) in transportation order. In (a) the central spot, concentrated in almost one point in the coordinate (0,0) is the pattern of beam and alignment cosmic rays, while the blurred spot is due to the transportation cosmic rays that are not aligned in this direction. The inverse situation hold in (b).

By flagging the tracks aligned in the first order is possible to recognize the cosmic rays accumulated during the fly and remove them before performing the alignment and the reconstruction in the direction of the beam and cosmic rays exposure. The shuffling of the films decrease the quality of the transportation alignment and raise the probability of not to reconstruct the tracks of cosmic rays recorded during the shipment Japan-Fermilab. This way of operate is called *virtual erasing* of transportation cosmic rays. This technique cannot be applied for the cosmic rays entered ortogonally to the films which cannot be erased.

The base-track density, in assembly and transportation order are given in the following table 6.2

The differences in the densities are expected becouse during the fly the emulsions were exposed to cosmic rays at higher quota and for a time longer than the exposure for alignment performed on ground surface at Fermilab.

After the doublets alignment, for the bricks BL088 and BL034, all the remaining films were aligned in the exposition and transportation order. In the exposure order,

Brick Nr	Assembly order (b-tracks/ mm^2)	Transportation Ord. (b-tracks/ mm^2)
BL034	0.4	2.3
BL044	0.5	3,7
BL087	0.6	1.8
BL088	0.8	2.7

Tab. 6.2: Base track density in assembly and transportation order.

in aligning from the 3rd plate till the end, also the presence of the lead plate is taken into account by introducing the 1 mm thickness of the lead plate in the quota.

For the brick BL088 are reported the distributions plot for the positions (X, Y) and slopes (TX, TY) of the base tracks reconstructed in the transportation order in Fig. 6.4 and beam order Fig. 6.5.

From the slopes distributions is easily recognisable the typical cosmic rays shape in the transportation order, while the beam profile is visible in slopes distributions in the exposure order. Considering the slopes distribution of Fig. 6.5 is visible a shift from the center of about 20 mrad in X projection and about -50 mrad in Y. This shifts could be explained with a misalignment between the brick and the beam of about 2 mm and is compatible with the precision of the manual brick insertion in the wall.

The tracking efficiency in the beam and cosmic direction are respectively of 72% and 88%. This efficiency, below the 90% standard efficiency, can be explained owing to the big amount of background that the films have accumulated and to local distortions (till under study) generated in the phase of closing the brick with a hammer in the manual brick assembly operation. The differences between the efficiency in transportation and beam direction can be explained with the difference in the ionizing power of the particles of the cosmic rays and on the beam. In fact, as can be evaluated comparing the (a) side of Fig. 6.6a and Fig. 6.7a, the beam tracks are almost all minimum ionizing particle, with a typical mean value in grains number of 20, while selecting the more penetrating tracks of cosmic rays this mean value rise to 24.

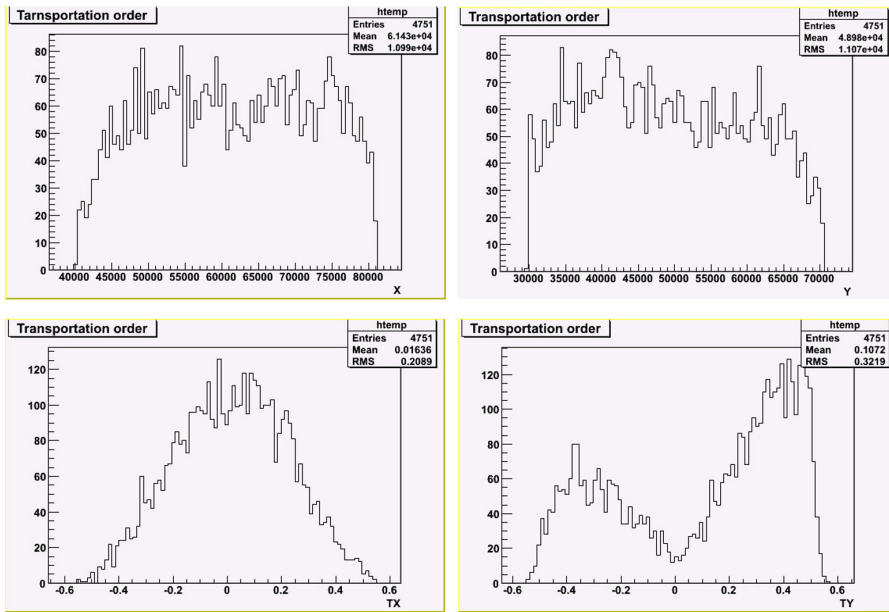


Fig. 6.4: Positions and slopes distribution for the base tracks reconstructed in transportation order.

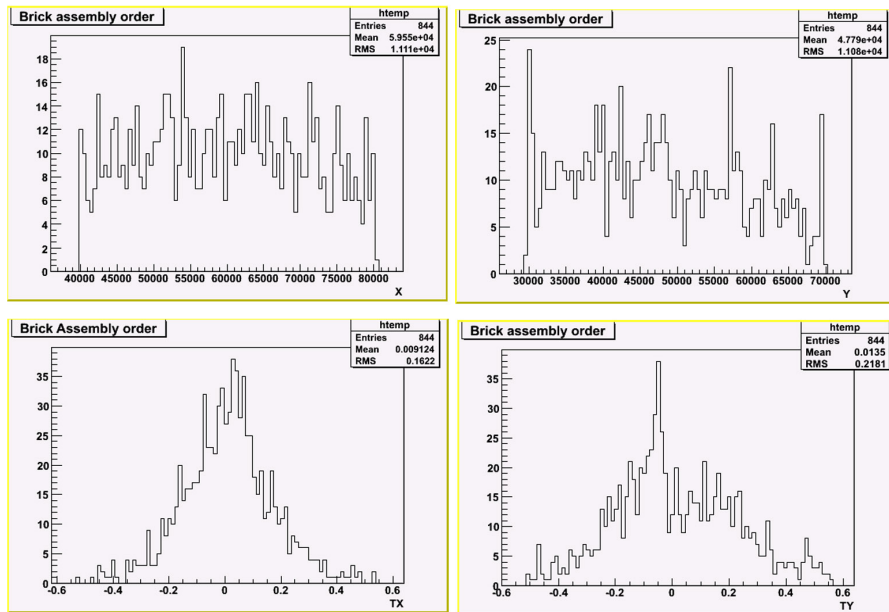


Fig. 6.5: Positions and slopes distribution for the base tracks reconstructed in exposure order.

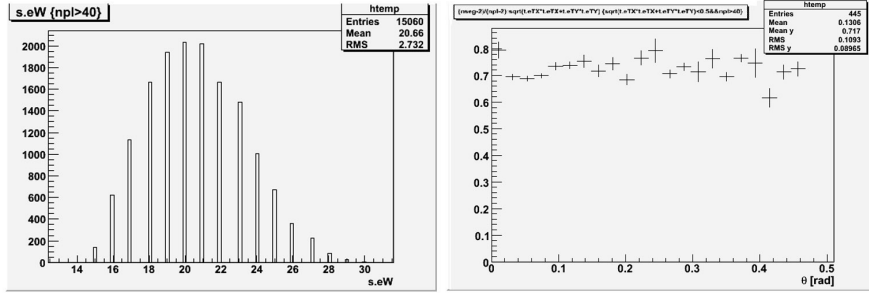


Fig. 6.6: Grain number distribution (a) and tracking efficiency (b) for the reconstructed base tracks in the beam direction

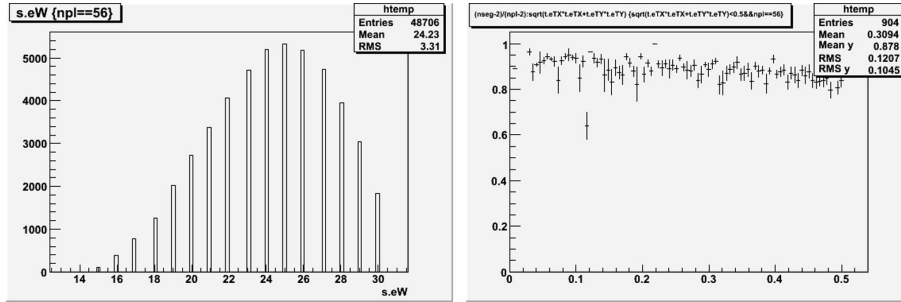


Fig. 6.7: Grain number distribution (a) and tracking efficiency (b) for the reconstructed base tracks in the transportation direction

As previously explained we scanned the first two plates in each brick. We remind that no lead plate was inserted in between them, in order to neglect the multiple scattering contribution and better define the “trigger” direction given by the first two base-tracks.

This direction was computed by aligning the two plates, with the procedure explained in chapter four, and matching the base-tracks according to predefined angular and position tolerances.

The plate to plate alignment precision obtained in brick BL088 is reported in Fig. 6.8.

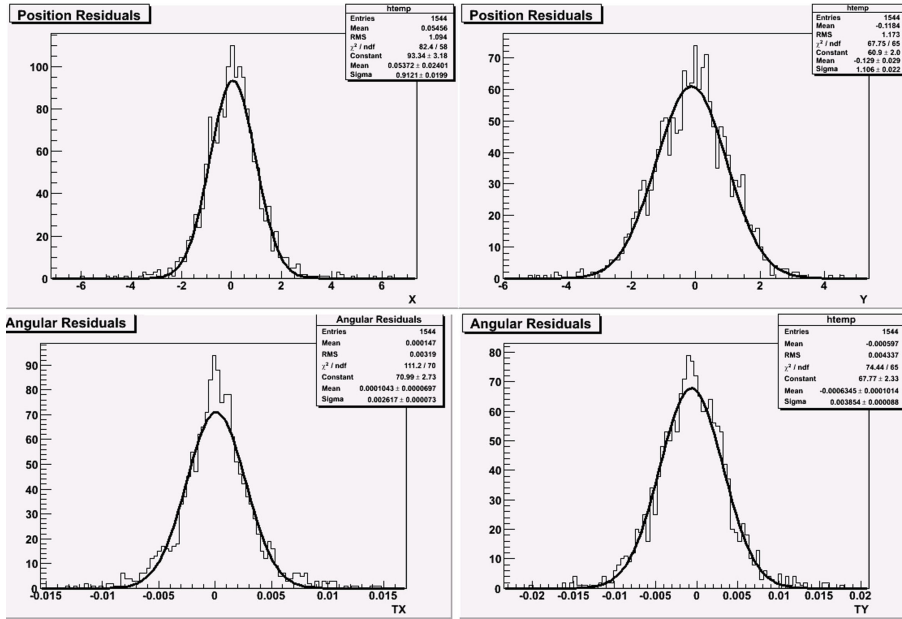


Fig. 6.8: Position and angular residuals after plate to plate alignment of doublet of BL088.

6.3 Electronic detector predictions

The information about the SFT are stored in ascii files. Each file refers to a single run and reports the event number, hits, projection track and 3D track.

From the online logbook we get the duration of the exposure and the geometric position of the brick inside the walls. To pick up passing through tracks we required 7 hits over 20, regardless of the wall position. Stopping track candidates were considered those tracks with 9 hits for walls 1, 7 hits for wall 2, 5 hits for wall 3 and 5 hits for waal 4, with the requirement that no hit is upstream. Following this criteria we extract good candidate tracks to be searched for in ECCs.

The number of SFT predictions extracted for the four bricks are reported in table 6.4. For each brick the electronic predictions are converted in the same data file structure of a base track to handling predicted tracks with the same tools of those recorded on an emulsion film.

6.4 Brick / SFT Alignment

The final step is to match the SFT predictions with the directions and positions of the doublets reconstructed in the first two plates. The matching is defined when SFT and doublets directions and positions are within 10 mrad and 1200 μm respectively;

In Fig. 6.9 the residuals of SFT/doublet matching are shown for BL088.

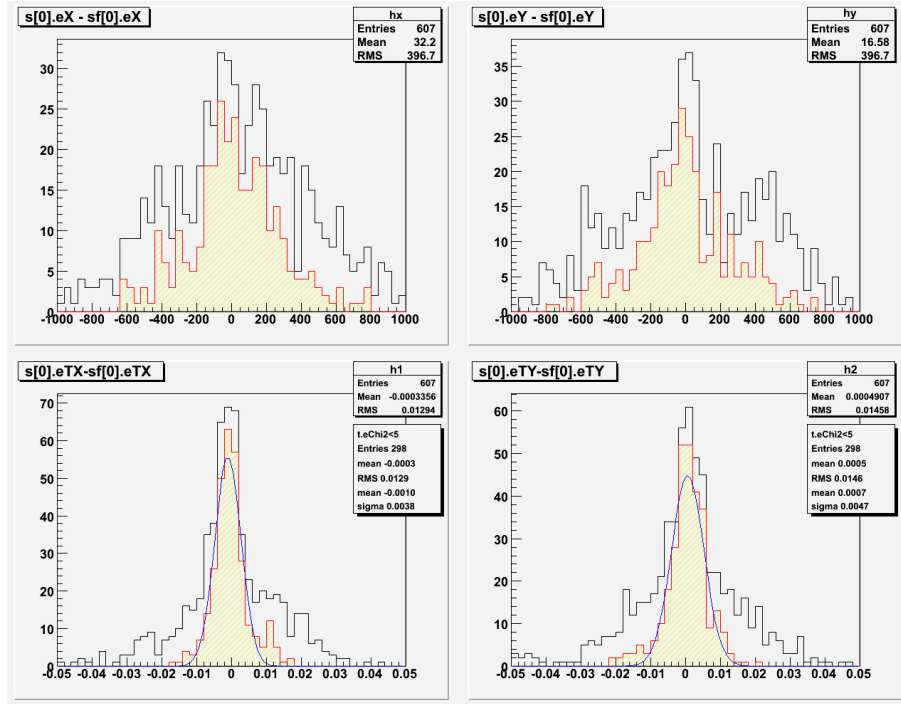


Fig. 6.9: Position and angular accuracy alignment between the electronic predictions and the doublet of the brick BL088.

Tab. 6.3 reports the sigma of the residual distributions for all the bricks.

The following table 6.4 summarizes, for all the analysed bricks, the number of SFT predictions, the number of doublet tracks and the matches occurring between them.

The alignment between SFT predictions with tracks extrapolated from the doublets has been successfully accomplished for all the bricks shared in Bologna scanning Laboratory.

Brick Nr	ΔX μm	ΔY μm	$\Delta\theta_x$ mrad	$\Delta\theta_y$ mrad
BL034	434	458	10	11
BL044	650	547	8	9
BL087	389	378	3	4
BL088	397	397	4	5

Tab. 6.3: Angular e position accuracy between SFT doublets alignment.

Brick Nr	Number of predictions	Number of tracks in doublets	Matches
BL034	1830	2493	276
BL044	2206	2790	213
BL087	2916	8960	543
BL088	2960	8797	607

Tab. 6.4: Number of electronic predictions, tracks in the doublets and their matches.

6.5 Vertex Analysis

After the alignment the goal of the study is to search vertexes produces by neutrino interactions inside the bricks volumes. As the NuMI beam has worked in Low Energy configurations we expect to have in our bricks 97 neutrino induced events.

We have analyzed the number of SFT hits and the χ^2 of the matches for the BL088 doublet and SFT predictions (see Fig 6.10); we decide to consider in our analisis only those prediction that have a number of hits greater than 9 and a χ^2 less than 5 and we obtain a subsample of 326 predictions out of 607 for the brick BL088.

As a first attempt, we tried to visually inspect SFT tracks that matched the ones in BL088. In this way we could classify each track on the basis of its topology. We named these categories as *passing through*, *multi-hits events* and *candidates*:

- Passing through tracks are those having at least one hit in each plane in all the projective views. Typically these events are formed by few tracks (from one up to three) well separated in space and direction.

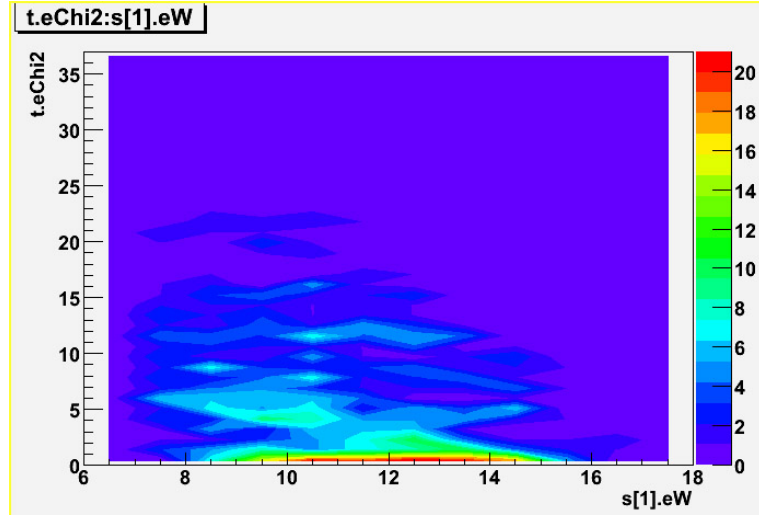


Fig. 6.10: χ^2 vs number of hits for the SFT prediction of BL088.

- Multi-hits events are those events reconstructed with a large number of tracks inside the brick acceptance; typically the number of tracks reconstructed is larger than 5 and it is very difficult to disentangle single tracks among them.
- Candidates or create inside events are tracks which are very likely to be generated by neutrino interactions: they have no hits in the SFT upstream planes but only downstream the brick position (Fig. 6.11).

The result of this classification for the 326 matches of BL088 is: 253 passing through tracks, 45 multi-hits and 28 candidate events.

6.5.1 Prediction scanning

Starting from the 326 tracks of the doublet that have matched with the SFT tracks we have performed the search inside the BL088 brick using the so called *Scan Back* (SB) procedure.

This procedure is completely automatized and relies on a continuous feedback with the data base. Preliminary plate to plate intercalibration is performed acquiring the fiducial grid and three areas in which long and straight selected tracks of

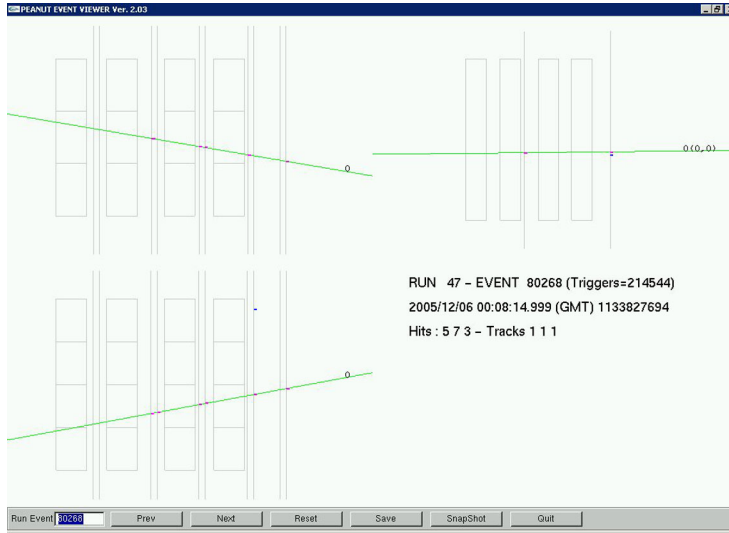


Fig. 6.11: Example of candidate event in the classification with the viewer on the brick BL088. The beam comes from left, the position of the brick is shaded. There are no hits on the first SFT plane before the brick but only on the planes after.

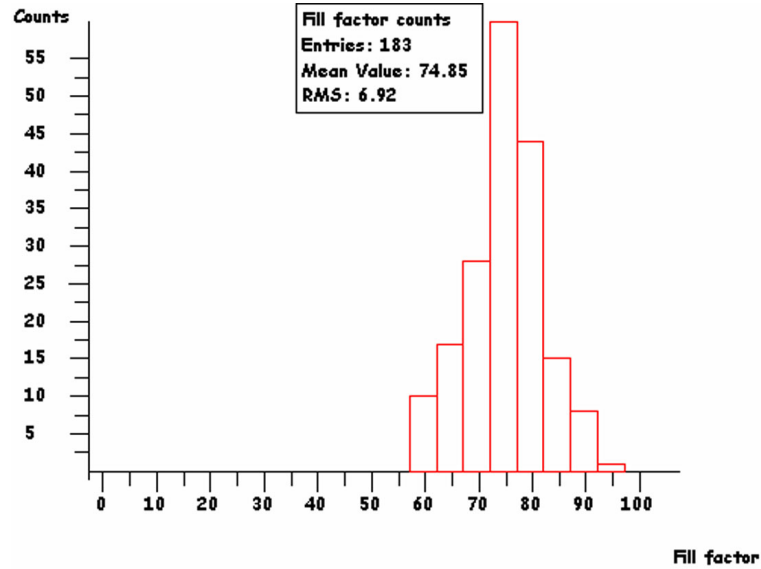
cosmic rays are followed (at least 8 tracks must be found on the plates otherwise the procedure fails). This procedure provides the parameters of the affine transformation that allows to follow selected tracks up to their stopping point.

We store in the DB the parameters of each predictions, X-Y coordinate and TX-TY slopes; intercalibration areas are chosen to be $6 \times 6 \text{ mm}^2$ in order to have enough cosmic ray tracks to follow.

The track parameters, are found on the first plate, with an angular tolerance of 30 mrad and a position tolerance of $70 \mu\text{m}$ for almost vertical tracks; in the general case they are searched with an increasing tolerance according to the formulas:

$$\Delta TX = 0.03 + 0.05 * TX \quad \Delta X = 70 + 6 * TX$$

and similarly for the Y projection. If no track is found in a given plate, the prediction is extrapolated on the following plated and search for in the corresponding area. This procedure is repeated for three consecutive plates. If no track is found in three consecutive plates, we define the track as a *stopping* track and the position of the last measured base-track is defined as the *stopping point*. The SB efficiency,

**Fig. 6.12:** Scan Back efficiency

		SFT viewer			Total
		Pass-through	Multi-hits	candidates	
scan back	pass	147	28	15	190
	stop	106	17	13	136
					326

Tab. 6.5: Scan Back result

computed according to the number of found/expected track segments, is reported in the Fig. 6.12

At the end of this procedures we found 136 stopping points. Table 6.5 shows the results of scan back analysis compared with the SFT viewer classification.

6.5.2 Scanning around *stopping points*

A volume scan around each stopping point is then performed in order to classify the candidate vertexes and to confirm (or disproof) the presence of a neutrino interaction. This procedure is called *Total Scan* (TS).

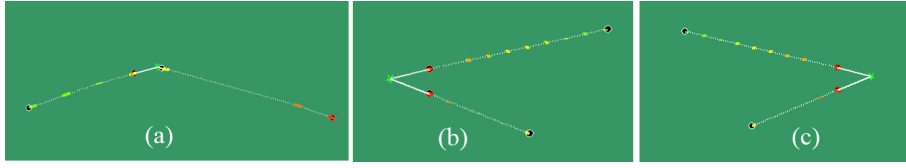


Fig. 6.13: Basic vertex topology, reconstructed by FEDRA.

We choose a volume area of $5 \times 5 \text{ mm}^2$ for 11 plates, i.e. the plate containing the stopping point, five plates before and five plate after. The volume is skewed with primary scan-back track slope, so it is a not-rectangular parallelepiped.

The aim of TS procedure is to filter out events with no sign of possible decay topologies and thus to reduce the number of events to be fully analyzed.

Short decays are those in which the neutrino interaction and the particle decay occur in the same lead plate. The only possibility to recognise those events is to measure the impact point of the daughter direction with respect to vertex determined by the particles created at the primary vertex. If the interaction and decay occur in different plates (*long decays*) then the signature is given by the kink angle formed by the mother and daughter directions.

After the TS, inside all the volumes the base tracks of each plate are aligned and tracked again. The FEDRA vertex procedure considers couple of volume tracks and attach together into a 2 prong vertex. This is done on the whole volume and three basic topology are reconstructed:

- i) vertex with mother track or *charged* vertex, (Fig. 6.13a);
- ii) *neutral forward* vertex(Fig. 6.13a);
- iii) *back-forward* vertex (Fig. 6.13a).

Combining these three categories of vertex, FEDRA is able to reconstruct all the kind of topology. In the our analysis, during the vertex reconstruction we have tag and excluded all the back forward vertexes reconstructed in the volume. This vertex can be included in the background.

		SFT viewer			
		Pass-through	Multitrack	candidates	Total
Total Scan	pass-through	39	4	3	46
	not rec.	47	11	4	62
	stop 1 prong	15	1	3	19
	stop multipr.	5	1	3	9

Fig. 6.14: DB driven Total Scan result

Take into account the scanning efficiency and the plate to plate accuracy we require for the vertex reconstruction that the impact parameter (IP) must be within $50 \mu\text{m}$ and the longitudinal tracks distance among the end of two prong and the apex of the vertex within $4000 \mu\text{m}$.

For the tracks reconstructed in the volumes we have used the classification for *pass-through* tracks those volume tracks that have two or more base tracks after the stopping point; with *not reconstructed* (not rec.) those volume tracks with less or equal than 3 base-tracks reconstructed and volume not reconstructed; *stop 1 prong* are the base track with the stopping point reconstructed in the last plate in which has been seen by scan back procedures and *stop multiprong* are those stopping point which lead to vertex multiprong. The results of TS analysis compared with the SFT viewer classification is shown in table 6.14:

A large number of events were not reconstructed owing to the reduced efficiency (72%) of the emulsions used for the test. This efficiency is due most probably to the large amount of background tracks accumulated in the emulsions during the fly, and strong local distortions due to the process to assembly the brick (see previous chapter).

We try to perform another total scan on the whole brick with a software-based procedure on the general scan data. The software procedure reconstructs the volumes with the same parameters used in the DB driven procedures. The results is shown in the table 6.15:

	SFT viewer			Total
	Pass-through	Multitrack	candidates	
pass-through	40	5	8	53
not rec.	36	7	2	45
stop 1 prong	21	4	3	28
stop multitr.	9	1	0	10

Fig. 6.15: Results of the offline Total Scan performed on general scan.

The total scan procedure on the general scan data has reduced the not reconstructed events by factor 5%.

We perform, on BL088, a scan back procedures and a total scan using all the 607 SFT-doublet matches. The scan back results was that 187 were passing-through tracks and 420 were stopping tracks. Fig. 6.16 shows the distributions of the tracks followed versus the stopping plates, and the Fig. 6.17 shows the position and slope residuals between founded and predicted tracks.

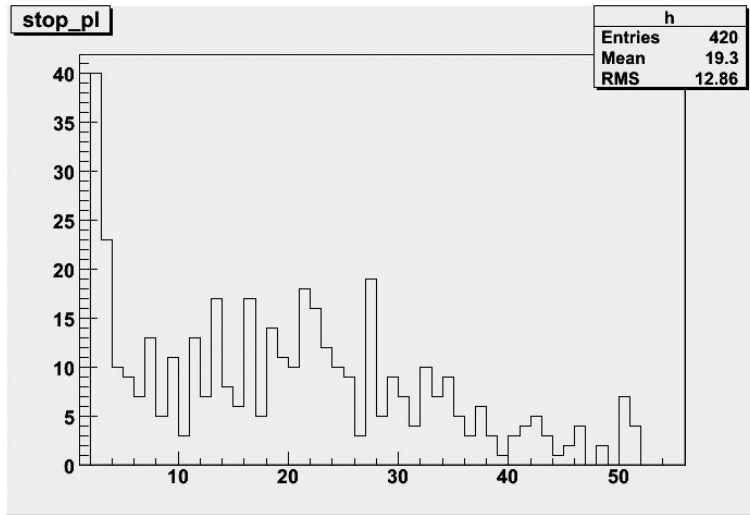


Fig. 6.16: Stopping plate distribution after the procedure of scan back.

On the 420 tracks we have applied the total scan procedure; in the analysis

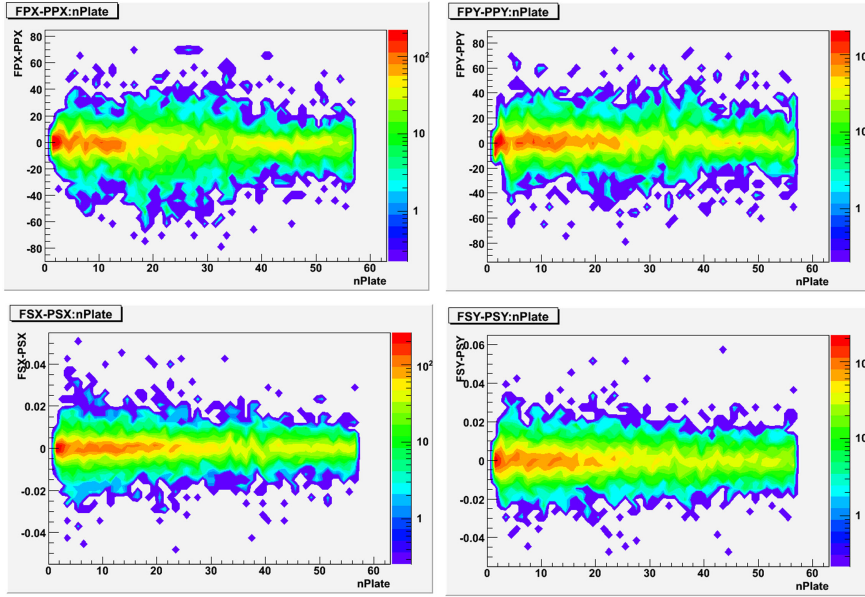


Fig. 6.17: Distributions of the residuals between found and predicted tracks as performed by Scan Back.

we have considered only those tracks that could be analyzed with a volume of 11 plates, excluding all the stopping point near the two ends of the bricks: i.e. we have considered only stopping point from plate 7 to plate 51. After this cut we have 329 tracks; all of them were reconstructed in the volume and analyzed.

The result was that 211 tracks were stopping tracks, 50 were passing-through, 57 not reconstructed and 11 were vertex (ten were two-prong and one was three). On this tracks we have considered all the tracks that survived at a cut ($\chi^2 < 5$) on the matches in order to consider in analysis only tracks with a good matches between fiber and emulsions. After this cut we have 19 pass-through tracks, 61 stopping, 25 not reconstructed and 7 vertex (one 3 prong and six double prong). Considering the stopping points as one prong vertexes, the final results is of 68 vertexes found on BL088.

The same procedures of off-line scan back has been applied to the 276 matches between fiber and doublet tracks on the brick BL034. We obtain 120 pass through

tracks and 156 stopping. The total scan is running.

6.6 Conclusions

We have performed a good alignment between the SFT predictions and the reconstructed tracks inside the bricks.

On the BL88, using the tools developed for the analysis of OPERA ECC, we have measured (68 ± 8) events induced by neutrinos. This number must be compared with the number of expected neutrino events, that for the fiducial volume analyzed on the BL088, is (97 ± 10) . If we include the efficiency of reconstruction in the data that is of 72%, the number of events is 94, in agreement with the expected.

Analysis of vertex searching performed by colleagues of Napoli group of European Scan Laboratory have found[79] (56 ± 6) events on a fiducial volume of 72 cm^2 , and on a brick exposed to 17.75 days to neutrino beam. We recall that on BL88 brick a fiducial volume of 80 cm^2 has been analyzed on 57 films and the exposition was of 28.18 days. Considering these differences the two results are in good agreement.

Conclusions

The OPERA experiment is close to perform its first physics run. If tau neutrinos will be observed in the CNGS beam, the hypothesis of neutrino oscillations will be completely and undoubtedly confirmed.

OPERA is already in the history of experimental technique for the large amount of emulsions that will be used, handled and analyzed. A dedicated battery of completely automated optical microscopes, characterized by high scanning speed, and high efficiency, will be able to perform a quasi on-line scanning of a large amount of nuclear emulsions. Many bricks per day will be shared among a network of scanning laboratories, both in Europe and in Japan. The Bologna scanning Lab. is included in the network and participated in the crucial steps of the R&D project.

In this thesis, developed in the Bologna emulsion scanning group, I have reported the results of the first exposure of an Emulsion Cloud Chamber (ECC), similar to the OPERA one, to a neutrino beam. Although the characteristics of the beam are different with respect to the CNGS one, this test was useful to validate the OPERA vertex reconstructing and searching tools.

Four bricks have been successfully aligned with the electronic detectors and analyzed with the Bologna fast microscopes. We had a good result in following tracks from the mm scale of the Scanning Fiber Tracker to the micrometric scale of the emulsion.

The procedures of Scan Back and Total Scan have been used and successfully tested on two bricks. The reconstruction performance of $\sim 70\%$ is far from the $\sim 90\%$ achieved on other tests using OPERA emulsions, the difference could be explained

CONCLUSIONS

considering the large background accumulated on the emulsions used in PEANUT test, during the airplane flight from Japan to Fermilab, which cannot be reduced by the virtual erasing technique.

The number of events found in one brick is (68 ± 8) , the expected number of events in the fiducial volume analyzed is 97. Taking into account the reconstruction efficiency (70%), the measured and expected events are in agreement.

Bibliography

- [1] W. Pauli, letter to a physicist's gathering at Tübingen, December 4, 1930.
Reprinted in *Wolfgang Pauli, Collected Scientific Papers*, ed. R. Kronig and V. Weisskopf, Vol. 2, p. 1313 (Interscience: New York, 1964).
- [2] F. Reines and C. Cowan, *Phys. Rev.* **92** (1953) 830(L).
- [3] M. Goldhaber, L. Grodzins and A.W. Sunyar, *Phys. Rev.* **109**, 1015(L).
- [4] G. Danby et al., *Zh. Eksp. Teor. Fiz.* **9** (1962) 36.
- [5] M. L. Perl et al., *Phys. Rev. Lett.* **35**, 1489 (1975); M. L. Perl et al., *Phys. Lett.* **63B**, 466 (1975); M. L. Perl et al., *Phys. Lett.* **70B**, 487 (1975).
- [6] K. Kodama et al., *Phys. Lett. B* **504** (2001) 218.
- [7] R. Davis, *J. Phys. Rev. Lett.* **12** (1964) 303.
- [8] B. Pontecorvo, *Zh. Eksp. Teor. Fiz.* **33** (1957) 549; *Zh. Eksp. Teor. Fiz.* **34** (1958) 247; *Zh. Eksp. Teor. Fiz.* **53** (1967) 1717.
- [9] Z. Maki, M. Nakagawa and S. Sakata, *Progr. Theor. Phys.* **28** (1962) 870.
- [10] J. N. Bahcall, *Astrophys. J.* **467** (1996) 475; J. N. Bahcall, S. Basu, M. H. Pinsonneault, *Phys. Lett. B* **433** (1998) 1.
- [11] B. T. Cleveland et al., *Astrophys. J.* **496** (1998) 505.
- [12] J. N. Abdurashitov, et al., *Phys. Rev. C* **60**, 055801 (1999); W. Hampel, et al., *Phys. Lett. B* **447**, 127 (1999).

BIBLIOGRAPHY

- [13] K. S. Hirata et al. (Kamiokande Coll.), *Phys. Lett. B* **280**, 146 (1988); *Phys. Lett. B* **280**, 146 (1992); Y. Fukuda et al. (Kamiokande Coll.), *Phys. Lett. B* **335**, 237 (1994).
- [14] Super Kamiokande Collaboration, *Nucl. Phys. B*, 145 (2005) 112-115.
- [15] Q. R. Ahmad et al. (SNO Coll.), *Phys. Rev. Lett.* **87** (2001) 071301.
- [16] Q. R. Ahmad et al. (SNO Coll.), *Phys. Rev. Lett.* **89** (2002) 011301; S. Ahmad et al., nucl-ex/0309004.
- [17] K. Eguchi et al. (KamLAND Coll.), *Phys. Rev. Lett.* **90** (2003) 021802.
- [18] M. Apollonio et al. (CHOOZ Coll.), *Eur. Phys. J. C* **27** (2003) 331.
- [19] F. Boehm et al. (Palo Verde Coll.), *Phys. Rev. D* **64** (2001) 112001.
- [20] IMB Coll., R. Becker-Szendy et al., *Phys. Rev. Lett.* **D46**, 372 (1992);
- [21] K.S. Hirata et al. (Kamiokande Coll), *Phys. Lett. B* **280**, 146 (1988); *Phys. Lett. B* **280**, 146 (1992); Y. Fukuda et al. (Kamiokande Coll) *Phys. Lett. B* **335**, 237 (1994).
- [22] NUSEX Coll. M. Aglietta et al., 23rd ICRC Proc., Vol.4 (1993) 446.
- [23] Frejus Coll., K. Daum et al., *Z. Phys.* **C66**, 417 (1995).
- [24] BAKSAN Coll., S. Mikheyev, 5th TAUP Workshop, Gran Sasso, Italy, 1997.
- [25] W.W.M. Allison et al., *Phys. Lett. B* **449**, 137 (1999); M. Sanchez et al., *Phys. Rev. D* **68** (2003) 113004.
- [26] M. Ambrosio et al. (MACRO Coll.), *Phys. Lett. B* **434**, 451 (1998).
- [27] SuperKamiokande Coll., Y. Fukuda et al., *Phys. Rev. Lett.* **81** 1562 (1998).
- [28] V. Agrawal et al., *Phys. Rev.* **D53**, 1314 (1996).
- [29] M. Honda et al., *Phys. Rev.* **D53**, 1314 (1996).

BIBLIOGRAPHY

- [30] M. Honda et al., Phys. Rev. **D64**, 053011 (2001); Phys. Rev. **D70**, 043008 (2004).
- [31] G. Battistoni et al., Astrop. Phys. **19**, 269 (2003).
- [32] M. Ambrosio et al., Phys. Lett. B **517** (2001) 59.
- [33] M. Ambrosio et al., Phys. Lett. B **566** (2003) 35.
- [34] G. Battistoni et al., Phys. Lett. B **615** (2005) 14-18.
- [35] G. L. Fogli et al., Phys. Lett. D **60** (1999) 053006.
- [36]
- [37] Y. Ashie et al., Phys. Rev. Lett. **93** (2004) 101801.
- [38] E. Aliu et al. (K2K Collaboration), Phys. Rev. Lett. **94** (2005) 081802.
- [39] M. H. Ahn, et al. (K2K Collaboration), Phys.Rev. D **74** (2006) 072003
- [40] D.G. Michael et al., Phys. Rev. Lett. **97**(2006) 191801.
- [41] Ch. Weinheimer et al., Phys. Lett. B **460**, 219 (1999); Phys. Lett. B **464**, 352 (1999);
- [42] W.W.M. Allison et al., Phys. Lett. B **449**, 137 (1999);
M. Sanchez et al., Phys. Rev. D **68** (2003) 113004. Nucl. Phys. B **118**, 279 (2003).
- [43] R. Barate et al., Eur. Phys. J. C **2**, 395 (1998).
- [44] S.Bilenky and S.Petcov, *Rev. Mod. Phys.* **59** (1987) 671 [Erratum ibid. **61** (1987), 169];
B.Kayser, *Neutrino Mass*, eds. G.Altarelli and K.Winter, Springer Tracts in Modern Physics (2003);
- [45] H.V.Klapdor-Kleingrothaus et al., *Mod. Phys. Lett.* **A16** (2001) 2490;

BIBLIOGRAPHY

- [46] H.V.Klapdor-Kleingrothaus *et al.*, *Phys. Lett.* **B586** (2004) 198;
- [47] C.E.Aalseth *et al.*, *Mod. Phys. Lett* **A17** (2002) 1475;
- [48] M. Guler *et al.* (OPERA Coll.) *Experimental proposal*, CERN-SPSC-2000-028;
- [49] CNGS project: On line at <http://proj-cngs.web.cern.ch/proj-cngs/> M. Guler *et al.* (OPERA Coll.) *Status report on the OPERA experiment*, CERN-SPSC-2001-025.
- [50]
- [51] Eidelman *et al.*, *Phys. Lett. B* **592** (2004).
- [52] B. Van de Vyver and P. Zucchelli, *Nucl. Instr. Meth.* A385 (1997) 91.
- [53] MACRO Coll., S. Ahlen *et al.*, *Phys. Lett. B* **357**, 481 (1995);
M. Ambrosio *et al.*, *Phys. Lett. B* **434** 451 1998;
M. Ambrosio *et al.*, *Eur. Phys. J. C* **36** 323 2004. (1997) 1297.
- [54] B. Van de Vyver, *Nucl. Instr. and Meth. A* **385** (1997) 91.
- [55] M.C. Gonzalez-Garcia and J.J. Gomez-Cadenas, *Phys. Rev. D* **55** (1997) 1297.
- [56] Walter H. Barkas *Nuclear research emulsion* 1963 Academic Press, New York and London.
- [57] http://www.ilford.com/html/us_english/prod_html/nuclear/ParticlePhysics.html
- [58] C. Lattes, H. Muirhead, G. Occhialini, C. Powell, Process involving charged mesons, *Nature* **159** (1947) 694.
- [59] D. Allasia *et al.*, *Nucl. Phys. B* **176** (1980) 13.
- [60] N. Ushida *et al.*, *Nucl. Instr. Meth.* **224** (1984) 50.
- [61] S. Aoki *et al.*, *Nucl. Instr. Meth. A* **274** (1989) 64.

BIBLIOGRAPHY

- [62] K. Kodama et al., Phys. Lett. B **504** (2001) 218.
- [63] T. Nakamura PhD Thesis (2004) Nagoya University
- [64] C. Sirignano PhD Thesis Salerno University (2004)
- [65] G. Rosa et al. "Automatic Development of OPERA emulsion film", 2004.
- [66] S. Aoki et al., Nucl. Instr. Meth. B **51** (1990) 466.
- [67] S. Aoki, Nucl. Instr. Meth. A **473** (2001) 192.
- [68] G. Rosa et al., Nucl. Instr. Meth. A **394** (1997) 357.
- [69] N. Armenise et al., Nucl. Instrum. Meth. A **551** (2005) 261.
- [70] W.J. Smith, Modern optical engineering, the design of optical systems, Third Edition, McGraw-Hill (2000).
- [71] V. Tioukov et al., Nucl. Instrum. Meth. A **559** (2006) 103.
- [72] E. Barbuto et al., Nucl. Instrum. Meth. A **525** (2004) 485.
- [73] H. W. Atherton et al. CERN-80-07.
- [74] D. S. Barton et al. Phys. Rev. D **27**, 2580 (1983).
- [75] G. Ambrosini et al. Eur. Phys. J. C **10** 605 (1999).
- [76] A. Abramov et al. MINOS Internal note 675 (2000).
- [77] M. Kostin et al. MINOS Internal note 783 (October 2001).
- [78] C. Sirignano "R&D on OPERA ECC: studies on emulsion handling and event reconstruction techniques", PhD Thesis, Salerno University, AA 2004-2005, pp 130.
- [79] Degree Thesis,
- [80] <http://flab.phys-nagoya-u.ac.jp/inetpub/peanut/DST/TOOL/src/sftview/v02.03>
- [81] Chiara Sirignano, R&D on OPERA ECC, PhD Thesis 2004/2005.

BIBLIOGRAPHY
